

Copyright
by
Ina Pavlova
2007

**The Dissertation Committee for Ina Pavlova Certifies that this is the approved
version of the following dissertation:**

**The Biological Basis for Changes in Autofluorescence during Neoplastic
Progression in Oral Mucosa**

Committee:

Rebecca Richards-Kortum, Supervisor

Ann Gillenwater

Calum MacAulay

Michele Follen

Thomas Milner

**The Biological Basis for Changes in Autofluorescence during Neoplastic
Progression in Oral Mucosa**

by

Ina Pavlova, B.S.; M.S.

Dissertation

Presented to the Faculty of the Graduate School of

The University of Texas at Austin

in Partial Fulfillment

of the Requirements

for the Degree of

Doctor of Philosophy

The University of Texas at Austin

December, 2007

Dedication

To my mother, Stefka Georgieva and my father, Pavel Pavlov.

Acknowledgements

First, I would like to thank my advisor Dr. Rebecca Richards-Kortum for her guidance through my research. Having Rebecca as an advisor was an exceptional experience and without her critical insight, encouraging support and optimism this dissertation could have not been written. She is also a great role model, proving that balancing career and family is possible. I am also thankful to Dr. Ann Gillenwater for all the support and help in the clinical part of my research. I'd also like to acknowledge Dr. Adel El-Naggar and Dr. Michelle Williams for providing the pathology readings of my slides and taking time from their busy schedule to help in interpreting the high resolution images of oral tissue. In addition, I would like to thank Dr. Michele Follen, Dr. Calum MacAulay and Dr. Thomas Milner. It is a privilege to have them on my Ph.D. committee. Finally, I'd like to thank all the members of the optical spectroscopy lab for all the crucial support when research got tough and for providing an enjoyable working environment.

Austin, TX

November 16, 2006

The Biological Basis for Changes in Autofluorescence during Neoplastic Progression in Oral Mucosa

Publication No. _____

Ina Pavlova, Ph.D.

The University of Texas at Austin, 2007

Supervisor: Rebecca Richards-Kortum

Autofluorescence spectroscopy can improve the early detections of oral cancer. Biochemical and structural changes associated with dysplastic progression alter the optical properties of oral mucosa and cause diagnostically significant differences in spectra from normal and neoplastic sites. This dissertation describes experimental and modeling studies aimed at revealing biological reasons for the diagnostically significant differences observed in depth-resolved fluorescence spectra from normal and neoplastic oral mucosa.

An experimental approach, based on high-resolution fluorescence imaging, is used to study the autofluorescence patterns of oral tissue. At UV excitation, most of the epithelial autofluorescence originates from cells occupying the basal and intermediate layers, while stromal signal originates from collagen and elastin crosslinks. With dysplasia, epithelial autofluorescence increases, while autofluorescence from subepithelial stroma drops significantly. Benign lesions also display a drop in

autofluorescence from subepithelial stroma, but have different epithelium fluorescence patterns compared to dysplasia. Optical probes that measure mostly stromal fluorescence, may reveal a similar loss of fluorescence intensity and thus fail to distinguish benign inflammation from dysplasia. These results emphasize the importance of using probes with enhanced detection of epithelial fluorescence for improved diagnosis of different types of oral lesions.

The second part of this work presents a Monte Carlo model that predicts fluorescence spectra of oral mucosa obtained using a depth-selective probe as a function of tissue optical properties. A model sensitivity analysis determines how variations in optical parameters associated with neoplastic development influence the intensity and shape of spectra, and elucidates the biological basis for differences in spectra from normal and premalignant oral mucosa. Spectra of oral mucosa collected with the depth-selective probe, are affected by variations in epithelial optical properties and to a lesser extent by changes in superficial stromal parameters, but not by changes in the optical properties of deeper stroma. Changes in parameters associated with dysplastic progression lead to a decreased fluorescence intensity and a shift of the spectra to longer emission wavelengths. Decreased fluorescence is due to a drop in detected stromal photons, whereas the shift of spectral shape is attributed to an increased fraction of detected photons arising in the epithelium.

Table of Contents

List of Tables.....	xi
List of Figures.....	xii
Chapter 1: Introduction.....	1
1.1 Overview.....	1
1.2 Specific aims.....	6
Chapter 2: Background.....	7
2.1 Motivation.....	7
2.2 Anatomy of the oral cavity.....	8
2.3 Pathology of the oral cavity.....	10
2.4 Optical technologies of a diagnostic tool.....	12
2.5 Optical Properties of normal and abnormal epithelial tissue.....	14
2.5.1 Fluorophores.....	15
2.5.2 Scatterers.....	17
2.5.3 Absorbers.....	17
2.6 Modeling of fluorescence in turbid media	18
2.7 Monte Carlo modeling.....	21
Chapter 3: Understanding the biological basis of autofluorescence imaging for oral cancer detection: High resolution fluorescence microscopy in viable tissue....	24
3.1 Introduction.....	24
3.2 Methods.....	27
3.2.1 Biopsy collection and preparation of tissue slices	27
3.2.2 Confocal microscopy and image collection.....	27
3.2.3 Histology.....	28
3.2.4 Image analysis.....	29
3.3 Results.....	31
3.3.1 Normal oral mucosa autofluorescence patterns	32

3.3.2 Autofluorescence patterns in inflammatory and dysplastic oral tongue tissue.....	35
3.3.3 Quantitative analysis of fluorescence in normal, benign, and dysplastic oral tongue slices	36
3.3.4 Autofluorescence of well, moderately and poorly differentiated carcinomas	40
3.4 Discussion.....	44
Chapter 4: A Monte Carlo model to describe depth selective fluorescence spectra of epithelial tissue: Applications for diagnosis of oral precancer.....	
4.1 Introduction.....	49
4.2 Methods.....	52
4.2.1 Clinical measurements of fluorescence spectra from oral mucos.....	52
4.2.2 Tissue geometry and model input parameters	52
4.2.3 Description and validation of the Monte Carlo model.....	56
4.2.4 Predictions of Tissue Fluorescence	59
4.3 Results.....	60
4.3.1 Validation of model with probe to target measurements	60
4.3.2 Sensitivity of the model to variations in epithelial input parameters	61
4.3.3 Sensitivity of the model to variations in stromal input parameters.....	66
4.3.4 Depth sensitivity analysis for fluorescence light.....	71
4.3.5 Comparison of Monte Carlo predictions to average clinical spectra	74
4.4 Discussion.....	77
Chapter 5: The biological basis for differences in fluorescence spectra caused by neoplastic development and by anatomical site variations in oral mucosa.....	
5.1 Introduction.....	81
5.2 Methods.....	83
5.2.1 Clinical measurements and biopsy collection.....	83
5.2.2 Tissue geometry and model input parameters.....	83

5.3 Results.....	86
5.3.1 Biological basis for spectral differences caused by neoplastic progression	86
5.3.2 Biological basis for spectral differences caused by anatomical site variations	89
5.4 Discussion.....	94
Chapter 6: Conclusion.....	96
6.1 Summary and contributions	96
6.2 Future research directions.....	100
References	103
Vita	112

List of Tables

Table 3.1:	Total number of biopsies for each diagnostic category and anatomic site	31
Table 4.1:	Effect of input parameters associated with hyperkeratosis, hyperplasia and dysplasia on the fraction of photons detected from the epithelium and the fraction of photons detected from the superficial oral mucosa (the epithelium and stromal layer 1) at emission wavelength of 440 nm.	65

List of Figures

Figure 2.1:	Anatomy and architecture of the oral cavity. (A) Major anatomical sites of the oral cavity (adapted from ref. 8); (B) Basic architecture of stratified squamous epithelium (adapted from ref. 9).....	9
Figure 2.2:	An illustration of the stepwise progression of normal squamous epithelium to invasive cancer	11
Figure 2.3:	Deflection of a photon at a scattering event. The scattering angle or deflection angle is indicated by θ (Adapted from http://omlc.ogi.edu/)	22
Figure 3.1:	Fluorescence and histologic images of normal tongue without inflammation: Confocal fluorescence images at (A) UV excitation, (B) 488 excitation and (C) H&E image. Scale bars represent 200 μm in the confocal images and 125 μm in the H&E image. Note that epithelial fluorescence increase with depth at UV excitation and slightly decrease at 488 nm excitation.....	33
Figure 3.2:	Fluorescence and histologic images of four normal oral sites without inflammation. Confocal fluorescence images at both UV (top row) and 488 nm excitation (middle row) and H&E image (bottom row) from (A) palate; (B) gingiva; (C) floor of mouth and (D) buccal mucosa. White line indicates the approximate location of the basement membrane. Scale bars represent 200 μm . Note that the superficial layer is significantly more fluorescent is the palate, then in other anatomical sites. Gingival epithelium displays a loss of fluorescence at UV excitation, which is unusual for other normal sites.....	34

Figure 3.3: Fluorescence patterns of (A) inflammation and (B) mild dysplasia in the oral tongue. Mosaic of confocal fluorescence images at UV (left), 488 nm excitation (middle) and H&E images (right). The histopathologic diagnosis of (A) is normal, non-dysplastic epithelium with severe inflammation and of (B) is mildly dysplastic epithelium with mild to moderate inflammation. White line indicates the approximate location of the basement membrane. Scale bars in the confocal images represent 200 μm and scale bars in the H&E images represent 120 μm . Arrow heads mark lymphocytic infiltration.....38

Figure 3.4: Quantitative analysis of the average fluorescence intensities of all normal, inflammatory and dysplastic oral tongue tissues. (A) Overlaid UV and 488 nm excited fluorescence images and (B) a simplified cartoon of normal tongue showing the approximate distribution of the epithelial and stromal subregions. Type 2 cells display easily visualized cytoplasmic fluorescence at UV excitation; while type 1 cells exhibit a weak cytoplasmic signal at UV excitation. Stromal region 1 includes stroma that is 100 -200 microns below the basement membrane, whereas stromal region 2 represents deeper stroma. Average fluorescence intensities at (C) UV excitation and (D) 488 nm excitation for each epithelial and stromal region. Error bars represent one standard deviation. Legend key for the diagnostic categories: N-Normal without inflammation (n=8); NMI-Normal with mild to moderate inflammation (n=2); NSI- Normal with severe inflammation (n=3); DMI-Dysplasia with mild to moderated inflammation (n=6).39

Figure 3.5: Fluorescence patterns of invasive tumors in the oral cavity. Confocal fluorescence images at UV (first column) and 488 nm excitation (second column); overlaid UV and 488 nm images (third column) and H&E images (fourth column). (A) Mildly dysplastic epithelium overlaying well differentiated submucosal carcinoma in the tongue; (B) Moderately differentiated carcinoma in the tongue; (C) Poorly differentiated carcinoma in the palate (C). Scale bars represent 200 microns.....41

Figure 3.6: Quantitative analysis of invasive tumors. (A) Overlaid UV and 488 nm excited fluorescence images and (B) a simplified cartoon of an invasive tumor showing the distribution of type 1 (green regions) and type 2 (dark blue regions) cancer cells surrounded by fibrous stroma (light blue region). Type 2 cancer cells display easily visualized cytoplasmic fluorescence at UV excitation; while type 1 cancer cells exhibit weak cytoplasmic signal at UV excitation. Fibrous stroma includes matrix with a dominant fiber component. Average fluorescence intensities at (C) UV and (D) 488 nm excitation for each subregion and (E) average redox ratio values for type 1 and type 2 cancer cells. Error bars indicate one standard deviation. Legend key for diagnostic categories: WDC-Well differentiated carcinoma (n=6); MDC-Moderately differentiated carcinoma (n=6) ; PDC-Poorly differentiated carcinoma (n=1).....43

Figure 4.1: Baseline tissue geometry and input parameters: (A) Tissue geometry for normal oral tissue, (B) Normalized fluorescence efficiencies, (C) Absorption coefficients, (D) Scattering properties.....55

Figure 4.2: Diagram of the depth-selective fiber optic probe geometry used in the Monte Carlo forward model. S represents the source fiber, and D the detector fiber. An air gap separates the fibers and the half ball lens. The distance between the source and detector fibers is 0.072 cm. The window is placed in contact with tissue.	58
Figure 4.3: Detected fluorescence intensity from a thin fluorescent layer as the separation between the target and window is varied. The line represents Monte Carlo predictions and the symbols are experimental measurements.....	60
Figure 4.4: Effect of epithelial input parameters, associated with (A, B) hyperkeratosis, (C, D) hyperplasia and (E, F) dysplasia on the intensity (left column) and spectral shape (right column) of the predicted fluorescence spectra.....	64
Figure 4.5: Effect of variations in the magnitude of the fluorescence efficiency of the stroma on (A and C) the intensity and (B and D) spectral shape of the predicted fluorescence spectra: (A-B): changes in superficial stromal layer 1 and (C-D): and deeper stromal layer 2.....	68
Figure 4.6: Effect of variations in the volume fraction of hemoglobin on (A and C) the intensity and (B and D) spectral shape of the predicted fluorescence spectra: (A-B) Changes in superficial stromal layer 1 and (C-D) deeper stromal layer 2.....	69
Figure 4.7: Effect of variations in the stromal scattering on (A and C) the intensity and (B and D) spectral shape of the predicted fluorescence spectra: (A-B) Changes in superficial stromal layer 1 and (C-D) deeper stromal layer 2.....	70

Figure 4.8:	Depth profiles at emission wavelength of 440 nm for (A) the baseline case and (B) hyperplasia with increased non-keratinized epithelium of 150 μm . The profiles show the distribution of fluorescence photons in basal epithelium, superficial stroma and deeper stroma. The green line indicates the mean depth of fluorescence, whereas the red line marks the depth above which 85 % of fluorescence photons originate.....	73
Figure 4.9:	Comparison of average clinical fluorescence spectra from normal oral mucosa (blue line) and lesions diagnosed with moderate to severe dysplasia (red line) to Monte Carlo predictions. (A) Average clinical spectra and predictions. Error bars represent the standard deviation in the clinical data for each diagnostic category. Number of detected photons from the epithelium and stroma in (B) normal and (C) dysplastic predictions.....	76
Figure 5.1:	Fluorescence confocal images and clinical depth-resolved fluorescence spectra at UV excitation showing 3 stages of neoplastic progression in the tongue. The spectra are measured from the same oral sites shown in the confocal images. (A) Normal Tongue, (B) Focal Mild Dysplasia (with stromal inflammation), (C) moderately differentiated cancer, (D) Fluorescence spectra at 350 nm excitation of normal tongue (blue line), focal mild dysplasia (green line), and moderately differentiated cancer (red line).....	87

Figure 5.2: Validation of the Monte Carlo model with clinical fluorescence spectra of (A) a normal tongue site, (B) focal mild dysplasia, and (C) moderately differentiated cancer measured from the same patient. The x axis represents emission wavelength in nm, while the y axis represents normalized fluorescence intensity. The bar graphs represent the predicted number of photons originating from the epithelium (black bars) and the stroma (white bars) for (D) normal and (E) dysplastic oral tissue. The depth statistics for the cancerous example are displayed in (F) where the black bars represent detected photons from a superficial region (top 400 microns) with cancer cells and the white bars represent photons detected from the underlying fibrous matrix.....90

Figure 5.3: Fluorescence confocal images and depth-resolved clinical fluorescence spectra at UV excitation showing changes in autofluorescence patterns due to anatomical site variation. The spectra were measured from the same oral sites shown in the confocal images. Confocal images from (A) normal buccal and (B) normal palate. (C) Emission spectra at 350 nm excitation of normal buccal (red line) and normal palate (green line).....92

Figure 5.4: Validation of the Monte Carlo model with clinical spectra of oral sites from (A) normal buccal and (B) normal palate. The x axis represents emission wavelength in nm, while the y axis represents normalized fluorescence intensity. The bar graphs represent the predicted number of photons originating from the superficial (first bars); intermediate (second bars) and basal (third bars) epithelium and the stroma (forth bars) for (C) normal buccal and (D) normal palate.....93

Chapter 1: Introduction

1.1 OVERVIEW

Cancer is one of the leading problems in public health and second only to heart disease as the leading cause of death in the United States. The overall five-year survival rate for cancer in many organs has remained low for the past several decades despite advances in the treatment of this disease. The mortality due to cancer can be greatly reduced by accurate early diagnosis before malignant changes have spread to distant sites in the body. For example, the five-year survival rate for oral cancer patients with advanced stages of disease is 21%; this figure improves to 80% if cancer is diagnosed at local stages of development. Providing an accurate early diagnosis of oral lesions is an important step towards decreasing the mortality caused by oral cancer.

Current screening techniques for oral lesions have a number of limitations. The accurate clinical detection of an oral lesion depends heavily on the expertise of the clinician and may involve several invasive biopsies. These limitations motivate the need for an automated, non-invasive and accurate diagnostic tool to aid the clinician in discriminating malignant oral lesions from normal oral tissue. A combination of autofluorescence spectroscopy and imaging has the potential to offer accurate, non-invasive, real-time diagnoses of oral lesion in a clinical settings. Preliminary clinical studies have shown that both autofluorescence spectroscopy and imaging can accurately distinguish oral lesions from healthy mucosa. Autofluorescence images and spectra display a set of diagnostically significant features that can be used to discriminate normal from abnormal tissue. However, the biological basis for these diagnostically significant

differences in autofluorescence spectra and images from normal and neoplastic tissue is not well understood.

Neoplastic transformation in oral mucosa is accompanied by a series of morphological, structural and biochemical changes that affect the optical properties of both epithelial and stromal tissue. These altered optical parameters are reflected as diagnostically significant differences in the autofluorescence spectra of normal, precancerous and cancerous epithelial sites. Improving the accuracy of fluorescence spectroscopy as a diagnostic tool for oral cancer detection within a large and diverse population requires a thorough understanding of the relationship between the changes in tissue optical properties and the measured fluorescence spectra. Analysis of spectral variations caused by neoplastic progression can be achieved by developing mathematical models to describe fluorescence propagation in oral tissue. The design of an accurate model for fluorescence light propagation in oral mucosa depends on prior knowledge of the key optical parameters associated with cancer progression and their effect on the intensity and shape of the in vivo spectra.

For multilayered tissue, such as the oral mucosa, understanding the biological factors behind differences in spectra is more complex because the measured data contain contributions from both the epithelium and stroma. Since most oral cancers originate in the epithelium, the diagnostic accuracy of autofluorescence spectroscopy can be improved by designing fiber optic probes that provide enhanced detection of fluorescence originating from within this region. In our research group, a ball-lens coupled probe was previously designed and proven to offer depth-resolved detection of fluorescence. This probe is currently used to obtain depth-resolved fluorescence spectra from normal and neoplastic oral sites in a clinical setting.

This dissertation aims at understanding the biological basis for diagnostically significant differences in depth-resolved spectra from normal and malignant oral sites measured with the clinical ball-lens coupled probe. A Monte Carlo based modeling approach was used to study how changes in optical parameters associated with neoplastic progression in the oral cavity affect fluorescence intensity and spectral shape. Previously, Monte Carlo simulations have been implemented for model-based analysis of fluorescence and reflectance spectra from cervical tissue. These existing models do not account for the multilayered structure of the oral mucosa. A unique feature of the approach that I took, is the use of biologically realistic fluorescence and tissue geometry, specific for oral cavity tissue as input parameters for Monte Carlo simulations. Other innovative characteristics of the Monte Carlo code presented in this work, is the modeling of fluorescence detection with a ball lens coupled fiber optic probe, and the ability to predict depth-resolved fluorescence spectra measured by the clinical probe.

Chapter 2 gives background information relevant to the research presented in this dissertation. The anatomy and pathology of oral mucosa are reviewed, followed by a summary of the application of fluorescence spectroscopy to oral cancer diagnosis and an overview of commonly used modeling methods to analyze fluorescence spectra from normal and abnormal epithelial tissue. A theoretical background of the Monte Carlo modeling approach has also been provided in this chapter.

In order to obtain biologically realistic input for the Monte Carlo model, the autofluorescence patterns of normal and neoplastic oral tissue has been experimentally determined in a high resolution microscopy study of fresh oral biopsies. Chapter 3 describes, qualitatively and quantitatively, the distribution of autofluorescence at the cellular level in oral tissue using laser scanning confocal fluorescence microscopy. The primary objective of this study was to characterize the origins of autofluorescence in

normal oral mucosa and to assess the effect of anatomical site variations on these autofluorescence patterns. In this chapter, I also studied how inflammation and dysplasia alter the autofluorescence properties of oral tissue and compared the autofluorescence patterns of oral cancers with different grades of differentiation. Upon visual examination of the confocal images, oral mucosa was subdivided into several sublayers with distinct autofluorescence characteristics. The average fluorescence intensity of each sublayer was determined for normal, inflammatory and dysplastic tissue slices. The resulting values were used to quantitatively analyze how neoplastic progression affects the depth-dependent distribution of autofluorescence in oral tissue. In addition, these average fluorescence values were used as biologically realistic input to the Monte Carlo based model. Thus, understanding how autofluorescence patterns in the epithelial and stromal layers change during oral carcinogenesis was the first step in the development of accurate and biologically realistic model for predicting depth-resolved fluorescence from oral mucosa.

A detailed description of the Monte Carlo based model for light propagation in oral tissue is offered in Chapter 4. The oral mucosa was represented as a multi-layered tissue geometry, allowing for depth-dependent variation in optical parameters in both the epithelium and the stroma. This model uses realistic fluorescence input parameters for each sublayer derived from measurements obtained from normal and neoplastic oral tissue to predict depth-resolved fluorescence detected by the clinical probe. A Monte Carlo based analysis was performed to study the sensitivity of predicted spectra to changes in biologically relevant optical parameters associated with the development of precancer and cancer. This served to identify the key optical parameters responsible for the observed differences in normal and neoplastic fluorescence spectra. Next, the model was validated by predicting normal and dysplastic depth-resolved fluorescence spectra

and comparing the predictions to data measured in the clinic. Finally, model predictions of average normal and dysplastic fluorescence spectra were analyzed to elucidate the biological reasons for diagnostically significant spectral features observed in clinical data. Chapter 5 further validates the ability of the Monte Carlo model to predict depth-resolved spectra from oral mucosa by comparing predictions to in vivo measurements from a normal, dysplastic and a cancerous site obtained from the same patient. To increase the accuracy of the predictions, input parameters for the thickness and fluorescence intensity of epithelial and stromal sublayers were derived from confocal images of biopsies obtained from the same oral sites that were clinically measured.

Normal oral tissue differs in the degree of keratinization of the superficial epithelial layer, which could contribute to a significant spectral variance in clinical data. Chapter 5 investigates how a thick and strongly fluorescent superficial layer affects Monte Carlo predictions and suggests possible biological reasons for variations in clinical depth-resolved spectra measured from keratinized and nonkeratinized anatomical sites. In particular, fluorescence spectra from normal tongue, buccal and palate were simulated and compared to clinical data. Depth analysis of the prediction is used to explain differences observed in the clinical measurements from these various normal oral sites.

Chapter 6 summarized the main accomplishments of this work and discusses the future directions for the research presented in this dissertation. Monte Carlo simulations present a convenient approach to analyze fluorescence spectra from the oral cavity and to understand the key optical parameters responsible for the differences between clinical normal and abnormal data. However, a Monte Carlo modeling approach for spectral analysis is computationally intensive and time consuming. Thus, the next step in model based analysis of fluorescence spectra is to develop an analytical expression that can accurately describe depth-resolved fluorescence spectra from multilayered tissue.

1.2 SPECIFIC AIMS

In summary, the primary objective of my research is to elucidate the biological basis for diagnostically relevant differences in depth- resolved fluorescence spectra measured from normal and abnormal oral mucosa.

My specific goals were to:

1. Use high-resolution fluorescence microscopy imaging of fresh biopsies to elucidate the autofluorescence patterns of normal oral tissue and to investigate how these patterns vary in benign, dysplastic and cancerous lesions.
2. Divide normal, benign and dysplastic oral mucosa into several layers with distinct autofluorescence characteristic and estimate, quantitatively, the average fluorescence intensity of each sublayer. Use these experimentally derived parameters as biologically realistic input to the Monte Carlo model.
3. Develop a Monte Carlo based model that can predict depth-resolved fluorescence spectra from normal and neoplastic oral sites. Unique features of this code include the use of multilayered tissue geometry and fluorescence input parameters specific for oral tissue. In addition, this code predicts spectra measured with a ball-lens coupled probe that offers enhances detection of epithelial fluorescence.
4. Implement the depth-sensitive Monte Carlo model to determine some of the optical parameters responsible for diagnostically significant differences observed in clinically measured fluorescence spectra from normal and neoplastic oral tissue. Based on these results, predict fluorescence spectra from normal, dysplastic and cancerous sites and validate simulations with clinical data. Use predictions to elucidate the biological basis for the decrease in intensity and shift of spectra shape to longer emission spectra that are commonly observed when comparing normal and neoplastic clinical spectra.

Chapter 2: Background

2.1 MOTIVATION

Oral cancer is a major health problem worldwide. It has been estimated that annually oral cancer is responsible for more than 7500 deaths in the United States and approximately 127,000 deaths worldwide (1, 2). Oral cancer is an epithelial cancer, which arises from genetic damage due to exposure to carcinogens (3), and it is closely associated with the tobacco usage and alcohol consumption (4). Additional causes of oral cancer include nutritional deficiencies, poor dentition, genetic predispositions, and viruses such as the human papilla and the herpes simplex viruses (HPV, HPS) (5, 6).

Despite years of research in cancer treatment, U.S. oral cancer survival rates have remained the same for approximately the last 20 years (2). The five-year survival rate for patients with advanced stages of the disease is 21%; however it improves to 81% if cancer is diagnosed early (2). Early diagnosis of oral cavity lesions drastically reduces the mortality rate associated with this disease, however with current oral cavity screening methods, it is difficult to identify early malignancies of the oral cavity. Screening for oral cancer is typically performed during dental check up or routine physical examination (7). Current techniques for detection oral lesions include clinical observation of the suspected area, followed by the performance of invasive biopsies by the clinician. Microscopic histologic examination of the biopsied tissue by a trained pathologist remains the gold standard for oral cancer diagnosis.

The accuracy of current screening methods for oral cancer detection depends substantially on the clinical expertise of the practitioner and the performing of repeated invasive biopsies of suspected areas. However, even experienced practitioners have

difficulty distinguishing premalignant lesions from benign inflammatory conditions. In addition, in high risk patients the entire mucosal lining is at risk for developing multiple lesions. Accurate diagnosis would depend on the performance of multiple oral biopsies, which are painful and require a waiting period for diagnostic results. Thus, both the patients and clinicians are hesitant to have multiply biopsies performed. Improvements in current screening methods would require a non-invasive diagnostic tool that can help the general practitioner accurately diagnose early stages of oral cavity malignancies in a one-time visit to the clinic.

2.2 ANATOMY OF THE ORAL CAVITY

As shown in Figure 1 A, the oral cavity is a multi-site organ with several anatomical sites. In general, the oral cavity is covered by a squamous epithelial tissue called the oral mucosa. Figure 1 B shows that oral mucosa can be divided into two major layers: the squamous epithelium and the underlying connective tissue (Figure 1 B). The squamous epithelium consists of several layers of cells stacked above the basement membrane. Germinative cells (or basal cells) occupy a region immediately above the basement membrane and are responsible for new cell growth. Thus, these cells have high cell proliferation and metabolism rates. As basal cells proliferate, they move upwards towards the tissue surface, where they become keratinized and are sloughed off every 6-7 days. The connective tissue directly below the basement membrane is called the lamina propria (or stroma) and it is composed primarily of fibrous proteins such as collagen and elastin. This region is also perfused with a network of capillaries. The oral mucosa can be subdivided into two main types, depending on the principal patterns of epithelial differentiation: keratinized and nonkeratinized oral mucosa. The buccal, floor of mouth,

soft palate and ventral surface of the tongue are covered by nonkeratinized oral mucosa. Differentiation in keratinized oral mucosa leads to the production of a distinct keratin layer, called the stratum corneum. Keratinized oral mucosa covers the oral anatomical sites such as the hard plate, gingiva and the dorsal side of the tongue (10).

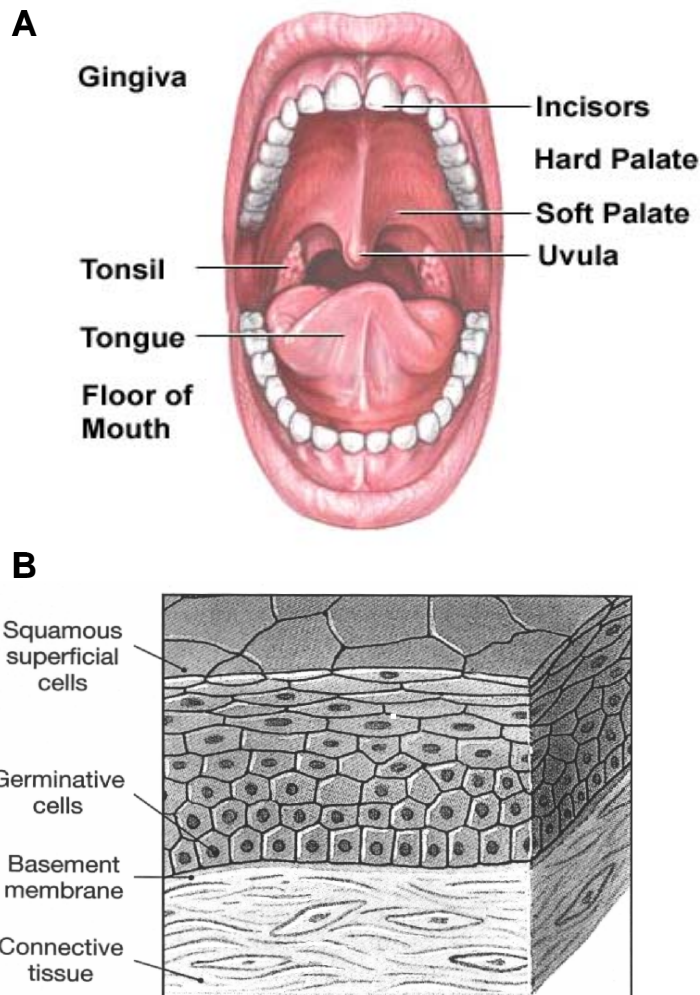


Figure 2.1: Anatomy and architecture of the oral cavity. (A) Major anatomical sites of the oral cavity (adapted from (8)); (B) Basic architecture of stratified squamous epithelium (adapted from (9)).

2.3 PATHOLOGY OF THE ORAL CAVITY

More the 90 % of all cancers in the oral cavity are squamous cell carcinomas which arise from the epithelial region of the oral mucosa (6). Figure 2 illustrates the step-wise progression of normal oral tissue to mild, moderate and severe dysplasia, carcinoma in situ, and finally, invasive carcinoma. Dysplastic progression is characterized by a series of morphologic cellular features including increased nuclear size, increased nuclear to cytoplasmic ratio, increased rate of mitosis, and hyperchromasia (11). Oral dysplasia is also associated with architectural changes such as disordered maturation from basal to squamous cells, hyperplasia of the basal cell layer and excessive surface keratin (hyperkeratosis) (11). An increased rate of proliferation within the basal layer is the first step of dysplastic transformation. Sites where cell proliferation is limited to one third of the epithelial thickness are diagnosed with mild dysplasia, whereas cell proliferation occupying more the half of epithelium is defined as higher grades of dysplasia. Carcinoma in situ is defined as having uncontrolled growth of epithelial cell, occupying the whole thickness of the epithelium. Invasion of malignant epithelial cells through the basement membrane is diagnosed as invasive carcinoma.

Oral lesions can be divided into two groups depending on their clinical appearance. Most lesions have the appearance of white patches and are called “leukoplakia”. Silverman has observed in a study of 257 cases over a time period of 7.2 years that 17.5% of leukoplakias undergo premalignant transformation (12). Most of the precancerous lesions (85%) have the appearance of leukoplakia (13); however some benign conditions such as hyperkeratosis or severe chronic inflammations, such as lichen planus, can have the appearance of white patches (14). This complicates the clinical recognition of benign and premalignant oral lesion. Lesions with the appearance of a red

patch are defined as “erythroplakia” and are associated, most of the time, with malignant or premalignant transformations at the time of clinical diagnosis (3). Lesions having a mixed appearance of red and white patches (erythroleukoplakia) are more likely to develop malignant transformations compared to white lesions alone (6). The diverse appearance of oral lesions complicates accurate clinical diagnosis and requires the performance of repeated biopsies, even in cases of benign transformations. This motivates the need for a non-invasive, accurate technique to aid the clinician in diagnosing oral neoplasia.

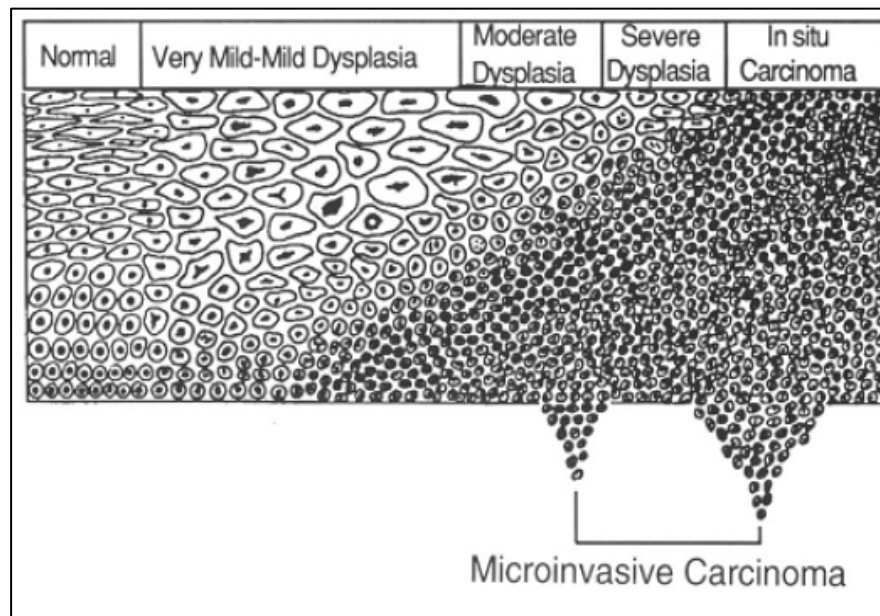


Figure 2.2: An illustration of the stepwise progression of normal squamous epithelium to invasive cancer.

2.4 OPTICAL TECHNOLOGIES AS A DIAGNOSTIC TOOL

Optical spectroscopy has emerged as a fast, accurate and non-invasive technology for diagnosing precancers and cancers in several organ sites. Several research groups have demonstrated that in vivo fluorescence spectroscopy can diagnose precancerous lesions in the cervix with a high sensitivity and specificity ranging from 68% to 90% (15-18). For example, a diagnostic algorithm, having a sample size of 147 patients and excitation wavelengths of 350 and 430 nm, distinguished high grade cervical lesions from normal tissue with 68% specificity and 81% sensitivity (15). Optical spectroscopy has shown much promise as a diagnostic tool in other organ sites such as breast tissue (19), esophagus (20), the bladder (21), and the colon (22).

In the oral cavity, several pilot studies proved that fluorescence spectroscopy can distinguish oral lesions from normal mucosa with sensitivity and specificity in the range of 82-100% (23-28). The accuracy of diagnosis oral cancer from normal tissue is especially high with sensitivity and specificity values above 95%. Heintzelman et al. reported that in a clinical study of 56 patients, fluorescence spectroscopy achieved 100% sensitivity and 90% specificity in diagnosing oral lesions from healthy tissue (24). Muller et al. recorded autofluorescence and reflectance spectra from 91 oral sites and developed a model to disentangle the effect of scattering and absorption on the intrinsic fluorescence caused by biological chromophores. Analysis of the intrinsic fluorescence spectra resulted in differentiation of cancerous and dysplastic lesion from normal tissue with 96% sensitivity and 96% specificity (25). De Veld et al. measured autofluorescence spectra from 155 patients and 97 healthy volunteers and found excellent separation between normal oral mucosa and oral cancer (26). However, in a different article De Veld

et al. report that while autofluorescence spectroscopy can successfully discriminate lesions from normal oral mucosa, classification of different types of lesions with high accuracy was not possible (28). In particular, she reports that autofluorescence spectroscopy could not distinguish benign from malignant oral lesions, due to the large variance in spectra from different pathologic categories.

Autofluorescence imaging has also been used to discriminate oral lesions from the surrounding normal oral tissue in several pilot studies (29-31). Recently, Lane et al. developed a commercial device for visualization of oral tissue autofluorescence (32). In a clinical study of 50 patients, they have observed that abnormal lesions display a loss of fluorescence intensity compared to normal oral mucosa. Based on this diagnostic feature alone, high risk dysplastic and cancerous lesions were differentiated from normal mucosa with 98% sensitivity and 100% specificity.

Most of the fluorescence spectra measured from the oral mucosa, to date, are acquired with fiber probes that sample fluorescence originating from large regions of the stroma as well as from the epithelium. Precancerous changes originate in the epithelium; therefore a probe design that detects fluorescence predominantly from the epithelial layer is likely to improve the diagnostic abilities of fluorescence spectroscopy. Separation of epithelial from stromal signal requires a fiber optics design that measure depth-resolved spectra from multilayered epithelial tissue. Several prior studies have reported fiber optic probe designs that allow for the detection of fluorescence and reflectance spectra with depth selectivity (33-35). Angled illumination fiber probes have been evaluated by measuring in vivo fluorescence spectra from epithelial precancers (36) and by diagnosing oral lesions with polarized reflectance spectroscopy (33). Recently in our lab, a ball-lens coupled probe has been designed and is currently used to obtain spatially resolved fluorescence spectra from normal and neoplastic oral sites in a clinical setting. The

shallow channel of this probe collects fluorescence from approximately 300 microns beneath the probe surface, which corresponds primarily to the epithelium and the superficial stroma (37).

2.5 OPTICAL PROPERTIES OF NORMAL AND ABNORMAL EPITHELIAL TISSUE

Optical spectroscopy has a high diagnostic potential because it can detect biochemical and morphological changes that occur in tissue during neoplastic progression. Cellular and architectural changes, linked to dysplastic progression in epithelial tissue, affect the absorption, scattering and fluorescence properties of tissue, and lead to diagnostically significant differences in clinically measured spectra. This section summarized the major optical properties of epithelial tissue and how these properties are altered by neoplastic development.

Fluorescence in turbid tissue can be described as a three step event. First, excitation light travels into the media and is attenuated by scattering and absorption in the media. Absorption of excitation light by a fluorophore and the emission of fluorescence depend on the absorption coefficient and fluorescence efficiency of the fluorophore. Finally, the remitted fluorescence light travels back to the detector and is further attenuated by scattering and absorption events. Thus, the intrinsic fluorescence signal is distorted by absorption and scattering events. The detected signal from epithelial tissue and its underlying stroma are affected by several main fluorophores, scatterers and absorbers, whose optical properties and distribution in tissue are summarized in this section.

2.5.1 Fluorophores

Pyridine nucleotides and the flavins are the main fluorophores responsible for cellular autofluorescence and play an important role in cellular metabolism (38). Nicotinamide adenine dinucleotide is a major electron acceptor in the oxidative phosphorylation chain of mitochondria and its reduced form (NADH) is fluorescent, having an excitation maximum near 360 nm and an emission maximum near 450 nm. When NADH is not bound to enzymes in the mitochondrial membrane it has an emission maximum at 470 nm. Flavin adenine dinucleotide is another major electron acceptor and its oxidized form, FAD, is fluorescent, having an excitation maximum near 450 nm and an emission maximum near 530 nm (39). Fluorescence excitation-emission matrices (EEMs) of cervical cell suspensions (40-42) indicate that the metabolic indicators NADH and FAD are the main source of cellular fluorescence at 350 nm and 450 nm excitation, respectively. Thus, fluorescence spectroscopy can be used to detect changes in the metabolic state of cells as assessed by the concentration of NADH and FAD.

Another possible source of autofluorescence in cells, are cytokeratin filaments, concentrated around the nucleus and the cell membrane of epithelial cells (43). Studies on the fluorescence properties of wool show that oxidation of the tryptophan residue in keratin results in several fluorescent species that are excited in the 335 to 445 nm range (44). In addition, EEMs of reduced wool fibers show a major peak at 365 nm excitation and 430 emission (45), and EEMs of human fingernail (composed mostly of keratins) show a peak that has a broad excitation from 350 to 400 nm and emission at 430 nm .

Significant autofluorescence has been noted in the structural proteins collagen and elastin. Collagen and elastin autofluorescence is associated with crosslinks (46, 47). There are two major mechanisms of collagen and elastin crosslinks formation. Enzymatically formed crosslinks were believed to be the main fluorophores in collagen at

325 nm excitation (48). A second mechanism of inter-molecular crosslinking of collagen has been reported, age related, and occurs via glycation (48). Several types of fluorescent crosslinks can result, such as pentosidine (excitation maximum 335 nm, emission maximum 385 nm, accounting for 25-40% of total collagen fluorescence), vesperlysine (370 nm, 440 nm, 5% of total fluorescence), crossline (380 nm, 460 nm) and argpyrimidine (320 nm, 380 nm) (48,49). Spectroscopic analysis of cervical stroma indicates that stromal fluorescence is mainly due to collagen crosslinks. In particular, collagen crosslinks, ranging from enzymatically formed crosslinks to advanced glycation endproducts (AGEs) are thought to be the major fluorescence source at 310 to 400 nm excitation (41). Since stroma has multiple fluorophores (crosslinks), Sokolov et al. described the emission spectra from stromal tissue using a linear combination of three set of Gaussian-Lorentzian curves centered at different emission wavelengths. The dominant component of stromal fluorescence at 350 nm excitation has an emission peak at 405 nm (41).

Fluorescence microscope images of viable short term tissue cultures from cervical biopsies show that with dysplasia the epithelial fluorescence at 360 nm excitation increases, while stromal fluorescence decreases (50). In a similar study, high-resolution confocal fluorescence images revealed that cytoplasmic fluorescence in epithelial cells is caused by mitochondrial NADH at 350-360 nm excitation and mitochondrial FAD at 488 nm excitation (51). In normal epithelium, cytoplasmic fluorescence is limited to a thin layer of basal cells, while the rest of the epithelium is dominated by fluorescence originating from the periphery of cells. With the development of precancer in the epithelium, the number of cells with cytoplasmic fluorescence increases, occupying about 2/3 of the whole layer, as in the case of high-grade dysplasia. Confocal images of stroma from normal and precancerous short-term tissue cultures indicate that the major source of

stromal fluorescence comes from fibers organized in a dense matrix. With the progression of dysplasia the density of the matrix decreases, so that the fluorescence properties of the stroma differ immediately under a precancerous lesion and 250-500 μm beneath the basement membrane.

2.5.2 Scatterers

Tissue scattering arises due to the microscopic heterogeneities of refractive indices between extracellular, cellular and sub-cellular components. Using angular measurements of elastic scattering from cells, Mourant et al. (52) identified that cellular scattering is caused by nuclei as well as other cellular organelles. Simulations based on a finite-difference time-domain (FDTD) technique predict an increase in the scattering cross section of precancerous cells, due to changes in nuclear size, optical density and texture (53). In addition, the scattering properties of cells vary not only with dysplasia, but also with epithelial depth. Further FDTD modeling shows that scattering decreases, going from the superficial layer to the intermediate layer, but increases again in the basal/parabasal layer of cervical epithelium (54).

2.5.3 Absorbers

Oxy- and deoxy-hemoglobin are considered to be the main absorber in the visible range of the spectrum and are present in vascularized tissues, such as the stromal layer underlying the epithelium. Hemoglobin has a strong absorption peak near 420 nm; two smaller absorption bands are present in oxy-hemoglobin near 540 and 580 nm. A single absorption peak is found in deoxy-hemoglobin, near 560 nm. Reabsorption of fluorescence by oxy- and/or deoxy-hemoglobin produces valleys in the emitted

fluorescence spectra. With the progression of dysplasia, the density of blood vessels has been reported to increase in the oral cavity (55), and a change in the absorption properties of dysplastic tissue is expected.

2.6 MODELING OF FLUORESCENCE IN TURBID MEDIA

One of the challenges in fluorescence spectroscopy is to develop models that provide quantitative understanding of how biochemical factors influence the optical properties and fluorescence from turbid tissue. Analytical models developed, are usually based on the diffusion theory which is an approximate solution to the transport equation that describes light propagation in a scattering and absorbing media. A second modeling approach involves Monte Carlo simulations.

Analytical models, based on diffusion theory, have been previously developed that can separate the intrinsic fluorescence from the distorting effects of scattering and absorption of turbid media. The validity of the diffusion theory in modeling propagation of light in turbid tissue was tested by several authors (56-58). The diffusion approximation is valid when the scattering properties of the media dominate its absorption properties and the distance between the source and detector fibers is large. In particular, the reduced scattering coefficient of the media, $\mu_s (1-g)$, must be much larger than the absorption coefficient, μ_a , ($\mu_s (1-g) \gg \mu_a$) (59) and there should be a large source/detector separation, such that $r (\mu_s (1-g) > 5)$ (60), where r is the source-detector separation and g is the anisotropy factor.

Chen et al. (56) showed that, with an index-mismatched boundary between the tissue and the outside medium, the diffusion approximation yields a significant error. In epithelial tissues, the epithelium and the underlying stroma have different optical

properties, and these two layers cannot be accurately described by a single homogeneous medium. Moreover, scattering in the epithelium is forward directed, and the condition, $\mu_s (1-g) \gg \mu_a$, is not valid for the epithelial layer. Results from a two layer model showed that light propagation in the bottom layer can be accurately described with diffusion theory; however, that from the top layer was difficult to predict accurately (57, 58). Propagation of fluorescence light in a one layer media for a collimated excitation source and point source of emission has also been modeled with diffusion theory (61). In addition, models that consider different source-detector separations, have been previously considered (62, 63). For example, Hyde et al. (63) developed a model that measures fluorescence detected at different source-detector separations from a media with variable fluorophore concentration. Results show that for the optical parameters used in the model, fluorescence from shallow depths is difficult to predict with diffusion theory. Chang et al. (64) developed an analytical model that describes fluorescence light propagation in two separate layers with different theories. In particular, light from the forward scattering epithelial layer was modeled with Beer-Lambert Law, while the highly scattering stroma was described with diffusion theory. The model was validated by clinically measured data and Monte Carlo simulations, and predicted normal and abnormal fluorescence spectra within 5% accuracy.

Monte Carlo simulations offer a flexible approach to model light propagation in tissue. This approach views light as photon particles and follows their random walk in a scattering and absorbing media. The location and trajectory of a photon in the tissue is determined by two random numbers that describe the path length and the scattering angle. The probability that a photon is scattered or absorbed, is calculated after a given step size. The main advantage of this approach is that it allows for implementation of a multi layered medium and different source-detector geometries. Monte Carlo simulations have

been widely used to analyze fluorescence and reflectance spectra and to validate predictions with clinical measurements. Previously, Zonios et al. (66) used a model based on Monte Carlo simulations to analyze fluorescence measurements from the colon. Monte Carlo simulations have also been used to generate spectra from a two-layered medium and separate the contributions from the epithelial (NADH) and stromal (collagen) fluorescence in in vivo spectra (65). In addition, Monte Carlo simulations are used to investigate the efficiency of different source-detector geometries (33-35). The major disadvantage of Monte Carlo modeling is that it is statistical in nature and requires the simulation of a large number of photons, which is computationally extensive. Thus this model cannot be used routinely to extract optical parameters from in vivo data, but can be implemented to validate other models of fluorescence.

Monte Carlo simulations are used as the main computational approach in this dissertation to generate and analyze depth-resolved fluorescence spectra from multi-layered epithelial tissue. The next section provides a short theoretical background on this simulation technique.

2.7 MONTE CARLO MODELING

In Monte Carlo models, turbid media is represented by one or more homogenous, infinitely wide layers. Each layer is described by a set of input parameters including the thickness D , the refractive index n , the absorption coefficient μ_a , the scattering coefficient μ_s , and anisotropy factor g . The absorption coefficient is defined as the probability of photon absorption per unit infinitesimal pathlength, and the scattering coefficient is defined as the probability of photon scattering per unit infinitesimal pathlength. The anisotropy factor characterizes the change in direction of propagation upon scattering (28).

The two key parameters that determine the photon's propagation path, are the mean free path for photon-medium interaction and the scattering angle. The mean free path is defined by the reciprocal of the total attenuation coefficient, μ_t . The attenuation coefficient can be represented by the sum of the scattering coefficient, μ_s , and the absorption coefficient, μ_a :

$$\mu_t = \mu_s + \mu_a \quad (2.1)$$

At each scattering event the photon trajectory is deflected by an angle, θ , referred to, as the scattering angle. In addition, at the scattering event, the photon is assumed to be deflected symmetrically about the initial axis of propagation at an azimuthal angle ψ . Figure 2.3 illustrates the geometry of a scattering event. In this figure, the scattering angle θ , is defined as the angle between incident photon direction, \hat{s}' , and the scattered photon direction, \hat{s} .

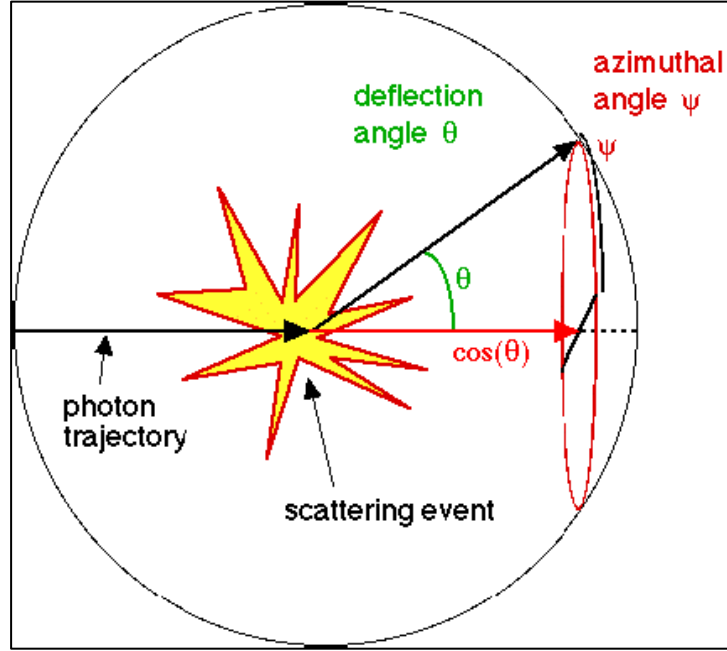


Figure 2.3: Deflection of a photon at a scattering event. The scattering angle or deflection angle is indicated by θ . Adapted from (8).

In Monte Carlo models, the parameters of mean free path and scattering angle are described with probability distribution functions. In particular, the mean free path, indicated as Δs , can be sampled from a probability distribution that depends on the total attenuation coefficient, μ_t . This probability distribution can be expressed as:

$$p(\Delta s) = \mu_t \exp(-\mu_t \Delta s) \quad (2.2)$$

The probability density function for the scattering angle, or more precisely, the probability distribution for the cosine of the deflection angle, $p(\cos \theta)$, is described by the

Henyey-Greenstein phase function. In tissue, scattering is not isotropic, but highly forward directed and therefore the scattering angle probability density function is not uniform. Henyey and Greenstein proposed a scattering phase function that approximates Mie scattering from particles that are similar in size to the wavelengths of light. The Henyey-Greenstein phase function is extensively in used in Monte Carlo models to approximate the scattering phase function in tissue:

$$p(\cos \theta) = \frac{1 - g^2}{2(1 + g^2 - 2g \cos \theta)^{3/2}} \quad (2.3)$$

where the anisotropy factor, g , is the average value of $\cos \theta$. The azimuthal scattering angle is assumed to be uniformly distributed between 0 and 2π .

In Monte Carlo simulations light propagation in tissue is modeled by incrementally propagating a statistically large number of photons through the homogenous layers that represent tissue media. The refractive index, the scattering and absorption coefficients and the anisotropy factor are specific for each layer. After each interaction event, a new mean free path, scattering and azimuthal angles are determined. Photons that are not absorbed and reach the surface of the medium are detected only if they exit under the area defined by the detector radius, and their propagation direction at the exit point is within the collection cone determined by the NA and refractive index of the fiber.

A fixed weight Monte Carlo model is employed for describing fluorescence light propagation in multilayered oral tissue. Chapter 4 provides more details about modeling fluorescence light with Monte Carlo simulation techniques.

Chapter 3: Understanding the biological basis of autofluorescence imaging for oral cancer detection: High resolution fluorescence microscopy in viable tissue.¹

3.1 INTRODUCTION

Oral cancer is one of the most common malignancies worldwide, and carries one of the lowest overall survival rates (1, 2). Despite the easy accessibility of the oral cavity to examination, most patients present with advanced disease, when treatment is associated with higher morbidity, more expense, and less success than earlier interventions. Early detection of oral cancer can greatly improve treatment outcomes. Unfortunately, there is no method to adequately screen and diagnose early oral cancers and pre-cancers because detection still relies on clinicians' ability to visually identify subtle neoplastic changes, and to distinguish these changes from more common inflammatory conditions. Technologic advances are needed to assist clinical diagnosis of oral cancer.

Autofluorescence imaging has been used successfully to rapidly and non-invasively distinguish malignant oral lesions from surrounding tissue in several pilot studies (29-31). A low-cost device for visualization of oral autofluorescence was used to identify high-risk precancerous and cancerous lesions with 98% sensitivity and 100% specificity based on the loss of fluorescence in abnormal sites compared to normal tissue (32). This device is now commercially available.² Autofluorescence spectroscopy has

¹ This chapter is modified from: I. Pavlova, M. Williams, A. El-Naggar, R. Richards-Kortum, A. Gillenwater. Clinical Cancer Research (in press).

² <http://www.velscope.com>.

also emerged as a non-invasive technology for diagnosing precancers and cancers in several organ sites (16-20, 68). In the oral cavity, several groups used fluorescence spectroscopy to distinguish oral lesions from normal tissue with high specificity and sensitivity (ranging from 81% to 100%) (23-28). Despite preliminary clinical evidence indicating the potential role of fluorescence imaging and spectroscopy for improved detection of early neoplasia in the oral cavity, there is limited understanding of the biological basis for optical changes associated with neoplastic transformation of oral tissue.

The diagnostic potential of fluorescence imaging and spectroscopy lies in the ability to non-invasively probe alternations in tissue morphology and biochemistry that occur during malignant progression. Fluorescence in epithelial tissue originates from multiple fluorophores (molecules that when excited by light emit energy in the form of fluorescence) and is influenced by absorption and scattering as light propagates through the epithelium and stroma. In the cervix, which is histologically similar to oral tissue in many respects, epithelial fluorescence originates from the cytoplasm of cells and is linked to the metabolic indicators NADH and FAD, which increase as dysplasia develops (50, 51, 39). Neoplastic progression is also associated with increased nuclear size and chromatin texture, which leads to increased epithelial scattering (69, 70).

Carcinogenesis involves complex biochemical signaling between the epithelial cells and the surrounding extracellular matrix (71-73). Subepithelial chronic inflammatory microenvironments express products that induce angiogenesis and degradation of the extracellular matrix, which in turn stimulates promotion of cancer in the epithelium (74). Since altered stromal properties may precede epithelial changes during carcinogenesis (75), understanding the autofluorescence patterns in the stroma and the impact of inflammation on these patterns, may help explain spectral differences in

normal oral mucosa and early dysplasia. Confocal images and spectroscopy analysis indicate that collagen crosslinks are the major fluorophore in stroma in the cervix (41). Remodeling of the stroma during cervical carcinogenesis leads to structural changes in the collagen matrix accompanied by loss of collagen fluorescence (51) and a decrease in stromal scattering (76). Thus, to harness the full potential of fluorescence based diagnosis, it is important to clarify how both epithelial and stromal alterations in oral tissue contribute to the changes in the overall optical properties during carcinogenesis.

Epithelial and stromal autofluorescence patterns can be directly visualized using fluorescence microscopy of viable *ex vivo* oral tissue. High spatial resolution is necessary to assess variability in the microscopic origin of autofluorescence within the epithelial or stromal layer. Here I qualitatively and quantitatively examined the distribution of autofluorescence at the cellular level in viable oral tissue using laser scanning confocal fluorescence microscopy. Our first objective was to characterize the origins of autofluorescence in normal oral mucosa and to assess how anatomical site variations affect these autofluorescence patterns. Second, I investigated how inflammation and dysplasia alter the autofluorescence properties of oral tissue. Third, I compared the autofluorescence patterns of oral cancers with different grades of differentiation. Understanding the biological basis underlying alteration in autofluorescence in epithelial and stromal layers during oral carcinogenesis will facilitate development of accurate diagnostic algorithms to differentiate normal, benign, precancerous, and cancerous oral tissue; an important step needed to achieve the full diagnostic potential of this technology.

3.2 METHODS

3.2.1 Biopsy collection and preparation of tissue slices

Clinical protocols were approved by the Institutional Review Boards at The University of Texas M. D. Anderson Cancer Center (MDACC), The University of Texas at Austin, and Rice University. A clinically normal and one or more clinically abnormal biopsies were obtained from each consenting patient at MDACC. Biopsies were immediately stored in iced phenol-free DMEM media (Sigma-Aldrich, St. Louis, MO) and kept there until examination. Transverse tissue slices approximately 200 μm thick were obtained from each fresh biopsy using a Krumdieck tissue slicer (Alabama Research and Development, Munford, AL). Note that prior to fluorescence imaging, slices were not fixed or processed in any way. Each unstained and unprocessed tissue slice was imaged with an inverted Leica SP2 AOBS confocal laser scanning fluorescence microscope (Leica Microsystems, Wetzlar, Germany) within 12 hours after biopsy collection. Detailed procedures for tissue cutting and preparation for imaging are described elsewhere (50, 51).

3.2.2 Confocal Microscopy and Image Collection

Optical sections from each tissue slice were obtained at both UV and 488 nm excitation using a 40 X oil-immersion objective. UV excitation was provided by an argon laser, at 351 nm and 364 nm, and an Ar/Kr laser was used for 488 nm excitation. Prior analysis on cervical tissue (41) has indicated the UV excitation (at 351 nm and 364 nm) targets predominantly NADH in the epithelium and collagen fibers in the stroma, while 488 nm excitation targets FAD in the epithelium in addition to stromal fibers. The oil-

immersion objective had a numerical aperture of 1.25 and a working distance of 80 μm . Single optical sections of each region of interest were obtained at a fixed depth of 15 μm beneath the cover slip. The fluorescence signal at UV excitation was collected from 380 to 500 nm, whereas at 488 nm excitation, fluorescence was collected from 505 to 650 nm. The field of view for each image was 375 $\mu\text{m} \times 375 \mu\text{m}$. The lateral resolution was limited by the pixel size of the detector and was 0.73 μm . The axial step size varied from 1.0 to 1.2 μm . In order to perform quantitative comparisons all images were taken with the same detector settings and corrections for laser power variations were performed prior to analysis.

In tissue slices with well defined layered structure (normal, inflammation, and dysplasia), adjacent images were acquired to include the whole thickness of the epithelium and the more superficial stromal regions down to about 1 mm in depth. In tissue slices without a defined structure (invasive carcinoma), several images were taken, starting from what appeared to be the surface of the tissue slice and ending about 1 mm below this edge. Adjacent confocal images were tiled together in order to provide large-scale mosaic view of each region of interest. Some adjacent images had a considerable area of overlap, which was cropped off prior to assembly of the mosaic view. Brightness and contrast was readjusted by the same amount for all confocal images prior to display.

3.2.3 Histology

After imaging, tissue slices were fixed in 10% formalin and prepared for pathological examination using standard protocols. Hematoxylin and eosin (H&E) stained sections were obtained from each imaged tissue slice and reviewed by experienced head and neck pathologists. A pathologic diagnosis of normal, dysplasia or cancer was rendered; hyperkeratosis and hyperplasia were treated as normal for further

analysis. In addition, the absence or presence (and degree) of inflammation was determined.

3.2.4 Image analysis: average fluorescence intensity and redox ratio calculations

A qualitative assessment of autofluorescence patterns was performed initially, comparing variations by anatomic site and pathologic diagnosis. Then the UV and 488 nm images were overlaid and examined visually. In normal and precancerous tissue slices, the fluorescence patterns were examined in the superficial, intermediate and basal epithelium as well as in the superficial and deep stroma. Tissue slices diagnosed with invasive cancers displayed a loss of layered morphology. After visually identifying common morphological and fluorescence patterns, tumor images were divided into subregions, including regions with tumor cells and surrounding fiber matrix.

Quantitative image analysis was performed in the following manner: After background subtraction, the UV and 488 nm image for each tissue slice were overlaid. Several regions containing cells and stroma were outlined based on the appearance of the overlaid images. The average grayscale values of all pixels within an outlined region were calculated in order to obtain the mean fluorescence intensity value (FIV) for each region. These calculations were performed for both the UV and 488 nm images. In addition the average redox ratio value was calculated for the cellular regions in each tissue slice by dividing the mean FIV at 488 nm excitation for the region by the sum of the mean FIV at UV and the mean FIV at 488 nm excitation for the same region. The redox ratio reflects changes in the concentrations and redox potentials of the metabolic indicators NADH and FAD, and has been used in previous research to monitor cellular metabolism (39, 50).

Finally, all tissue slices were grouped according to their pathologic diagnosis, and the mean FIV and redox ratio were calculated for each diagnostic category. For normal, inflammatory and dysplastic samples, which retain a well-defined layered morphology, tissue slices were grouped by both pathologic diagnosis and anatomic site. For tissue slices from cancerous lesions, samples were grouped by diagnosis regardless of anatomic site. The average FIV was calculated for cellular and stromal regions by averaging the mean FIV for each tissue slice for that diagnostic group and anatomic site. The average FIVs were used to compare changes in the fluorescence characteristics of oral tissue that occur in association with neoplastic development. In a similar manner, the average redox ratio was obtained for each diagnostic group.

3.3 RESULTS

A total of 49 oral biopsies were obtained in this study. The biopsies were subdivided according to oral anatomical type and pathologic diagnosis. Oral biopsies from five different anatomical types were imaged including the tongue, palate, gingiva, buccal mucosa and the floor of mouth. Each biopsy was assigned to the following pathological diagnostic subcategories: normal without inflammation (8 tongue biopsies, 2 palate biopsies, 2 gingival biopsies, 2 buccal mucosa biopsies, and 4 floor of mouth biopsies); normal with mild to moderate inflammation (2 tongue biopsies, 2 gingival biopsies, and 3 floor of mouth biopsies); normal with severe inflammation (3 tongue biopsies); dysplasia (6 tongue biopsies, 2 palate biopsies); well differentiated carcinoma (3 tongue biopsies, 1 palate biopsy, and 2 floor of mouth biopsies); moderately differentiated carcinoma (5 tongue biopsies, and 1 floor of mouth biopsies); poorly differentiated carcinoma (1 palate biopsy).

	Tongue	Palate	Gingiva	Floor of mouth	Buccal	Total
Normal without inflammation	8	2	2	4	2	18
Normal with mild to moderate inflammation	2	0	2	3	0	7
Normal with severe inflammation	3	0	0	0	0	3
Dysplasia	6	2	0	0	0	8
Well differentiated carcinoma	3	1	0	2	0	6
Moderately differentiated carcinoma	5	0	0	1	0	6
Poorly differentiated carcinoma	0	1	0	0	0	1
Total						49

Table 3.1: Total number of biopsies for each diagnostic category and anatomic site.

3.3.1 Normal oral mucosa autofluorescence patterns

Figure 3.1 displays confocal images at UV and 488 nm excitation from a representative normal tongue tissue slice. At UV excitation, most of the epithelial fluorescence originates from the cytoplasm of cells occupying roughly the lower 2/3 of the epithelial layer (Figure 3.1 A). At 488 nm excitation, these same cells have less cytoplasmic fluorescence compared to the upper 1/3 of the epithelium (Figure 3.1 B). Strong stromal autofluorescence at both excitation wavelengths originates from a dense matrix of structural fibers and does not vary significantly with depth.

Autofluorescence characteristics of normal oral mucosa from different anatomical sites are compared in Figure 3.2. Oral epithelium often retains a superficial keratin-containing layer which is highly fluorescent. I observed the presence of this highly fluorescent superficial layer in epithelia from the palate and gingiva (Figure 3.2 A and B). In contrast, epithelia from the floor of mouth, buccal mucosa and the tongue (Figure 3.2 C and D and Figure 3.1) display a weakly fluorescent superficial layer. Deep to this superficial layer, autofluorescence patterns of epithelia in all tissue sites except the gingiva are generally similar. Gingival epithelia, in contrast to other oral sites such as the tongue (Figure 3.1), is dominated by cells that have low fluorescence at UV excitation but high fluorescence at 488 nm excitation. The diminished cytoplasmic fluorescence at UV excitation was observed in all gingival samples, although the number of gingival samples examined was limited.

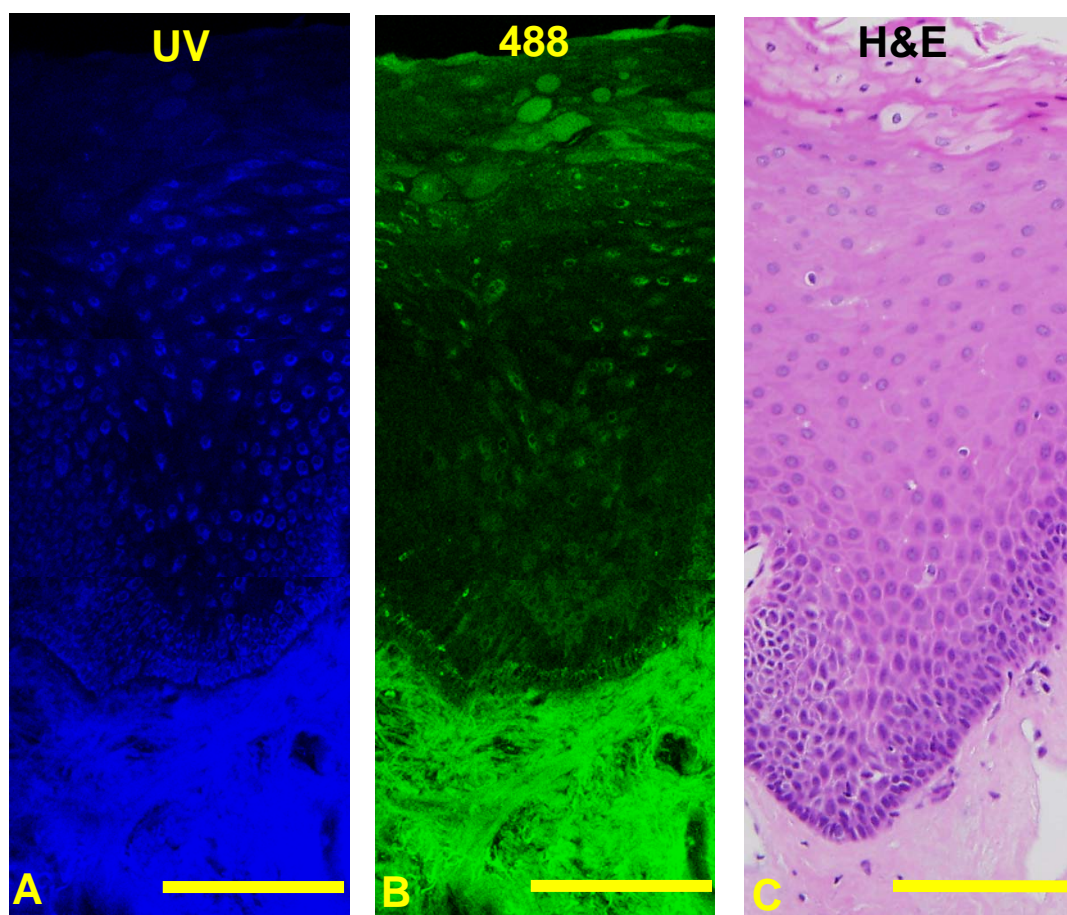


Figure 3.1: Fluorescence and histologic images of normal tongue without inflammation: Confocal fluorescence images at (A) UV excitation, (B) 488 excitation and (C) H&E image. Scale bars represent 200 μm in the confocal images and 125 μm in the H&E image. Note that epithelial fluorescence increase with depth at UV excitation and slightly decrease at 488 nm excitation.

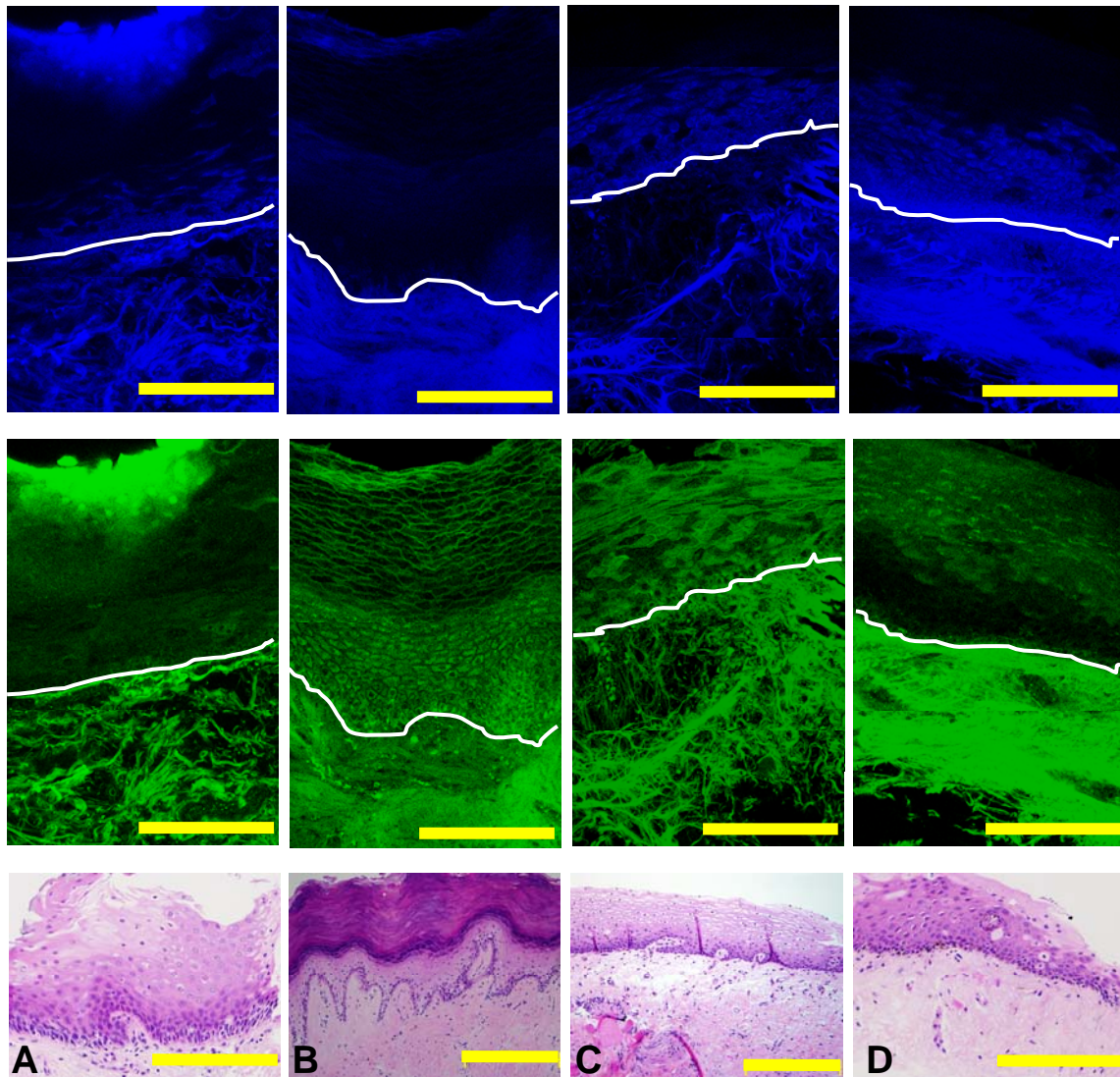


Figure 3.2: Fluorescence and histologic images of four normal oral sites without inflammation. Confocal fluorescence images at both UV (top row) and 488 nm excitation (middle row) and H&E image (bottom row) from (A) palate; (B) gingiva; (C) floor of mouth and (D) buccal mucosa. White line indicates the approximate location of the basement membrane. Scale bars represent 200 μm . Note that the superficial layer is significantly more fluorescent in the palate, then in other anatomical sites. Gingival epithelium displays a loss of fluorescence at UV excitation, which is unusual for other normal sites.

3.3.2 Autofluorescence patterns in inflammatory and dysplastic oral tongue tissue

Representative fluorescence images of oral tongue lesions diagnosed as normal, non-dysplastic epithelium with severe inflammation (Figure 3.3A) and mildly dysplastic epithelium with mild to moderate inflammation (Figure 3.3 B) are compared. Mild dysplasia and severe inflammation can be distinguished based on differences in epithelial fluorescence at UV excitation. A large decrease in fluorescence at UV excitation is observed in the normal basal epithelium overlying inflammatory stroma compared to normal non-inflammatory tongue epithelium (Figure 3.1 A). In contrast, dysplastic epithelium displays a small increase in fluorescence at UV excitation, compared to normal non-inflammatory tongue epithelium. Thus, the representative images in Figures 3.3 indicate that dysplastic epithelium is significantly more fluorescent than the normal basal epithelium overlying severely inflamed stroma. Images from a non-dysplastic floor of mouth sample with mild to moderate inflammation in the stroma show a similar loss of epithelial fluorescence at UV excitation as in the tongue (data not shown).

Stromal areas directly beneath the basement membrane in both the inflammatory and the dysplastic examples exhibit a large loss in fluorescence at UV and 488 nm excitation. In the loose stromal matrix evident in both samples, autofluorescence signals originate predominantly from cells rather than from fibers as seen in normal oral tissue. This shift in origin of stromal fluorescence from fibers to cells, which is more obvious in the severe inflammation case, appears to be associated with the influx of inflammatory cells in this area, as confirmed in H&E images (black arrows in Figure 3.3). In the dysplastic example, these stromal changes affect only the region 100-200 μm below the basement membrane. In particular, stromal fluorescence and fiber density decrease predominantly in areas underling the epithelium, whereas autofluorescence patterns of deeper stroma appear to be similar to normal stroma.

3.3.3 Quantitative analysis of fluorescence in normal, benign, and dysplastic oral tongue slices

Figures 3.4 A and B illustrate how images of tissue slices with well defined layered morphology were divided into subregions for quantitative analysis. The superficial epithelial region includes cells that retain keratin (white area on Figure 3.4 B). Non-keratinized epithelial cells displaying a weak cytoplasmic fluorescence signal at UV excitation are defined as type 1 cells (green area on Figure 3.4 B). At 488 nm excitation; type 1 cells display an increased cytoplasmic fluorescence signal compared to the rest of the nonkeratinized epithelium. Epithelial cells with a strong cytoplasmic fluorescence signal at UV excitation are defined as type 2 cells (blue area on Figure 3.4B). Stromal region 1 occupies an area approximately 100 -200 μm below the basement membrane. Stromal region 2 is situated below stromal region 1, and occupies an area that is about 200-500 μm deep. For all tissue slices obtained from the tongue, the mean fluorescence intensity value was calculated for each region by diagnostic category for slices diagnosed as normal, inflammatory or dysplastic; results are shown in Figures 3.4 C and D.

In normal tongue epithelium, type 2 cells display the highest average fluorescence intensity at UV excitation but the lowest value at 488 nm excitation. The average redox values for type 2 cells are 1.8 times lower than the redox values for type 1 cells (data not shown) indicating an increased metabolic activity in this region of the epithelium. In all normal tongue samples, type 2 cells occupied more than half of the non-keratinized part of the epithelium. These data suggest that the majority of normal tongue epithelium is occupied by cells with bright UV cytoplasmic fluorescence and weak 488 nm cytoplasmic fluorescence.

Average fluorescence intensities for type 2 cells at UV excitation (Figure 3.4 C) illustrate the differences in epithelial fluorescence between normal, inflammatory and

dysplastic tongue samples. In dysplasias, fluorescence from type 2 cells increases by a factor of 1.3 on average compared to normal tongue. In contrast, inflammatory tongue tissue displays a large drop in the average fluorescence intensity of type 2 cells, which is more pronounced for samples with severe inflammation. Thus, type 2 cells in dysplastic lesions exhibit an increase in UV excited fluorescence by more than a factor of 4 compared to lesions with severe inflammation. These modifications in epithelial fluorescence at UV excitation are not accompanied by significant changes in the 488 nm excited fluorescence.

Average fluorescence values from stromal region 1 (Figures 3.4 C and D) reveal that both inflammatory and dysplastic lesions are characterized by a large loss of stromal fluorescence at both excitations. Mild to moderate inflammation and dysplasia show a similar drop in fluorescence at UV excitation (by more than a factor of 2) compared to normal values. Severe inflammation displays an even more pronounced decrease (by factor of 4 at UV excitation) compared to mild to moderate inflammation and dysplasia. The degree of inflammation also determines the depth of the affected stromal areas. Severe inflammation displays a very large loss of fluorescence in both stromal region 1 and 2. In mild to moderate inflammation and dysplasia, fluorescence from stromal region 2 is higher compared to severe inflammation.

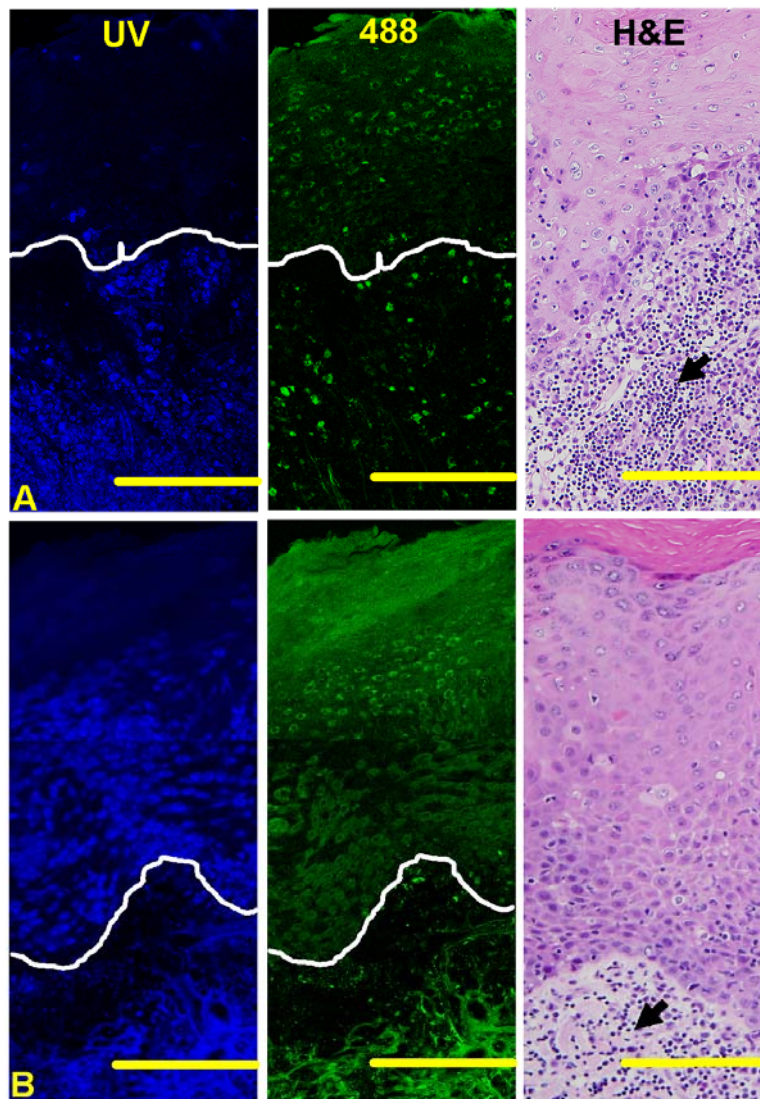


Figure 3.3: Fluorescence patterns of (A) inflammation and (B) mild dysplasia in the oral tongue. Mosaic of confocal fluorescence images at UV (left), 488 nm excitation (middle) and H&E images (right). The histopathologic diagnosis of (A) is normal, non-dysplastic epithelium with severe inflammation and of (B) is mildly dysplastic epithelium with mild to moderate inflammation. White line indicates the approximate location of the basement membrane. Scale bars in the confocal images represent 200 μm and scale bars in the H&E images represent 120 μm . Arrow heads mark lymphocytic infiltration.

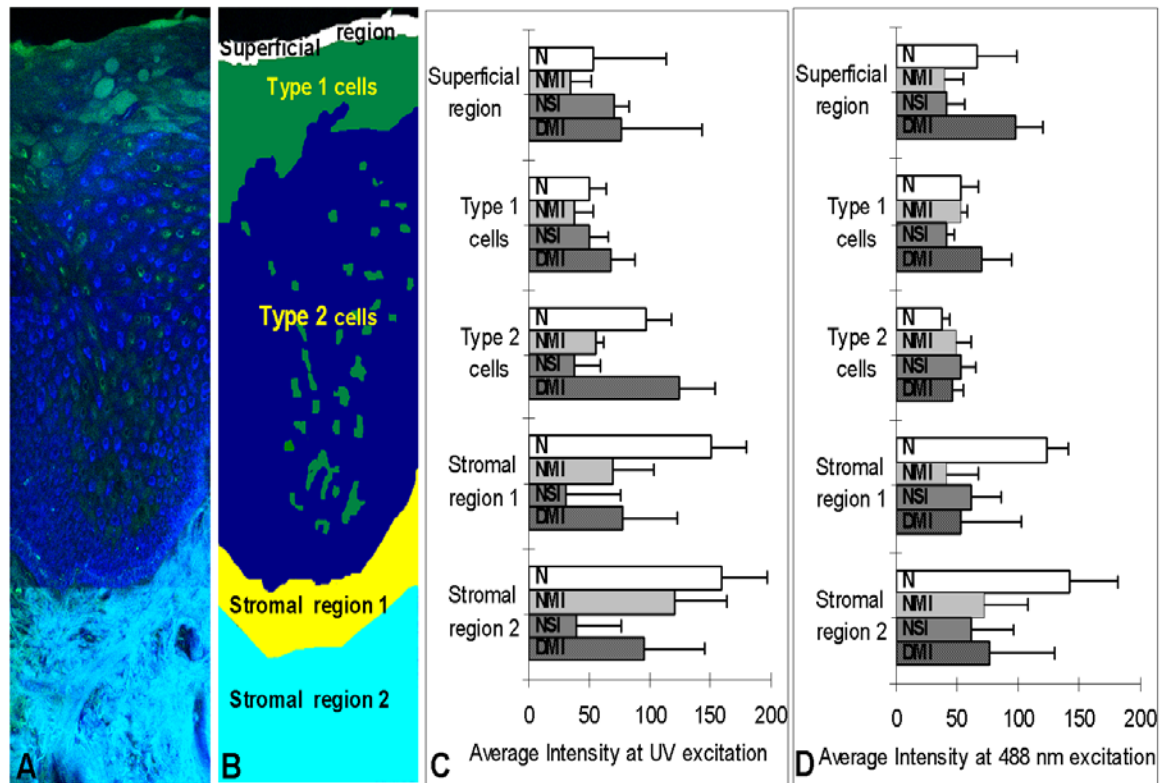


Figure 3.4: Quantitative analysis of the average fluorescence intensities of all normal, inflammatory and dysplastic oral tongue tissues. (A) Overlaid UV and 488 nm excited fluorescence images and (B) a simplified cartoon of normal tongue showing the approximate distribution of the epithelial and stromal subregions. Type 2 cells display easily visualized cytoplasmic fluorescence at UV excitation; while type 1 cells exhibit a weak cytoplasmic signal at UV excitation. Stromal region 1 includes stroma that is 100 -200 microns below the basement membrane, whereas stromal region 2 represents deeper stroma. Average fluorescence intensities at (C) UV excitation and (D) 488 nm excitation for each epithelial and stromal region. Error bars represent one standard deviation. Legend key for the diagnostic categories: N-Normal without inflammation (n=8); NMI-Normal with mild to moderate inflammation (n=2); NSI- Normal with severe inflammation (n=3); DMI-Dysplasia with mild to moderated inflammation (n=6).

3.3.4 Autofluorescence of well, moderately and poorly differentiated carcinomas

Figure 3.5 displays representative confocal fluorescence images of well, moderately and poorly differentiated carcinomas, while Figure 3.6 A and B show how images of cancers were divided into three subregions. A common feature present in all cancers is the absence of layered morphology and the aggregation of cancer cells in clearly defined regions (Figure 3.6 A and B). Type 1 cancer cells are characterized by an absence of cytoplasmic fluorescence at UV excitation but a strong cytoplasmic signal at 488 nm excitation. Type 2 cancer cells display an easily visualized cytoplasmic fluorescence at UV excitation. Cancer cells are surrounded by matrix fibers. Matrix regions with dense, brightly fluorescent fibers and without a significant cellular component are defined here as fibrous stroma (light blue region in Figure 3.6 B). Matrix regions with a dominant cellular component, consisting of inflammation and atypical cells are very heterogeneous and difficult to outline. These regions were excluded from the analysis of cancer images and are not shown in Figure 3.6. Some tissue slices contained submucosal tumors. Figure 3.5 A shows an example of a well differentiated submucosal tumor underneath a mildly dysplastic surface epithelium. Cells from the surface epithelium overlying submucosal tumors were excluded from quantitative analysis of carcinomas.

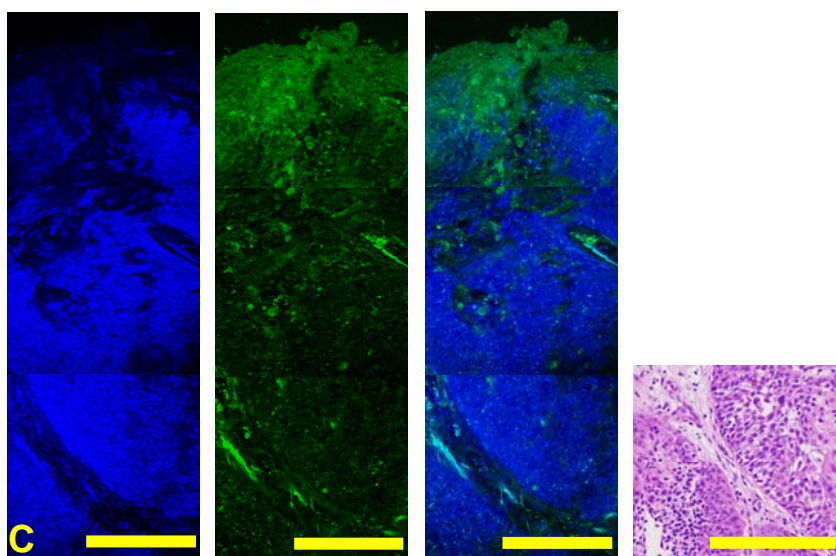
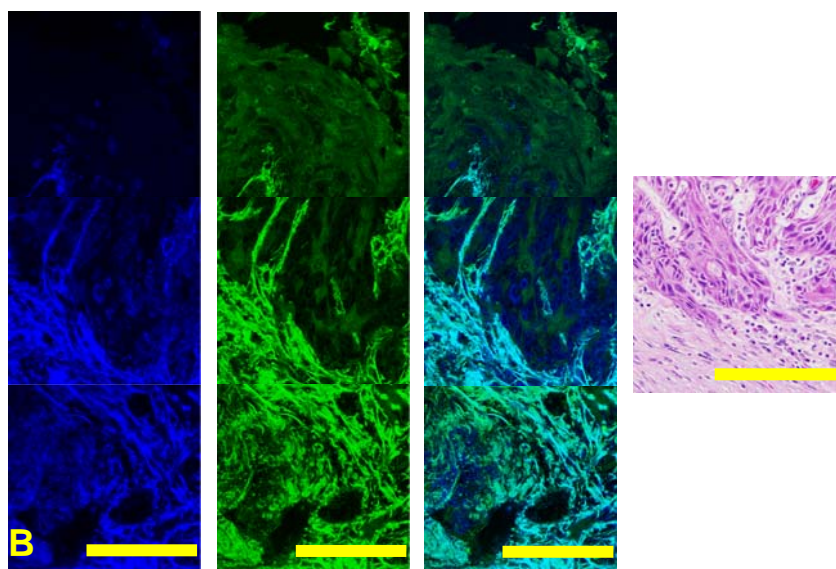
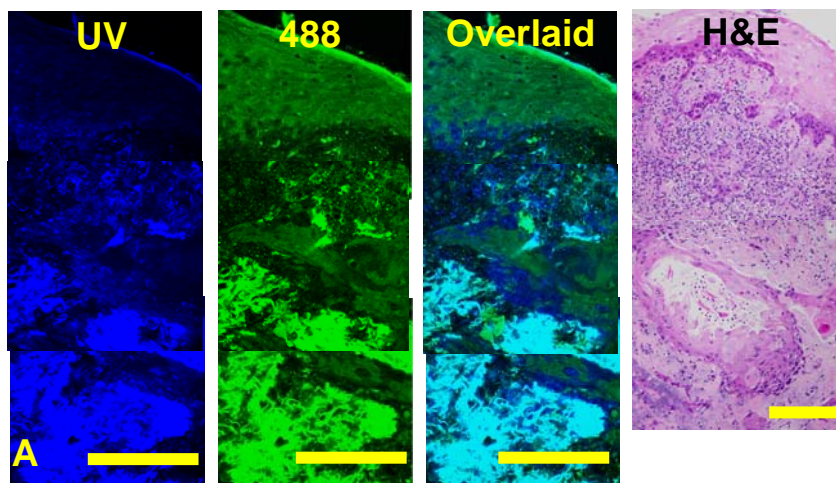


Figure 3.5: Fluorescence patterns of invasive tumors in the oral cavity. Confocal fluorescence images at UV (first column) and 488 nm excitation (second column); overlaid UV and 488 nm images (third column) and H&E images (fourth column). (A) Mildly dysplastic epithelium overlaying well differentiated submucosal carcinoma in the tongue; (B) Moderately differentiated carcinoma in the tongue; (C) Poorly differentiated carcinoma in the palate (C). Scale bars represent 200 microns.

Average fluorescence intensity values for type 1 and type 2 cancer cells are compared in Figure 3.6 C and D. The poorly differentiated tumor shows the highest fluorescence intensity at UV excitation for both cell types and the lowest fluorescence at 488 nm excitation. Average redox values for type 1 and 2 cancer cells are shown in Figure 3.6 D. The poorly differentiated carcinoma displays the lowest redox values, especially for type 2 cells. Since redox values are inversely proportional to metabolic activity, these results provide support for the clinical tenet that poorly differentiated carcinoma cells are more metabolically active on average than cells in more differentiated tumors. In addition, average fluorescence intensity values show that fibrous stroma in well differentiated tumors generally has higher fluorescence at both excitation wavelengths when compared to less differentiated carcinomas.

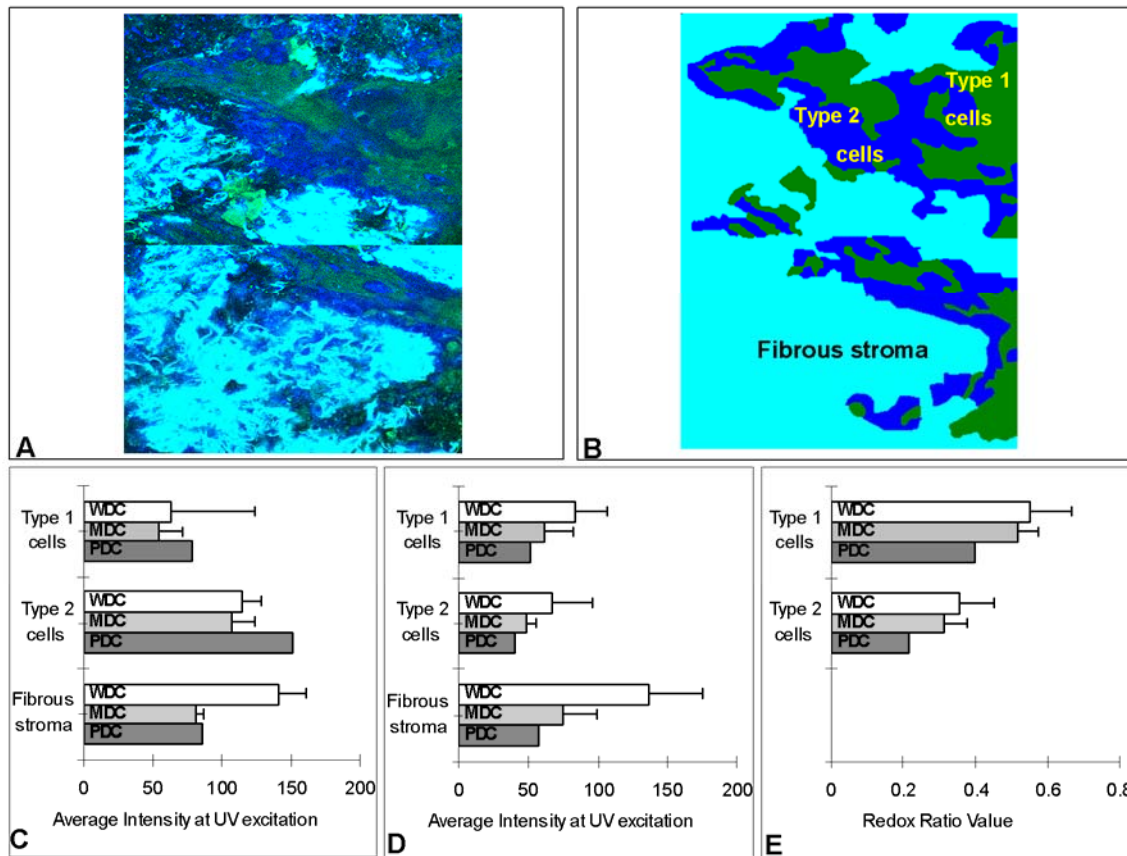


Figure 3.6: Quantitative analysis of invasive tumors. (A) Overlaid UV and 488 nm excited fluorescence images and (B) a simplified cartoon of an invasive tumor showing the distribution of type 1 (green regions) and type 2 (dark blue regions) cancer cells surrounded by fibrous stroma (light blue region). Type 2 cancer cells display easily visualized cytoplasmic fluorescence at UV excitation; while type 1 cancer cells exhibit weak cytoplasmic signal at UV excitation. Fibrous stroma includes matrix with a dominant fiber component. Average fluorescence intensities at (C) UV and (D) 488 nm excitation for each subregion and (E) average redox ratio values for type 1 and type 2 cancer cells. Error bars indicate one standard deviation. Legend key for diagnostic categories: WDC-Well differentiated carcinoma (n=6); MDC-Moderately differentiated carcinoma (n=6) ; PDC-Poorly differentiated carcinoma (n=1).

3.4 DISCUSSION

Understanding how optical properties are altered during oral carcinogenesis is critical for optimizing diagnostic technologies for oral cancer detection based on autofluorescence imaging and spectroscopy. In this study I used high resolution microscopy to investigate patterns of autofluorescence in normal oral mucosa and in benign and neoplastic oral lesions. Our results demonstrate that the autofluorescence properties of oral tissue vary based on the anatomical site within the oral cavity and the pathologic diagnosis. The fluorescence signals from epithelial and stromal layers can change independently of other tissue layers. This has important implications for clinical diagnosis of oral lesions using fluorescence imaging and spectroscopy.

When normal oral tissue is illuminated by UV light, most of the epithelial autofluorescence that is generated originates from the cytoplasm of cells occupying the basal and intermediate layers. Similar findings were found using confocal images of cervical tissue, where the epithelial fluorescence at UV excitation originates partially from the cytoplasm of metabolically active cells and the main fluorophore responsible for this signal was shown to be NADH (19, 29). In normal, non-dysplastic tongue and FOM tissue, the presence of inflammation within the lamina propria is characterized by a significant decrease in fluorescence from the lower epithelial layers at UV excitation. Several investigators have suggested that in benign lesions such as lichen planus, the large influx of inflammatory cells under the basement membrane triggers apoptosis and changes the proliferation rate of epithelial cells, which would also affect the autofluorescence of these cells (51, 78). In contrast, epithelial dysplasia in the tongue exhibited a small increase in epithelial fluorescence at UV excitation. A similar pattern

was previously observed in dysplastic cervical tissue and was attributed to increased cellular metabolism (50).

In normal oral tissue, stromal fluorescence originates from structural fibers such as collagen. Indeed, collagen crosslinks are believed to be the dominant fluorophores in normal stroma and the optical signatures of these crosslinks are quite different from that of epithelial NADH and FAD (41). With the appearance of inflammation, a large loss of stromal fluorescence is noticed, especially in areas close to the basement membrane. This trend is observed in inflammatory tissue, irregardless of anatomical site and the degree of inflammation correlates well with the extent of the fluorescence loss. I speculate that the reduction in stromal fluorescence in the presence of chronic inflammation is linked to the displacement of structural fibers by the infiltrating lymphocytes which are much less fluorescent, and also promote expression of matrix degrading proteases leading to breakdown of collagen crosslinks (74). A study of the distribution of collagen fibers in human gingiva found that collagen types I and III are lost in stromal tissue with progression of inflammation (79). In vivo multiphoton microscopy images of hamster cheek pouch tissue demonstrated that number and length of collagen fibers is greatly diminished with increasing severity of inflammation (80).

Our results demonstrated a marked loss of stromal fluorescence in dysplastic lesions similar to that observed in normal mucosa with mild to moderate inflammation. Since most of the dysplastic samples in this study also had mild to moderate inflammatory infiltrate in the lamina propria, the reduction of stromal fluorescence is most likely due to the presence of chronic inflammatory cells. Gannot et al also documented increasing levels of subepithelial inflammatory infiltrate (sometimes referred to as lichenoid inflammation) in oral tissue during progression from normal to dysplasia to carcinoma (81). A second investigation found that stromal T cells increased by roughly a factor of 2

in mild dysplasias, and by about 5-fold in moderate and severe dysplasia compared to normal oral tissue (82).

In vivo fluorescence spectroscopy and imaging evaluations consistently find that oral lesions display a loss of fluorescence intensity when compared to normal oral tissue. Some investigators have extracted the intrinsic fluorescence spectra from in vivo fluorescence spectra in the cervix (83) and the oral cavity (25) with a mathematical model. They have found that in the cervix and the oral cavity the intrinsic fluorescence spectra can be composed of two spectra components, NADH and collagen, and that the NADH contribution increases whereas the collagen contribution decrease as lesions become more malignant. In both the cervix and oral cavity, the decrease in collagen contribution was larger than the increase in NADH contribution. These results are in agreement with the autofluorescence patterns from normal and dysplastic oral tongue tissue summarized in this study. Moreover, the loss of fluorescence intensity in oral lesions, as observed in both autofluorescence spectra and images, can be explained mostly by changes in stromal optical and morphologic properties. Lane et al attribute the loss of autofluorescence signal in images of oral precancerous and cancerous lesions primarily to the breakdown of the collagen matrix and increased hemoglobin absorption and secondarily to epithelial factors, such as increased epithelial scattering and thickness (32). Previously Drezek et al have shown with Monte Carlo simulations of fluorescence spectra that most of the in vivo fluorescence signal in cervical tissue (about 80% in normal cervix tissue and 70% in dysplastic tissue) originates from the stroma. She concludes that the decreased fluorescence in dysplastic cervical tissue is due more to the reduction of stromal collagen fluorescence than changes in the contribution from epithelial NADH fluorescence (65).

Here I show that both inflammatory and dysplastic oral tongue tissue display a large decrease in stromal fluorescence, especially in the superficial stroma, but have very different fluorescence patterns in the epithelium. Imaging such lesions with optical devices or probes that measure mostly stromal fluorescence may result in similar findings of loss of fluorescence intensity and thus fail to distinguish benign inflammation from dysplasia. Current results suggest that a possible way to distinguish benign inflammation from dysplastic lesions is to probe differences in epithelial fluorescence in addition to stromal fluorescence. Moreover, while stromal fluorescence decreases with malignant progression at both UV and 488 nm excitations, significant differences in epithelial fluorescence are observed only at UV excitation. Thus, the diagnostic ability of fluorescence imaging and spectroscopy for differentiating benign inflammations from dysplastic lesions could be improved by using excitation wavelengths in the UV range. Recently it was shown that a simple imaging device can be used as an aid to successfully detect and identify high-risk pre-invasive lesions with excitation wavelengths in the 400 to 460 nm range (32). While the success of this device is quite exciting, our results suggest that the accuracy of such imaging devices in distinguishing different types of oral lesions, such as benign inflammation and dysplasia might be enhanced by using UV excitation in addition to higher excitation wavelengths.

Bright autofluorescence was noted from the superficial, keratinized epithelial layer, which is often present in normal oral tissue from specific anatomical sites such as the palate and the gingiva, and also in clinically apparent leukoplakia. This superficial layer is composed of keratinized cells that have different scattering (70) and fluorescence signatures (84) than the rest of the epithelium. The presence of a thick, keratinized superficial layer can influence both the intensity and emission peak of in vivo fluorescence spectra. Muller et al. reported that fluorescence spectra from keratinized oral

mucosa exhibit a shift to the red and a lower intensity compared to nonkeratinized tissue. They explained these differences by a reduction of the depth of penetration of excitation light due to scattering from the keratin layer, which results in an increased NADH and decreased collagen contribution to the measured spectra. Thus, in order to classify dysplastic tissue from cancers with good accuracy, they advocated that non-keratinized and keratinized mucosa should be divided in to different groups (25). Our results support this view, and also suggest that this subdivision would be important for distinguishing non-dysplastic from dysplastic oral mucosa.

Results here suggest that the diagnostic potential of fluorescence spectroscopy and imaging can be improved by designing optical probes or devices that can selectively measure signal from either the epithelium or the stroma. Excitation wavelengths in the UV range may also improve the accurate diagnosis of different types of oral lesions.

Chapter 4: A Monte Carlo model to describe depth selective fluorescence spectra of epithelial tissue: Applications for diagnosis of oral precancer.³

4.1 INTRODUCTION

Autofluorescence imaging of the oral cavity has emerged as a promising non-invasive technique to aid visualization and identification of premalignant and malignant oral lesions from benign lesions and normal oral mucosa (29-32). Autofluorescence spectroscopy can also identify oral dysplasia and cancer with high specificity and sensitivity (24-28). During neoplastic progression, the optical properties of both the superficial epithelium and the underlying stroma are altered. These changes can include an increase in epithelial cell scattering, increased stromal hemoglobin content and decreased structural protein fluorescence within the stroma. Many research groups have developed analytical models to analyze fluorescence spectra collected in vivo in terms of these biochemical and morphologic changes (25, 83, 85-87). Accurate biological interpretation of autofluorescence spectra of precancer and cancer diagnosis depends, in part, on prior knowledge of the key optical parameters associated with cancer progression and a detailed understanding of how these optical parameters can alter the intensity and shape of the in vivo spectra.

Interpretation of tissue spectra is made more complex because measured data often contain contributions from both the epithelium and stroma. Recently, a number of groups have developed fiber optic probes to acquire fluorescence spectra with depth

³ This chapter is modified from: I. Pavlova, R. Schwarz, M. Williams, A. El-Naggar, A. Gillenwater, R. Richards-Kortum, Journal of Biomedical Engineering (submitted).

selectivity (33, 34, 93). Schwarz et al have used a ball-lens coupled probe to obtain spatially resolved fluorescence spectra from normal and neoplastic oral sites in a clinical setting (37); the shallow channel of this probe collects fluorescence from approximately 300 microns beneath the probe surface, which corresponds primarily to the epithelium and the superficial stroma.

In order to guide the interpretation of spectra collected with such probes, this chapter presents a Monte Carlo based model to study the sensitivity of tissue fluorescence spectra collected with a depth-selective probe to variations in epithelial and stromal optical parameters associated with neoplastic transformation. An advantage of using Monte Carlo simulations rather than analytic models is the lack of simplifying assumptions which must be made regarding either the source-detector geometry or the tissue heterogeneity. Monte Carlo simulations have been used to evaluate the effect of scattering and absorption changes on light propagation in a two layer model of the cervix (64, 88) and in multilayered models of the colon (89) and bronchial tissue (90). As a clinically relevant example, I explore the application of this model to describe fluorescence spectra of oral tissue, using physiologically realistic input parameters and tissue geometries for normal oral tissue and for benign and precancerous oral lesions.

High-resolution fluorescence and confocal microscopy of viable oral tissue has elucidated the autofluorescence and scattering characteristics of the epithelial and stromal layers in normal, benign and dysplastic tissue (70, 91, 92). Results from these studies suggest that oral epithelium can be divided into three layers with different optical properties. The superficial oral epithelium is occupied by a highly scattering keratinized layer which varies in thickness depending on the specific anatomical oral site or the presence of hyperkeratosis. The main fluorophore of the superficial layer is thought to be keratin. Beneath this layer, the non-keratinized oral epithelium is less scattering and is

occupied by metabolically active intermediate and basal cells. Fluorescence from the non-keratinized epithelium is associated with the metabolic indicators NADH and FAD, which increase in dysplastic oral samples.

Since carcinogenesis involves biochemical signaling between the epithelium and the surrounding extracellular matrix (75), the optical properties of the superficial stroma are expected to be altered more by disease progression than those of the deeper stroma. Stromal fluorescence, caused by collagen and elastin crosslinks, is significantly reduced in dysplastic and inflammatory oral samples, especially in the stromal layer immediately beneath the dysplastic epithelium. Dysplastic progression in oral mucosa leads to a decreased volume fraction of collagen and decreased stromal scattering (76), which also may be more prominent in the superficial stroma. Angiogenesis, associated with neoplastic progression in oral mucosa, may also be more prevalent in superficial stromal areas. In particular, spectra collected with a depth sensitive fiber optic probe will likely depend strongly on both the magnitude and the spatial extent of neoplastic related changes in optical properties.

Here I introduce a Monte Carlo model to describe fluorescence spectra in oral mucosa with a multi-layered tissue geometry, allowing depth dependent variation in optical parameters in both the epithelium and the stroma. This model uses realistic fluorescence input parameters for each sublayer derived from measurements in viable normal and neoplastic oral tissue. This depth sensitive model is used to study the sensitivity of predicted spectra to changes in biologically relevant optical parameters associated with the development of precancer and cancer, and thus to begin to elucidate the key optical parameters responsible for observed differences in normal and neoplastic fluorescence spectra. Finally, model predictions are compared to clinical spectroscopy measurements of normal and neoplastic tissue.

4.2 METHODS

4.2.1 Clinical measurements of fluorescence spectra from oral mucosa

A point probe spectroscopic system was used to obtain depth-resolved fluorescence spectra at 350 nm excitation of normal and neoplastic oral lesions in IRB approved clinical studies carried out at the University of Texas M.D. Anderson Cancer Center (37). Lesions selected by the clinician and an anatomically similar contralateral normal appearing site were measured for each patient by placing the probe against the mucosal surface. To minimize artifact from exposure to room light the measurements were performed in a darkened room. Wavelength calibration, power calibration and standard measurements were performed for each set of clinical measurements. After spectroscopic measurements, biopsies were collected from the corresponding tissue site for histological examination, subject to prior patient consent and discretion of the clinician. Histologic results were reviewed by a collaborating pathologist.

4.2.2 Tissue geometry and model input parameters

Oral mucosa is modeled as a multilayered medium with homogenous distribution of absorbers, scatterers and fluorophores within each sublayer. As illustrated in Fig. 4.1A, the epithelium of normal oral mucosa can be divided into three layers with different fluorescence characteristics. The strongly scattering superficial epithelial layer includes cells that retain keratin and the main fluorophore in this layer is assumed to be keratin. Immediately beneath this is a layer of intermediate non-keratinized epithelial cells containing FAD as the dominant fluorophore. Beneath this is a layer of basal epithelial containing mitochondrial NADH as the dominant fluorophore. Similarly, the stroma can

be divided into two layers with different optical properties: the superficial stroma and deeper stroma. Previous research shows that the main stromal fluorophores are collagen and elastin crosslinks (41). The thickness of each sublayer was derived from confocal fluorescence images of a representative normal tongue tissue slice shown in Fig. 4.1. In our model, the total thickness of the epithelial layer is 280 μm ; the superficial layer and the intermediate epithelial layer are each 80 μm thick, whereas the basal epithelial layer occupies 120 μm . The superficial stroma (stromal region 1) occupies an area 125 μm below the basement membrane and deeper stroma (stromal region 2) is modeled as a semi-infinite medium.

In this model the fluorescence emission properties of a given sublayer are described by the fluorescence efficiency term $(\mu(\lambda_{\text{ex}}) \cdot \phi(\lambda_{\text{ex}}, \lambda_{\text{em}}))$ of the dominant fluorophore within that sublayer, where $\mu(\lambda_{\text{ex}})$ is the absorption coefficient and $\phi(\lambda_{\text{ex}}, \lambda_{\text{em}})$ is the quantum efficiency of the dominant fluorophore. The spectral shape of the quantum efficiency for each sublayer was estimated from emission spectra at 350 nm excitation of biological samples containing the predominant fluorophore. The spectrum of keratin was obtained by measuring the fluorescence of human nail (41), which is dominated by keratin. The emission spectrum of an optically dilute solution of FAD was used to represent the shape of the fluorescence efficiency of the intermediate epithelial cells. A suspension of SiHa cervical cancer cells (41) was used to describe the shape of the basal epithelium. Previously it was shown that the emission spectrum from collagen type 1 gel can be described as a linear combination of spectra from three main types of collagen crosslinks (41). The contribution from collagen crosslinks with emission peaks at 410 nm was found to be dominant, and was used here as input for the shape of the stromal fluorescence efficiency. The relative magnitude of the fluorescence efficiency term for each sublayer was determined from the confocal images of the representative

normal tongue tissue slice used here as a baseline example. The relative fluorescence efficiencies for each sublayer are summarized in Fig. 4.1B.

Baseline values for the absorption and scattering coefficients for each epithelial and stromal layer were obtained from previous studies of cervical, oral and bronchial tissue. The scattering coefficients of the superficial and basal epithelial layer were derived from reflectance confocal measurements of cervical epithelium (92). In particular, the scattering coefficient extracted from keratinized cervical epithelium is used to represent superficial oral scattering, while the scattering coefficient from basal cervical cells is used here for the basal epithelial layer. The scattering coefficient of the intermediate epithelial layer was derived from reflectance confocal images of normal oral epithelium (70). The stromal scattering coefficients for stromal layer 1 and 2 were assumed to be the same and were taken from a study on bronchial tissue (94). Note that the scattering coefficients were extrapolated to lower wavelengths using the inverse proportionality relationship of cellular scattering to wavelength (95). The absorption coefficient was assumed to be constant throughout the oral epithelium and was based on measurements from bronchial tissue (94). Stromal absorption is assumed to be caused by collagen and oxy- and deoxy-hemoglobin. The total hemoglobin absorption coefficient was calculated by the well known expression for blood absorption published by Jacques (96). The extinction coefficients for oxy- and deoxy-hemoglobin were taken from the same source and the oxygen saturation of hemoglobin was assumed to be 80%. The concentration of hemoglobin per liter of blood used in this study was 150 g/l (the normal value reported by Jacques) and the baseline volume fraction of blood in stromal layers 1 and 2 was set to be 0.16%. Stromal collagen absorption coefficients are based on measurements from bloodless skin samples (97). Figures 1 C and D summarize the

baseline absorption and scattering coefficients for the stromal and epithelial layers used in this study.

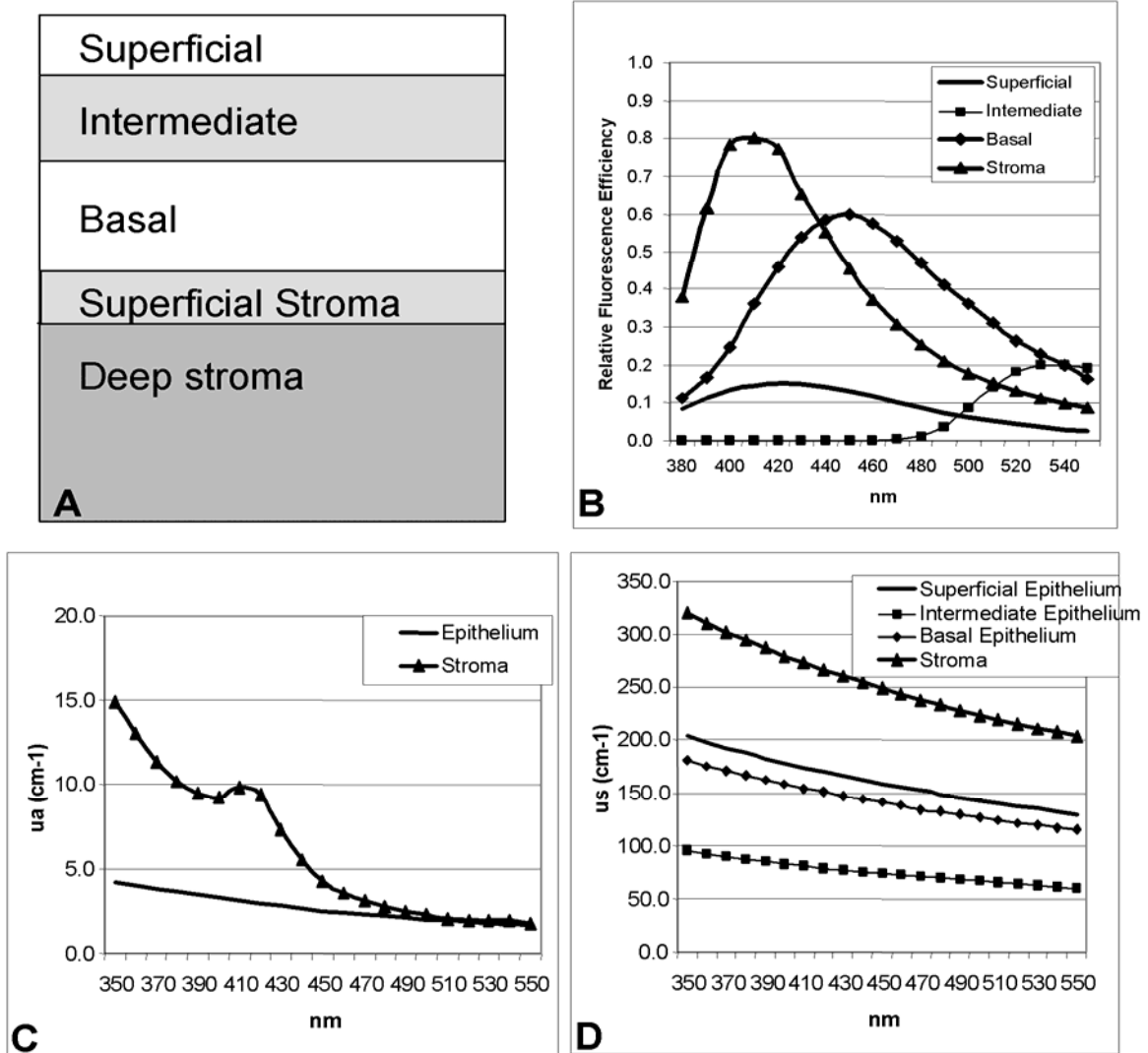


Figure 4.1: Baseline tissue geometry and input parameters: (A) Tissue geometry for normal oral tissue, (B) Normalized fluorescence efficiencies, (C) Absorption coefficients, (D) Scattering properties.

4.2.3 Description and validation of the Monte Carlo model

A fixed weight, multilayered reflectance Monte Carlo code with a depth selective fiber optic probe has been modified to account for generation and propagation of fluorescent light. Details regarding the reflectance Monte Carlo code and the geometry of illumination and collection are described in a previous study (93). In the fluorescence Monte Carlo code used here, excitation photons are initially propagated using scattering and absorption coefficient values at the excitation wavelength. At each scattering event, the probability of the photon being absorbed is given by $\mu_a / (\mu_a + \mu_s)$, where μ_a is the absorption coefficient and μ_s is the scattering coefficient for a specific layer. Upon absorption, the probability that a photon is absorbed by a fluorophore is calculated. In the epithelial layers this probability is equal to one, because it is assumed that the only absorbers are also fluorophores. In the stromal layers, however, a photon can be absorbed by either collagen crosslinks (a fluorophore) or by hemoglobin (an absorber). The probability that the photon is absorbed by a stromal fluorophore is given by $\mu_{a \text{ coll}} / (\mu_{a \text{ coll}} + \mu_{a \text{ Hb}})$, where $\mu_{a \text{ coll}}$ is the absorption coefficient of collagen and $\mu_{a \text{ Hb}}$ is the absorption coefficient for a given stromal layer at the excitation wavelength. The probability of fluorescence emission at a particular emission wavelength is given by the fluorescence efficiency of each sublayer. After isotropic emission, fluorescence photons are further propagated using the scattering and absorption coefficient of each layer at the emission wavelength, until reabsorbed or until remitted from the tissue surface. The Heyney-Greenstein approximation was used as the phase function. The accuracy of the multilayered fluorescence Monte Carlo code for an infinite source and detector was compared to remitted fluorescence reported in the literature and our results were found to be within 1% of published values (98).

Figure 4.2 shows a diagram of the depth selective probe used to measure tissue fluorescence spectra and the geometry used within the Monte Carlo code. In the probe, a ball lens is used to confine illumination and collection to a shallow area, approximately 300 microns beneath the tissue surface. In the Monte Carlo code, the ball lens was approximated using a half ball lens coupled to a flat window (93). To validate that the Monte Carlo code predicted the depth selectivity of the fiber probe, the code was used to predict the measured fluorescence from a thin fluorescent target as the distance between the probe tip and the target was varied. Results were compared to experimental measurements. The experimental measurements were performed in water to better simulate the refractive index mismatch between the probe tip and tissue. In the simulations, the fluorescence target was modeled as a very thin (10 μm) strongly fluorescent layer, with a large absorption coefficient and a very small scattering coefficient, and a refractive index equal to 1.4. The gap between the probe and the target was represented by a layer with the optical properties of water. Simulations of measurements at different probe to target distances were performed by increasing the thickness of the water layer in increments of 50-100 μm .

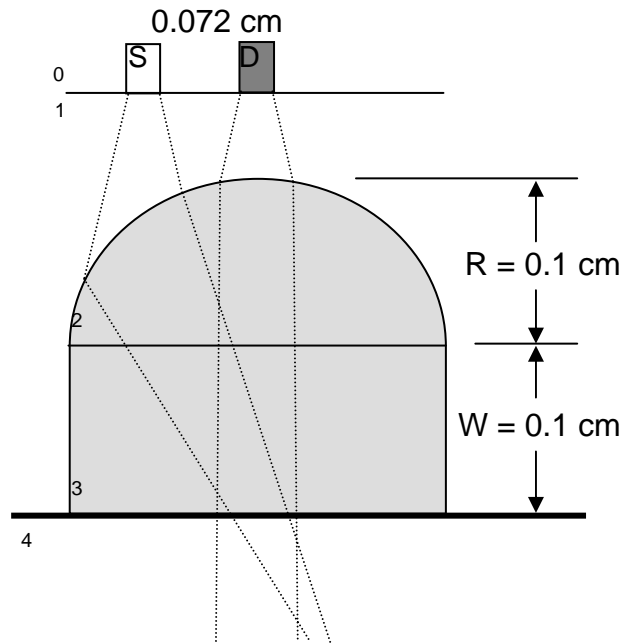


Figure 4.2: Diagram of the depth-selective fiber optic probe geometry used in the Monte Carlo forward model. S represents the source fiber, and D the detector fiber. An air gap separates the fibers and the half ball lens. The distance between the source and detector fibers is 0.072 cm. The window is placed in contact with tissue.

4.2.4 Predictions of Tissue Fluorescence

After validation, the Monte Carlo model was then used to explore the predicted fluorescence spectra of tissue. All simulations were done at an excitation wavelength of 350 nm. A single simulation output consists of the detected fluorescence intensity (total number of detected fluorescence photons) at emission wavelengths of 400 nm, 420 nm, 440 nm, 450 nm, 460 nm and 480 nm. Each simulation was performed with 10^8 excitation photons. Simulations were performed first for a baseline case using the optical properties of normal oral mucosa. Then a sensitivity analysis was performed by varying the optical properties of individual layers which are expected to change with neoplasia. In the baseline case and the model sensitivity analysis of stromal input parameters simulations were repeated three times. Simulations for the model sensitivity analysis of epithelial parameters were performed only once. For display purposes the output for the six emission wavelengths has been interpolated in Matlab using a linear interpolation function to decrease the sampling interval to 10 nm.

For each detected photon, the depth at which fluorescence emission occurred was recorded. The mean depth of fluorescence was calculated by averaging these depths for all detected photons. I calculated the depth above which 85% of the detected photons originated, termed the 85% fluorescence depth. I also calculated the fraction of detected photons with a depth of emission originating from the epithelium. Finally, in order to determine how deep excitation light penetrates, I recorded the maximum depth at which excitation photons scatter in tissue and calculated the depth at which 85% of the excitation light has been attenuated.

4.3 RESULTS

4.3.1 Validation of model with probe to target measurements

Figure 4.3 shows simulated fluorescence measurements for a thin fluorescent target as the distance between the probe tip and the sample is varied and compares the performance of the modeled probe to the actual probe used in the clinical studies. The agreement between measured and predicted data is within 10% at all distances and illustrates the depth selective nature of the probe which collects fluorescence generated within 300-400 microns of the probe tip.

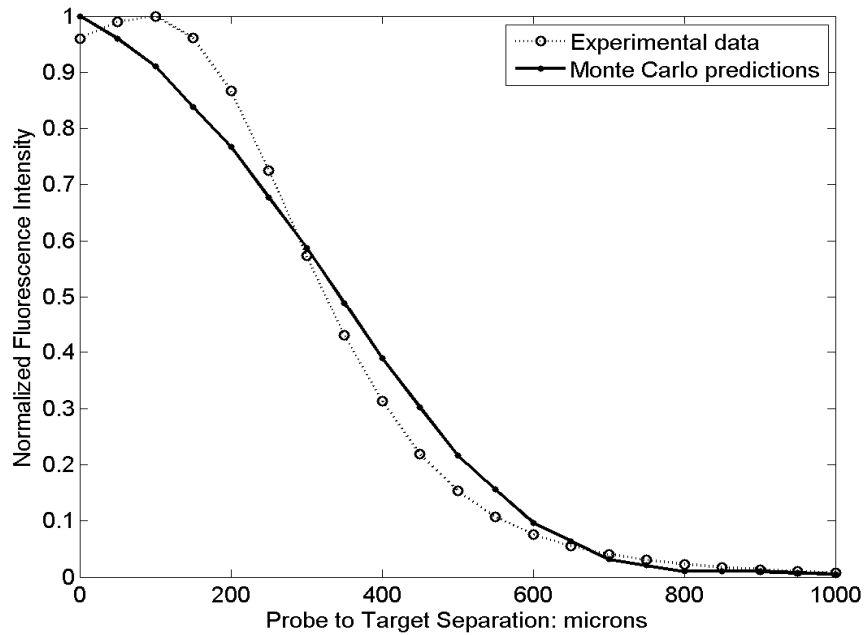


Figure 4.3: Detected fluorescence intensity from a thin fluorescent layer as the separation between the target and window is varied. The line represents Monte Carlo predictions and the symbols are experimental measurements.

4.3.2 Sensitivity of the model to variations in epithelial input parameters

The development of neoplasia in the oral cavity is accompanied by series of physiological changes in the epithelium such as hyperkeratosis and higher cellular metabolic activity. These physiologic changes lead to changes in optical properties, including increased epithelial scattering and an increase in the NADH associated fluorescence from epithelial cells. The effect of each of these changes on the detected fluorescence was studied individually by varying a particular input parameter while holding all other factors constant. Figure 3.4 summarizes the predicted fluorescence spectra for three different sets of simulations designed to model hyperplasia, hyperkeratosis and dysplasia in oral mucosa. Predictions in Figs. 3.4 A, C and E were normalized to the maximum intensity value of the baseline spectra (black line) to emphasize the effect of varying a particular input parameter on the overall intensity of the fluorescence. Predictions in Figs. 3.4 B, D and F were normalized by dividing each individual spectrum by its maximum intensity value to emphasize changes in spectral shape. In all sets of simulations, the baseline fluorescence spectrum is plotted as a black line. Table 4.1 summarizes the fraction of detected fluorescence photons which originate in the epithelium at 440 nm emission for each predicted spectrum.

The effect of hyperplasia is simulated by changing the thickness of the nonkeratinized epithelium (keeping the thickness of the superficial layer and the ratio of the intermediate epithelium to the basal epithelium thickness constant) in increments of 50 microns. Figures 3.4 A and B show that, as the thickness of the non-keratinized epithelium is increased, the overall fluorescence intensity drops, accompanied by a shift of the spectra to longer emission wavelengths and an increase in the fraction of detected photons generated in the epithelium. For example, increasing epithelial thickness by 150 microns results in a drop of fluorescence intensity at 440 nm emission by about a factor

of 1.5 and an increase in the fraction of epithelial photons by about a factor of 1.6. Examination of the number of epithelial and stromal photons indicates that the relative increase in the fraction of epithelial photons is due more to a drop in stromal photons than to an increased number of epithelial photons. Increasing the thickness of the nonkeratinized epithelium decreases excitation light penetration to stromal areas, and thus increases sampling of epithelial fluorescence. Decreased epithelial thickness results in the opposite trend. It is interesting to observe that even small changes (50 microns) in the thickness of non-keratinized epithelium have a significant effect on both the intensity and the shape of the predicted spectra.

The effect of hyperkeratosis on the spectral shape and fluorescence intensity was studied by changing the thickness of the strongly scattering, keratinized superficial layer (and hence changing the total thickness of the epithelium) by 50 microns; results are illustrated in Figs. 3.4 C and D. A thicker keratin layer results in a drop of fluorescence intensity by a factor of 1.3 without a significant shift in spectral shape and fraction of epithelial photons. However, a thicker keratin layer causes a small increase in photons detected from the keratin layer, and a large decrease in the numbers of photons from the underlying basal epithelial layer and stroma. Decreasing the thickness of the superficial layer has the opposite effect, due to deeper light penetration and increased detection of stromal fluorescence.

The development of dysplasia is associated with an increase in epithelial scattering and an increase in NADH based cellular fluorescence. I have modeled these changes by increasing the thickness of the basal epithelial layer without changing the overall thickness of the epithelium. As shown in Figs. 3.4 E and F, an 80 μm increase in the thickness of the basal epithelium leads to higher total fluorescence intensity and a shift of the spectral shape to the red. These changes are accompanied by a significant

increase (a factor of 1.4) in the fraction of detected epithelial photons, due an increase in the number of epithelial photons, but no significant change in the number of detected stromal photons. Thus, as the fraction of cells with higher scattering and NADH based fluorescence increases, fluorescence from the epithelium starts to dominate the total detected fluorescence.

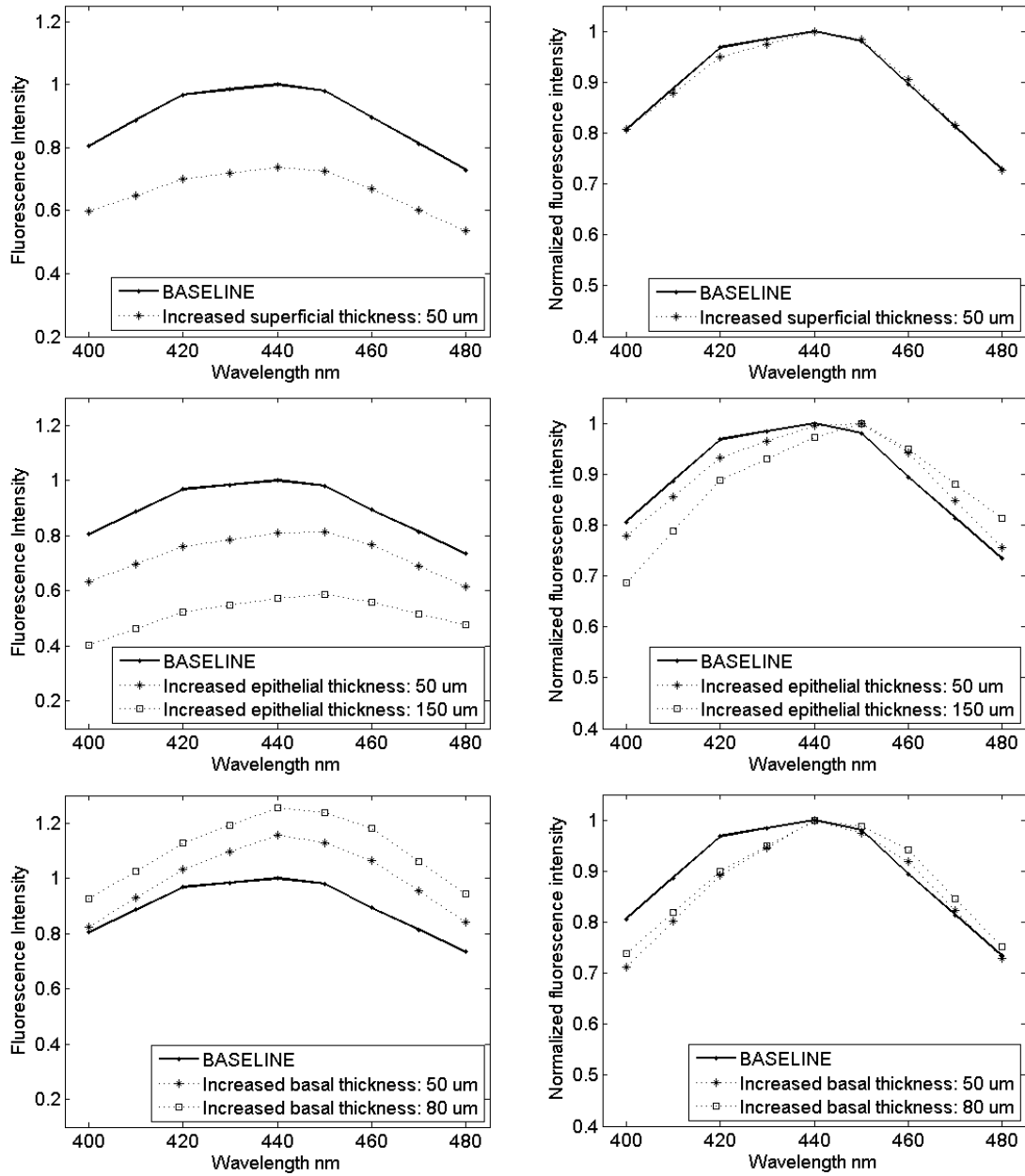


Figure 4.4: Effect of epithelial input parameters, associated with (A, B) hyperkeratosis, (C, D) hyperplasia and (E, F) dysplasia on the intensity (left column) and spectral shape (right column) of the predicted fluorescence spectra.

	Fraction of epithelial photons	Fraction of superficial photons
Baseline case	0.43 ± 0.01	0.90 ± 0.01
Thickness of nonkeratinized epithelium		
- 50 microns	0.35	0.88
+ 50 microns	0.51	0.92
+ 150 microns	0.66	0.93
Thickness of superficial epithelial layer		
- 50 microns	0.38	0.89
+ 50 microns	0.50	0.90
Thickness of the basal epithelial layer		
- 50 microns	0.35	0.88
+ 50 microns	0.56	0.92
+ 80 microns	0.60	0.93
Fluorescence Intensity of superficial stroma		
Increased by 20%	0.39	0.91
Decreased by 20%	0.50	0.89
Decreased by 40%	0.56	0.86

Table 4.1: Effect of input parameters associated with hyperkeratosis, hyperplasia and dysplasia on the fraction of photons detected from the epithelium and the fraction of photons detected from the superficial oral mucosa (the epithelium and stromal layer 1) at emission wavelength of 440 nm.

4.3.3 Sensitivity of the model to variations in stromal input parameters

The fraction of epithelial photons, calculated for different sets of simulations and summarized in Table 4.1, indicates that the modeled probe detects a substantial number of stromal photons. For example, in the baseline case, more the half of the detected photons originate from the stroma. In tissue geometries representing hyperplasia and dysplasia, the fraction of epithelial photons rises to 0.60 - 0.66, however complete rejection of stromal photons is not achieved, suggesting that variations in stromal parameters can also influence simulations. Here I have modeled stroma as a two layered medium which allows us to study variations in input parameters within each individual stromal sublayer.

Figure 4.5 illustrates the effect of changing the magnitude of the stromal fluorescence efficiency on the total intensity and spectral shape of the predictions. Benign and dysplastic alterations in oral tissue were found to be characterized by a large drop of fluorescence intensity in the superficial stroma (91). I simulated the effect of changes in the magnitude of the fluorescence efficiency of the superficial stromal layer 1 (Figs. 4.5 A and B), separately from changes in the deeper stromal layer 2 (Figs. 4.5 C and D). Decreasing the fluorescence efficiency of stromal layer 1 leads to a drop in the total fluorescence intensity and a shift of the spectrum to the red. These changes are also associated with an increased epithelial fraction of photons, due to a decrease in the number of stromal photons. Note that decreasing the fluorescence of stromal layer 1 by a factor of 2 leads to a significant decrease in total fluorescence (by a factor of 1.3) and a relatively large increase in the fraction of epithelial photons (by a factor 1.3). Previous research indicates that with inflammation and dysplasia, fluorescence from the stroma can drop by more then a factor of 3. Thus, changes in the magnitude of the fluorescence efficiency of stromal layer 1 can have a potentially more significant effect than shown in

Fig. 4.5. Decreasing the fluorescence efficiency of stromal layer 2 does not have a significant effect on the spectral shape, fluorescence intensity, or the fraction of detected epithelial photons. This indicates that only changes in the magnitude of the fluorescence efficiency of stromal layer 1 lead to changes in predicted spectra collected with the depth selective probe.

The effect of changes in stromal hemoglobin absorption on predictions is illustrated in Fig. 4.6. An increase in blood vessel density by about a factor of 1.2 to 3 is commonly associated with premalignant progression in oral mucosa (32). Here the volume fraction of hemoglobin in stroma was varied, which changes the stromal absorption coefficient. Simulations show that an increased volume fraction of hemoglobin in stromal layer 1 leads to a decrease in the total fluorescence intensity, mainly in the 400-440 nm emission region. These changes are also associated with small differences in the epithelial fraction of photons, also limited to the 400-450 nm emission range (data not shown). Changes in stromal layer 2 have a minimal effect on predicted spectra.

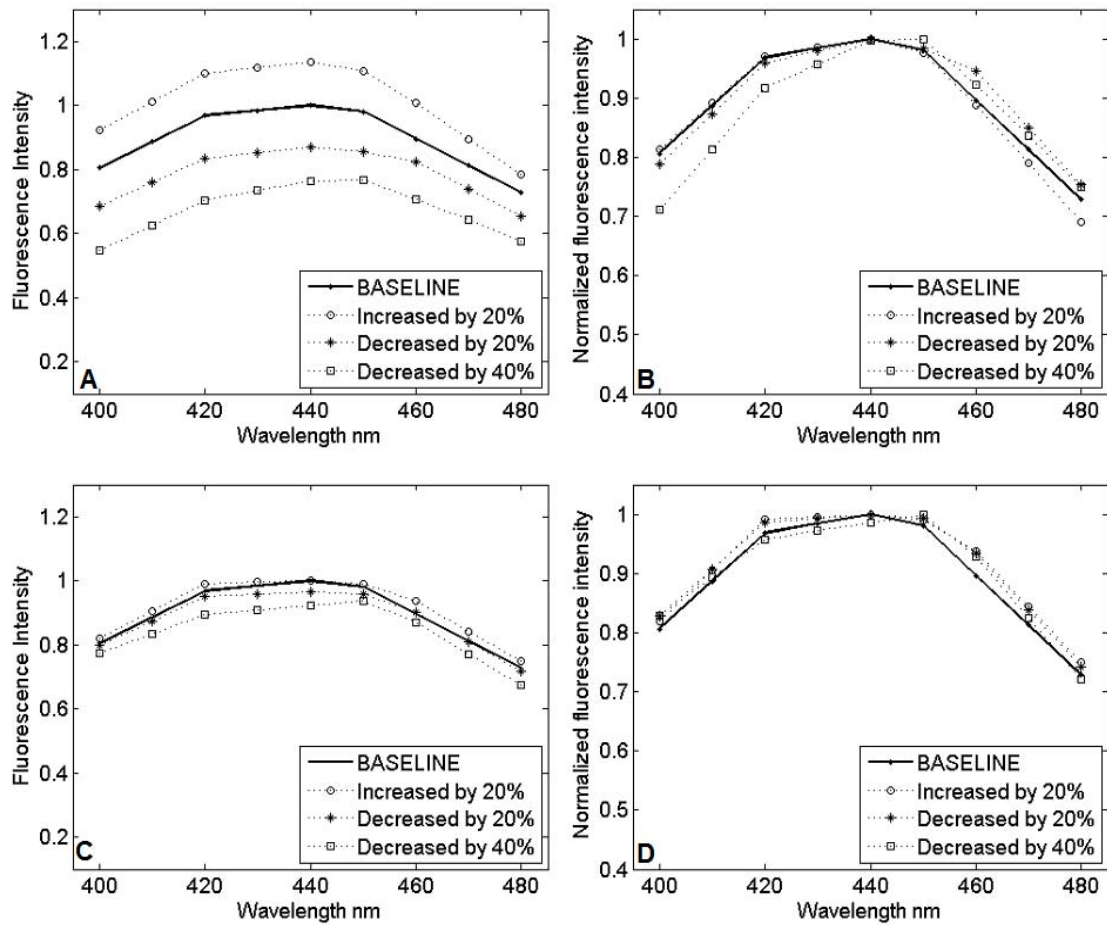


Figure 4.5: Effect of variations in the magnitude of the fluorescence efficiency of the stroma on (A and C) the intensity and (B and D) spectral shape of the predicted fluorescence spectra: (A-B): changes in superficial stromal layer 1 and (C-D): and deeper stromal layer 2.

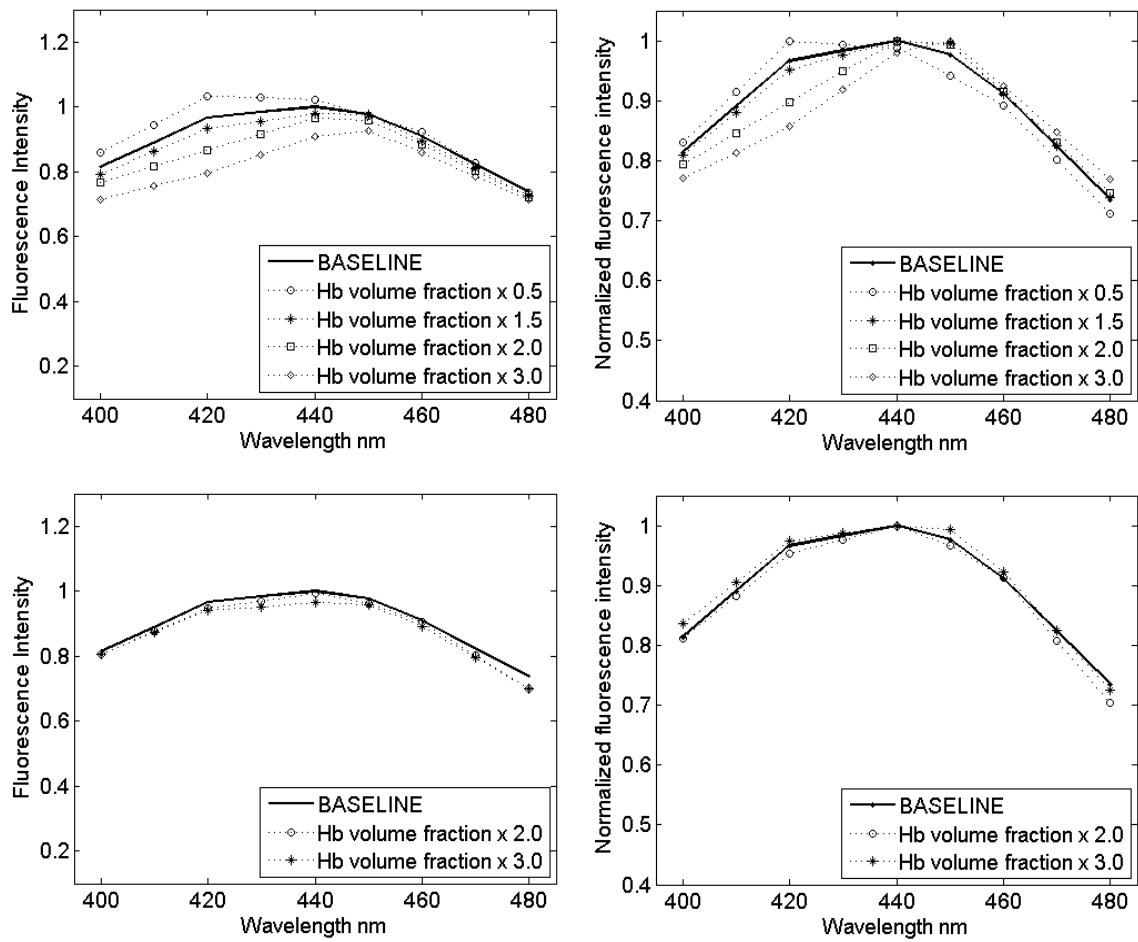


Figure 4.6: Effect of variations in the volume fraction of hemoglobin on (A and C) the intensity and (B and D) spectral shape of the predicted fluorescence spectra: (A-B) Changes in superficial stromal layer 1 and (C-D) deeper stromal layer 2.

Figure 4.7 summarizes the effect of decreasing scattering in stromal layer 1 and stromal layer 2. Results indicate that variations in the scattering coefficient in both stromal layer 1 and 2 do not change the spectral intensity, shape or epithelial photons fraction by more than 10%. It should be noted that varying both stromal scattering and hemoglobin absorption had a less pronounced effect on predictions compared to changes associated with variations in the stromal fluorescence and epithelial optical parameters.

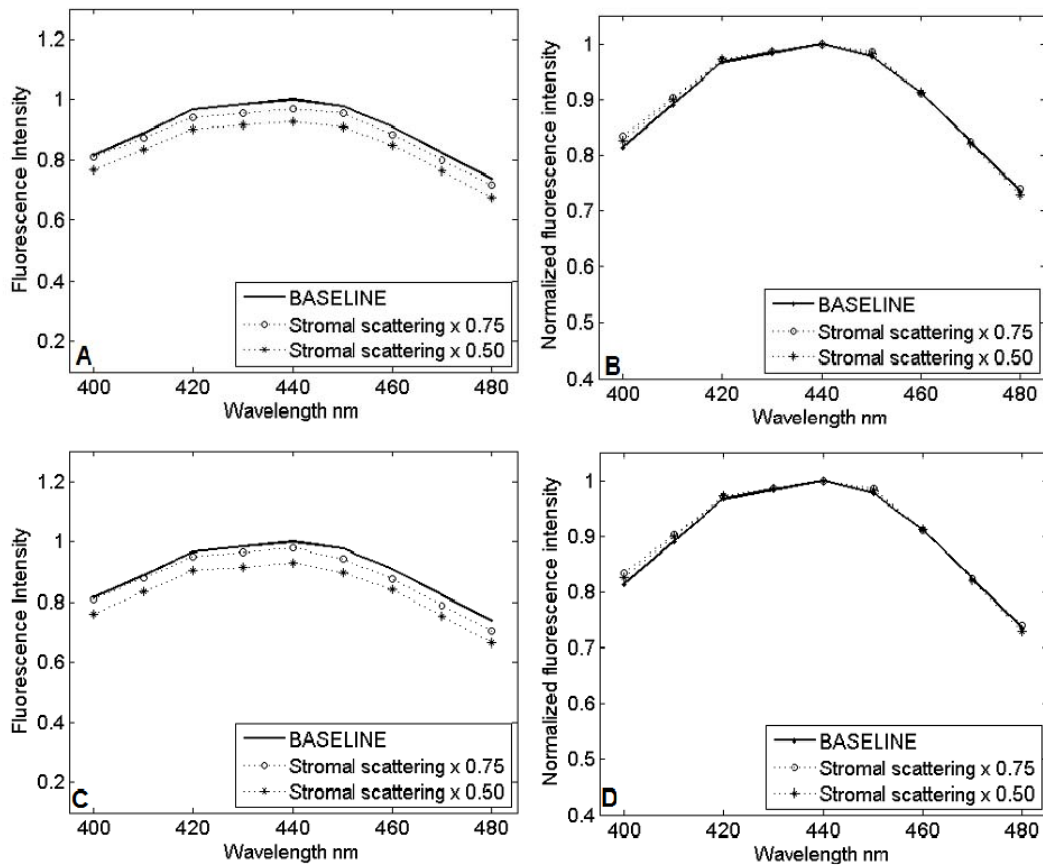


Figure 4.7: Effect of variations in the stromal scattering on (A and C) the intensity and (B and D) spectral shape of the predicted fluorescence spectra: (A-B) Changes in superficial stromal layer 1 and (C-D) deeper stromal layer 2.

4.3.4 Depth sensitivity analysis for fluorescence light

Results in Figs. 4.5-4.7 indicate that the fluorescence output is most affected by variations in input parameters from stromal layer 1. This suggests that the modeled probe geometry limits the penetration of excitation light to the superficial layers of the oral mucosa and detects fluorescence that originates mostly from the epithelium and superficial stromal areas. The fraction of superficial fluorescence photons (the number of fluorescence photons originating from the epithelial and superficial stromal layers divided by the total fluorescence photons) was calculated for the baseline case and for simulations with varied epithelial and stromal fluorescence parameters. As shown in Table 4.1, in the baseline case, 90% of detected fluorescence photons originate from the epithelium and superficial stromal layer 1. While variations in the input parameters influence the value of the superficial photon fraction, results consistently indicate that most (86 to 93%) of the detected fluorescence originates from the epithelium and superficial stroma of the oral mucosa for all sets of simulations.

Figure 4.8 shows the distribution of detected fluorescence photons as a function of the depth of generation for each photon for two tissue geometries. The mean fluorescence depth and the depth above which 85% of the photons originate are also indicated in Fig. 4.8. Note that these profiles display only the distribution of photons in the basal epithelium, the superficial stromal layer 1 and the deeper stroma. In the baseline case (Fig. 4.8 A) the mean fluorescence depth (278 μm) is approximately at the interface of the epithelium and stroma, while 85% the photons originate above the depth of 408 microns (approximately at the border of stromal layers 1 and 2). Figure 4.8 B displays the fluorescence depth profile for a tissue geometry representing hyperplasia. Increasing the thickness of the nonkeratinized epithelium by 150 μm , results in a photon distribution that is more shifted to the basal epithelial layer than in the baseline case. For

example, the mean fluorescence depth (328 μm) is above the epithelium/stromal interface, and the depth above which 85% of photons originate is located in the superficial stromal layer 1.

It should be noted that fluorescence emission can be caused by backscattered excitation light. Thus, while recording the origin at which fluorescence photons are generated is a useful indication of the enhanced detection abilities of the probe to superficial fluorescence, recording the maximum penetration depth of excitation light can further elucidate the significance of input parameters in stromal layer 2 on the depth resolved spectra. For the baseline case in Figure 4.8 A, the depth at which 85% of excitation light has been attenuated is 420 μm (located in the deeper stromal layer 2), while for the hyperplastic case this depth is just above the interface between the superficial stromal layer 1 and deeper stroma. Thus, for tissue geometries with a thinner epithelium, the optical properties of the deeper stroma can still have a small influence on the fluorescence output; fluorescence from tissue with thicker epithelium is largely independent of the optical properties of deep stroma.

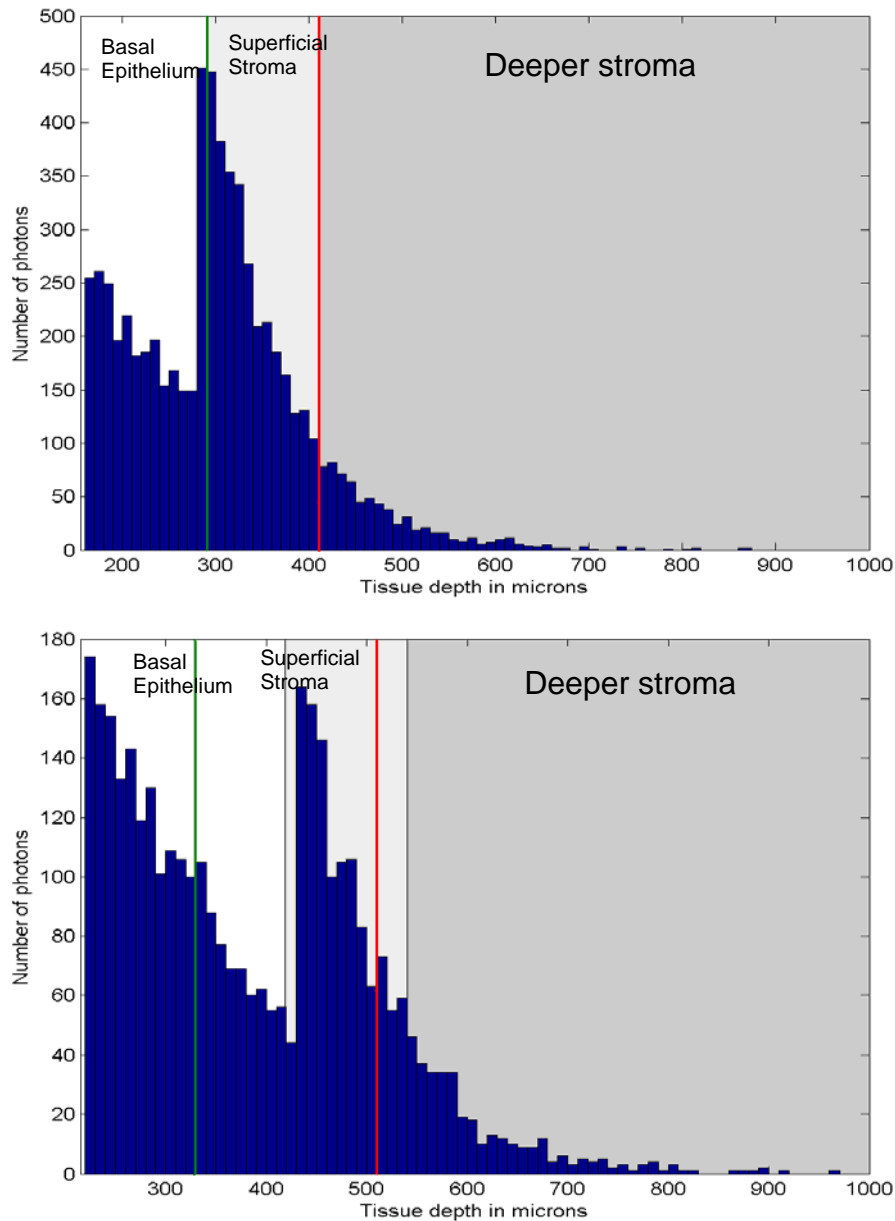


Figure 4.8: Depth profiles at emission wavelength of 440 nm for (A) the baseline case and (B) hyperplasia with increased non-keratinized epithelium of 150 μm . The profiles show the distribution of fluorescence photons in basal epithelium, superficial stroma and deeper stroma. The green line indicates the mean depth of fluorescence, whereas the red line marks the depth above which 85 % of fluorescence photons originate.

4.3.5 Comparison of Monte Carlo predictions to average clinical spectra

The performance of the Monte Carlo code in predicting normal and abnormal fluorescence spectra was validated by comparing simulation results to average spectra from normal and dysplastic sites measured from the buccal mucosa, the tongue, the lip, and the floor of the mouth at 350 nm excitation. Depth resolved fluorescence spectra from 336 normal oral sites and 19 oral sites diagnosed with moderate to severe dysplasia were used to calculate the average normal and dysplastic spectra.

Normal oral tissue was simulated with the input parameters and tissue geometry used in the baseline predictions. Dysplasia is characterized by a series of physiological changes including an increase in the total epithelial thickness (hyperplasia), thickening of the keratinized superficial epithelium, and spreading of abnormal cells with increased scattering and metabolic activity throughout the epithelium. In addition the fluorescence intensity of superficial stroma was found to decrease in oral lesions diagnosed with dysplasia. Other stromal changes, such as increased Hb absorption and decreased stromal scattering were not considered because the model sensitivity analysis shows that these parameters have only a small effect on the intensity and shape of predictions. In order to model dysplastic tissue the combined effect of several epithelial changes were considered. It was found that the set of changes that best predict dysplastic fluorescence spectra is a combination of hyperkeratosis, hyperplasia, increase in the thickness of the basal epithelium (to simulate the spreading of metabolically active and highly scattering cells) and a drop of fluorescence intensity of the superficial stroma. In particular, hyperkeratosis was modeled by a small increase in the superficial thickness (50 μm), a small increase in the thickness of the nonkeratinized epithelium (50 μm), and an increased fraction of the epithelium occupied by the basal sublayer. The fluorescence intensity of the superficial stromal was reduced by a factor of 1.6.

Figure 4.9 compares the average clinical spectra at 350 nm excitation to simulated spectra from normal and dysplastic sites. The error bars in the figure represent the standard deviation of the clinical average spectra at a particular emission wavelength (420 nm for normal and 440 nm for dysplasia) and indicate the degree of variability in the data sets. Results show good agreement between the clinical data and the simulations in both the normal and dysplastic case, except in 400-420 nm emission region. Moreover, both simulations sets are slightly shifted to the red emission region compared to clinical data. The Monte Carlo model accurately predicts the drop in intensity and the shift of spectral shape to longer emission wavelengths that accompanies dysplastic progression. Bar graphs representing the total number of detected photons from the epithelium and stroma are displayed in Fig. 4.9B. The drop in fluorescence intensity can be attributed to a decrease in the total number for photons originating from the stroma, whereas the shift of the emission peak is due to the increased fraction of epithelial photons of the total detected signal.

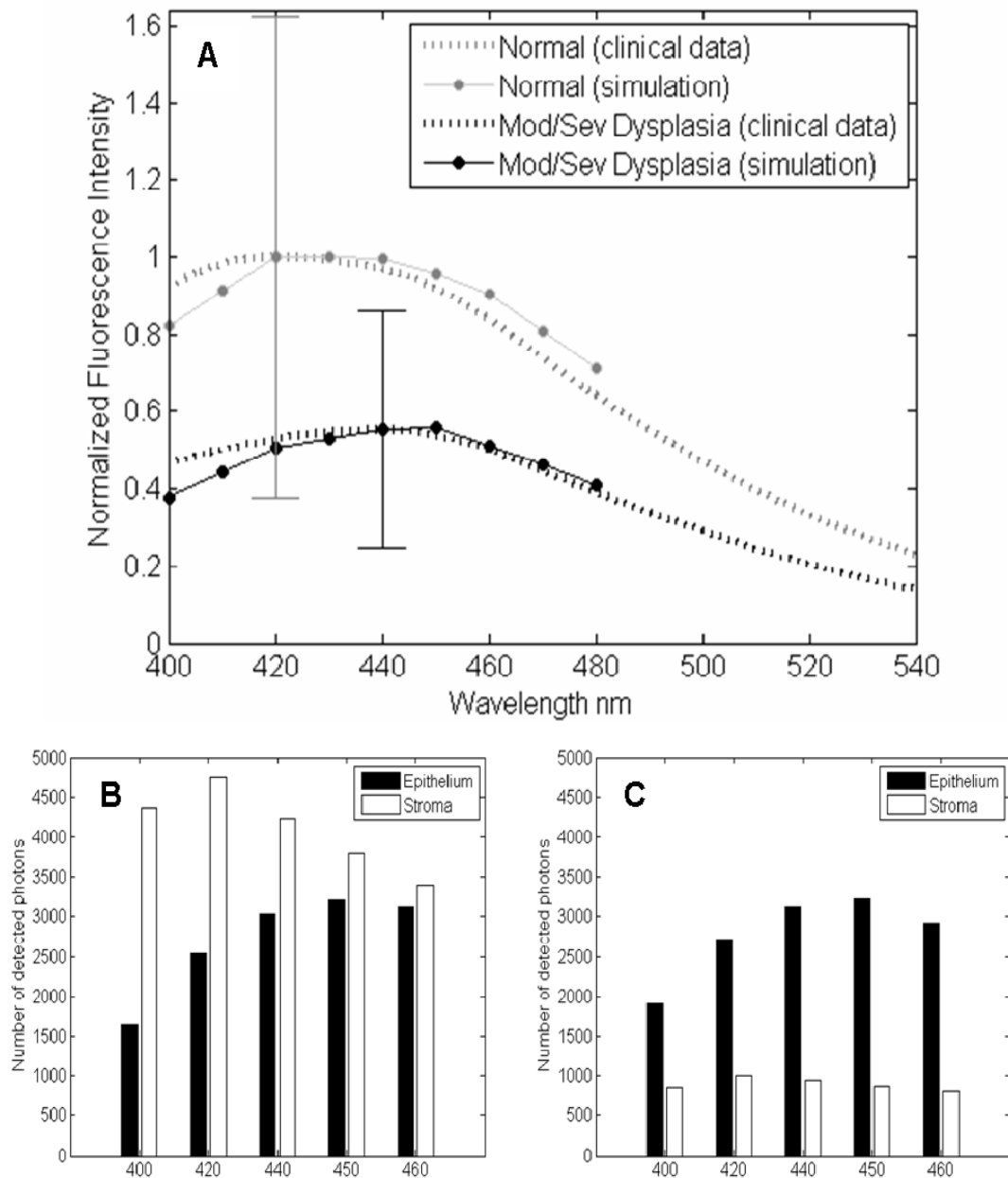


Figure 4.9: Comparison of average clinical fluorescence spectra from normal oral mucosa (blue line) and lesions diagnosed with moderate to severe dysplasia (red line) to Monte Carlo predictions. (A) Average clinical spectra and predictions. Error bars represent the standard deviation in the clinical data for each diagnostic category. Number of detected photons from the epithelium and stroma in (B) normal and (C) dysplastic predictions.

4.4 DISCUSSION

This chapter presents a Monte Carlo forward model to describe the sensitivity of oral tissue spectroscopy data collected with a depth selective fiber optic probe to changes in the optical properties of the epithelium and stroma that accompany the development of dysplasia. Simulation results show that the depth selective probe offers enhanced detection of fluorescence from the superficial layers of the oral mucosa. Comparison of simulated fluorescence spectra from normal and dysplastic oral tissue to clinical data shows that the model correctly predicts the characteristic drop in fluorescence intensity and the shift of spectral shape to longer emission wavelengths that accompanies neoplastic progression in the oral mucosa. Moreover, analysis of the depth of origin of the simulated fluorescence collected with the depth-selective probe indicates that the reduced fluorescence intensity associated with dysplasia is due to a decreased number of photons originating from the stroma, whereas the spectral red shift can be attributed to an increase in the fraction of epithelial photons in the total detected signal.

Similar trends in clinical data have been previously reported by other studies on oral cancer detection. For example, previously De Veld et al. have found that dysplastic and tumor sites are accompanied by a progressive drop in fluorescence intensity (26), whereas Lane et al reported a loss of autofluorescence signal in images of oral precancerous and cancerous lesions compared to the surrounding normal mucosa (32). Mathematical models for extracting the intrinsic fluorescence spectra from in vivo fluorescence spectra in the cervix (83) and the oral cavity (25) have been previously described. Results from these studies indicate that intrinsic fluorescence spectra can be composed of two spectral components, epithelial (NADH) and stromal (collagen), and that the epithelial contribution increases whereas the stromal contribution decreases with

malignant transformation. This is in agreement with current results from the depth analysis of simulated average fluorescence spectra of normal and dysplastic oral tissue.

The model sensitivity analysis described in this chapter elucidates the relationship between changes in tissue optical properties commonly associated with neoplastic development and the spectral characteristics of the depth resolved fluorescence spectra. It was found that predictions are sensitive to changes in the epithelial properties commonly associated with dysplastic progression in oral tissue. For example, thickening of the epithelial layer, thickening of the keratinized superficial epithelium and increasing the fraction of the epithelium occupied by more metabolically active and scattering cells all lead to significant changes in the shape and intensity of predicted spectra. As the epithelium becomes thicker and contains more metabolically active cells, the spectral intensity drops and the spectral shape shifts to longer emission wavelengths. These changes are accompanied by an increase in the fraction of epithelial photons in the total detected fluorescence. A major epithelial fluorophore is mitochondrial NADH. In this study the fluorescence properties of mitochondrial NADH were approximated by emission spectra from SiHa cells in suspension, which have an emission peak at 440 nm. In contrast, collagen crosslinks which are the dominant fluorophores in the stroma have an emission peak that is more shifted to the blue region (405 nm). Thus, the spectral shift in simulated spectra that is linked to neoplastic changes in oral mucosa suggests that the total detected signal is dominated by NADH-based fluorescence instead of stromal fluorescence.

Previous Monte Carlo based model sensitivity analysis of cervical reflectance and fluorescence spectra indicate that changes in epithelial parameters such as epithelial scattering and thickness have only a minimal effect on predictions (64, 88). It should be noted that these studies modeled fluorescence or reflectance detected with optical probes

that do not offer enhanced detection of epithelial signal. A recent investigation of the autofluorescence properties of viable oral tissue indicates that benign and premalignant lesions have similar stromal but different epithelial fluorescence properties (91). Thus, depth selective probes, which enhance the sensitivity to epithelial changes, may aid in accurate discrimination of spectra from benign and premalignant lesions.

In particular, results from the penetration depth analysis presented in this chapter show that 43-66% of total detected light with the depth-selective probe originates from the epithelium as the thickness of the nonkeratinized epithelium was varied from 280 to 420 microns. Previously a Monte Carlo model without enhanced detection of epithelial signal was employed to simulated fluorescence spectra of cervical tissue and to calculate the fraction of epithelial photons in the total detected fluorescence (55). Results from this study indicate that more than 80% of the fluorescence originates from the stroma when considering an epithelial thickness of 300 microns and optical properties similar to those used for the baseline case of normal oral mucosa. In comparison, the Monte Carlo model presented in the current study illustrates that the depth-selective probe offers a significant improvement in detecting light from the epithelial layer.

However, results from the depth sensitivity analysis also indicate that the modeled probe does not offer complete rejection of stromal fluorescence. This is in agreement with experimental measurements of the depth sensitive collection efficiency of the clinical probe which indicate that even though the probe's response is weighted towards the epithelium, it can not completely exclude stromal signal (37). Moreover, the simulations indicate that most of the stromal fluorescence originates from the superficial stromal region and not from deeper stroma. For example, the fraction of photons originating from the epithelium and superficial stromal region varies from 88 to 93% depending on the epithelial thickness. Changes in the optical properties of deeper stroma,

such as increased hemoglobin concentration and decreased stromal scattering and fluorescence intensity have minimal effect on predicted fluorescence spectra.

The enhanced detection of epithelial fluorescence offered by the depth selective probe depends on the overall thickness of the epithelial layer and also on the thickness of the superficial and basal epithelial sublayers. Therefore accurate predictions of depth enhanced spectra from the oral cavity depend on the use of biologically realistic tissue geometries. A major advantage of the Monte Carlo model described in this chapter is the use of tissue geometries obtained from confocal images of viable oral tissue. However the volume fraction of hemoglobin was estimated from previous studies on fluorescence spectra from cervical tissue. A more accurate estimation of the volume fraction of hemoglobin in the subepithelial stroma of oral tissue can lead to more accurate prediction of depth-resolved fluorescence spectra.

Chapter 5: The biological basis for differences in fluorescence spectra caused by neoplastic development and by anatomical site variations in oral mucosa.

5.1 INTRODUCTION

A Monte Carlo model that predicts depth-resolved fluorescence spectra from oral mucosa was introduced in Chapter 4. The model was tested by simulating a representative normal fluorescence spectrum and comparing predictions to average clinical data from normal sites. A typical dysplastic spectrum was simulated by changing optical parameters, commonly associated with neoplastic progression, and predictions were validated with average clinical data from dysplastic lesions. The model correctly predicts the characteristic drop in fluorescence intensity and the shift of spectral shape to longer emission wavelengths that accompany neoplastic progression in the oral mucosa.

However, model sensitivity analysis suggests that predictions are very sensitive to changes in epithelial and some superficial stromal input parameters. Even small (50 microns) changes in the epithelial thickness and the fluorescence intensity of superficial stroma can lead to noticeable differences in the shape and intensity of predictions. Visual analysis of confocal images from oral mucosa indicates that the thickness of the epithelium can vary by more than 40 microns even within the same field of view. The question arises as to whether the model can accurately predict a spectrum from an individual oral site by using input parameters derived from confocal images. In this chapter, I further validate the ability of the model to predict depth-resolved spectra from oral mucosa, by comparing predictions to measurements from a normal, a dysplastic and

a cancerous site obtained from the same patient. Input parameters for the thickness and fluorescence intensity of epithelial and stromal sublayers were extracted from confocal images of biopsies obtained from the same oral sites that were clinically measured.

Superficial epithelium in normal oral mucosa can vary significantly in thickness and fluorescence intensity depending on anatomical site (91). A thick superficial layer is expected in normal oral tissue from keratinized anatomical sites such as the hard palate and the gingiva, and also in some lesions such as leukoplakia (6, 99, 100). Muller et al. reported that in vivo fluorescence spectra from keratinized oral mucosa exhibit changes in the intensity and spectral shape compared to nonkeratinized tissue (25). De Veld et al. reported that autofluorescence spectroscopy cannot achieve accurate distinction between benign and malignant lesions, possibly due to the large spectral variance observed within the different pathologic categories (28). She points out that oral lesions differ in the degree of keratinization, in addition to other factors, such as hyperplasia and blood content.

Simulations in Chapter 4 indicate that even a small (50 microns) increase in the highly scattering superficial epithelial layer can decrease the intensity of the predictions. These simulations were performed by increasing the thickness of the superficial epithelium without changing the fluorescence intensity of this layer. In some confocal images analyzed in chapter 3, the superficial layer is also characterized by a very bright autofluorescence. This chapter investigates how the presence a strongly fluorescent superficial layer affects Monte Carlo predictions and suggests possible biological reasons for variations in clinical depth-resolved spectra measured from different anatomical sites. I simulated fluorescence spectra from a normal buccal site, having a thin and weakly fluorescent superficial layer, and a normal palate site, having a thick and very fluorescence superficial epithelium. Predictions were compared to clinical data and

analysis of the origin of simulated fluorescence signal was used to explain the differences in shape and intensity, observed in the clinical measurements from these two normal sites.

5.2 METHODS

5.2.1 Clinical measurements and biopsy collection

Depth-resolved fluorescence spectra at 350 nm excitation of a normal, dysplastic and cancerous oral site from the same patient were measured with a point probe spectroscopic device in a IRB approved clinical study carried out at the University of Texas M.D. Anderson Cancer Center. Depth-resolved spectra were also collected from normal buccal and normal palate sites from different patients. After spectroscopic measurements, the oral sites were biopsied and part of each biopsy was sent for histological examination by a certified pathologist. Transverse tissue slices were obtained from the second part of each biopsy and imaged with a confocal fluorescence microscopy while the tissue was still viable. Confocal images at UV excitation were obtained from each tissue slice. Detailed procedures for imaging and quantitative analysis of autofluorescence patterns are described in Chapter 3.

5.2.2 Tissue geometry and model input parameters

In order to validate the performance of the model in predicting neoplastic changes, fluorescence spectra from a normal, dysplastic and cancerous oral sites were simulated. Oral sites with layered morphology (the normal and the dysplastic example)

were modeled as a multilayered turbid media with five different sublayers: superficial, intermediate, basal epithelium, subepithelial and deep stroma. The thickness and relative fluorescence intensities for each sublayer were derived from confocal fluorescence images (at UV excitation) of the particular oral biopsy site considered in the simulations. Fluorescence efficiencies for each particular layer were derived as previously described in chapter 4. The cancer example was modeled as a turbid media with two main regions: a superficial region, occupied by cancer cells, and an underlying fibrous stroma. Based on visual examination of the confocal images, the superficial region was further subdivided into top, intermediate and lower sublayers, having different fluorescence intensities.

The buccal site was modeled as a multilayered turbid media with five different sublayers: superficial, intermediate, basal epithelium and subepithelial and deep stroma. Confocal images of the palate example indicate that here, the epithelium is covered by a very fluorescent keratinized layer, occupying the top 100 microns of the total epithelium, followed by another keratinized layer, having very weak fluorescence intensity. Underlying these keratinized layers, is the intermediate and basal epithelium and subepithelial and deep stroma.

Baseline scattering coefficients for each stromal and epithelial layer are described in chapter 4 (Figure 1 D) and are used as input values for the normal tongue, buccal and palate examples. Note that the two keratinized layers in the palate example are assumed to have the same scattering coefficient as baseline superficial epithelium. The superficial, intermediate and basal epithelium in the dysplastic example have the same scattering coefficients as the baseline case. However, to accurately model the drop in stromal scattering associated with oral dysplasias, the scattering coefficient in subepithelial stroma was decreased by a factor of 0.75 (76). The top 40 microns of the cancer example

were assumed to have the same scattering coefficient as baseline superficial epithelium; whereas cancer cells in the intermediate and lower cellular regions were assumed to have the same scattering coefficient as baseline basal epithelium. The scattering coefficient of fibrous stroma in the cancer example was decreased by a factor of 0.5, compared to the baseline stroma value.

The volume fraction of blood in the stroma for each particular example in this study was determined from quantitative analysis of H&E slides. In particular, H&E images for each particular diagnostic and anatomical site were taken and analyzed by estimating the fraction of the total stromal area occupied by blood. The estimated value includes areas occupied only by the lumen of the blood vessels and excludes lymph vessels. The volume fraction of blood in the superficial stromal layer of normal tongue was estimated to be in the range of 0.05 – 0.1%, while the value for deep stroma was in the range of 0.2-0.3%. The superficial stromal layer underlying dysplastic epithelium has a volume fraction of blood in the range of 0.11-0.20%, while deep stroma has an approximate value of 0.70 %. Previous research indicates that the microvessel density of oral cancers is about 3 times higher than in normal oral tissue (55). To model blood absorption in the cancer example, I increased the volume fraction of blood estimated from superficial normal stroma by a factor of 3.

5.3 RESULTS

5.3.1 Biological basis for spectral differences caused by neoplastic progression.

Clinical data indicate that neoplastic progression in oral cavity is characterized by a set of characteristic spectral differences. Some of these diagnostically relevant spectral features include a drop of fluorescence intensity and a shift of the spectral shape to longer emission wavelengths. Figure 5.1 displays clinical depth-resolved emission spectra at 350 nm excitation from a normal, a dysplastic and a cancerous tongue, measured from the same patient, and illustrates the characteristic drop in intensity and spectral shift to longer emission wavelengths associated with neoplastic progression in oral mucosa. Confocal images at UV excitation of oral biopsies taken from the same clinically measured oral sites are also displayed in Figure 5.1. The dysplastic example (Figure 5.1 B) displays a thicker basal epithelium and a lower fluorescence intensity from subepithelial stroma compared to normal tongue (Figure 5.1 A). Confocal images of the cancer example (Figure 5.1 C) illustrate the loss of layered architecture typical for cancer lesions.

Depth-resolved spectra for the normal, dysplastic, and cancerous tissue sites were simulated with the Monte Carlo based model. Biologically realistic input parameters for the tissue geometry and fluorescence properties of epithelial and stromal sublayers were determined from the confocal images for each specific pathologic case. Predictions and measured (in vivo) fluorescence spectra at 350 nm excitation are compared in Figure 5.2 A-C. In order to understand the depth-dependent origin of the predicted fluorescence, and how it changes with neoplastic progression, the numbers of photons originating from the epithelium and stroma have been calculated at each emission wavelength and summarized in Figures 5.2 D-F.

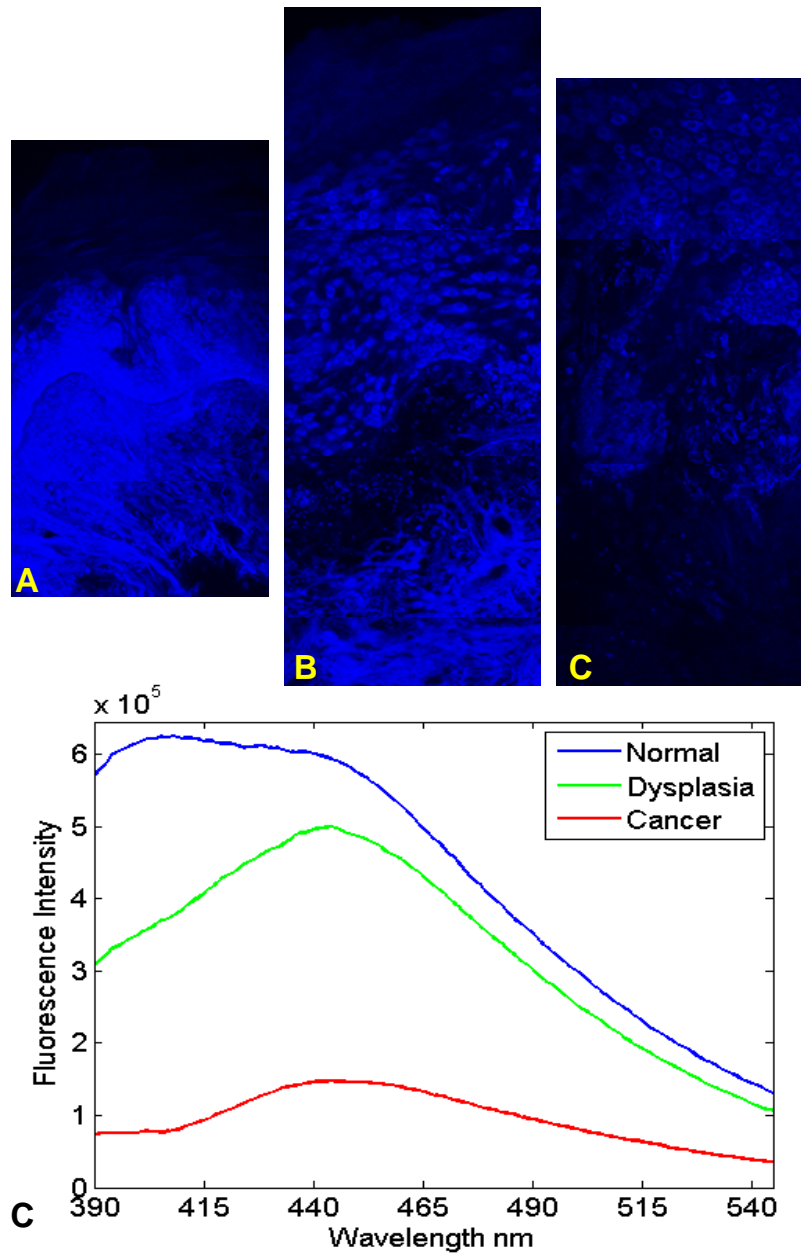


Figure 5.1: Fluorescence confocal images and clinical depth-resolved fluorescence spectra at UV excitation showing 3 stages of neoplastic progression in the tongue. The spectra are measured from the same oral sites shown in the confocal images. (A) Normal Tongue, (B) Focal Mild Dysplasia (with stromal inflammation), (C) moderately differentiated cancer, (D) Fluorescence spectra at 350 nm excitation of normal tongue (blue line), focal mild dysplasia (green line), and moderately differentiated cancer (red line).

Predictions show the characteristic drop in fluorescence intensity and spectral shift characteristic for dysplastic and cancerous oral lesions. The depth analysis indicates that in the normal case, the total detected fluorescence consists of a significant fraction of stromal photons. In the 400 – 440 nm emission range, stromal photons significantly dominate the predicted total fluorescence. With dysplasia (Figure 5.2 E), the number of photons originating from the stroma drops significantly, whereas the number of epithelial photons increases by about a factor of 2. Thus, the total predicted fluorescence is dominated by epithelial photons, which is reflected in a shift of the emission peak to longer emission wavelengths. The drop of total fluorescence intensity can be explained by the decreased number of photons detected from the stroma. The major optical parameters responsible for these changes are the increased thickness of basal epithelium and the decreased fluorescence intensity of the subepithelial stroma. Results from chapter 4 indicate that other stromal parameters, such as increased hemoglobin absorption and decreased stromal scattering, would not affect predictions as much as the changes in the fluorescence intensity of subepithelial stroma.

The superficial 400 microns of the malignant tissue slices are occupied by highly scattering cancer cells, followed by a fibrous matrix infiltrated, having atypical and inflammatory cells. It should be noted that the fluorescence intensity of the cancer cells, calculated from the confocal images of the cancer case, was lower than the fluorescence intensity calculated for basal cells from the normal and dysplastic example. The stromal matrix has lower fluorescence intensity, a lower scattering coefficient and higher blood absorption compared to normal and dysplastic stroma. Thus, the number of photons detected from the cancerous cell layer and the number of photons detected from the underlying fibrous matrix were low compared to the normal case. This resulted in an overall drop of fluorescence intensity, that is larger than the drop observed for the

dysplastic case. The prominent shift of the spectra to the red emission region is attributed to a dominant contribution from the cancerous cell region and a very small contribution from the fibrous matrix, especially in the 400 -440 nm emission region due to high blood absorption and low fluorescence intensity.

5.3.2 Biological basis for spectral differences caused by anatomical site variations.

Figure 5.3 shows autofluorescence trends of normal oral mucosa taken from different anatomical sites. As seen on Figure 5.3 A, normal buccal displays very similar autofluorescence patterns as does normal tongue (Figure 5.1 A). In contrast, the palate (Figure 5.3 C) has a very strongly fluorescent superficial layer and a basal layer that is thinner compared to normal tongue and normal buccal. Clinical depth-resolved fluorescence spectra at 350 nm excitation from normal buccal and palate are displayed in Figure 5.3 D. Here, the emission spectrum from the palate stands out by having an increased intensity and a spectral shape shifted to the blue region relative to the buccal.

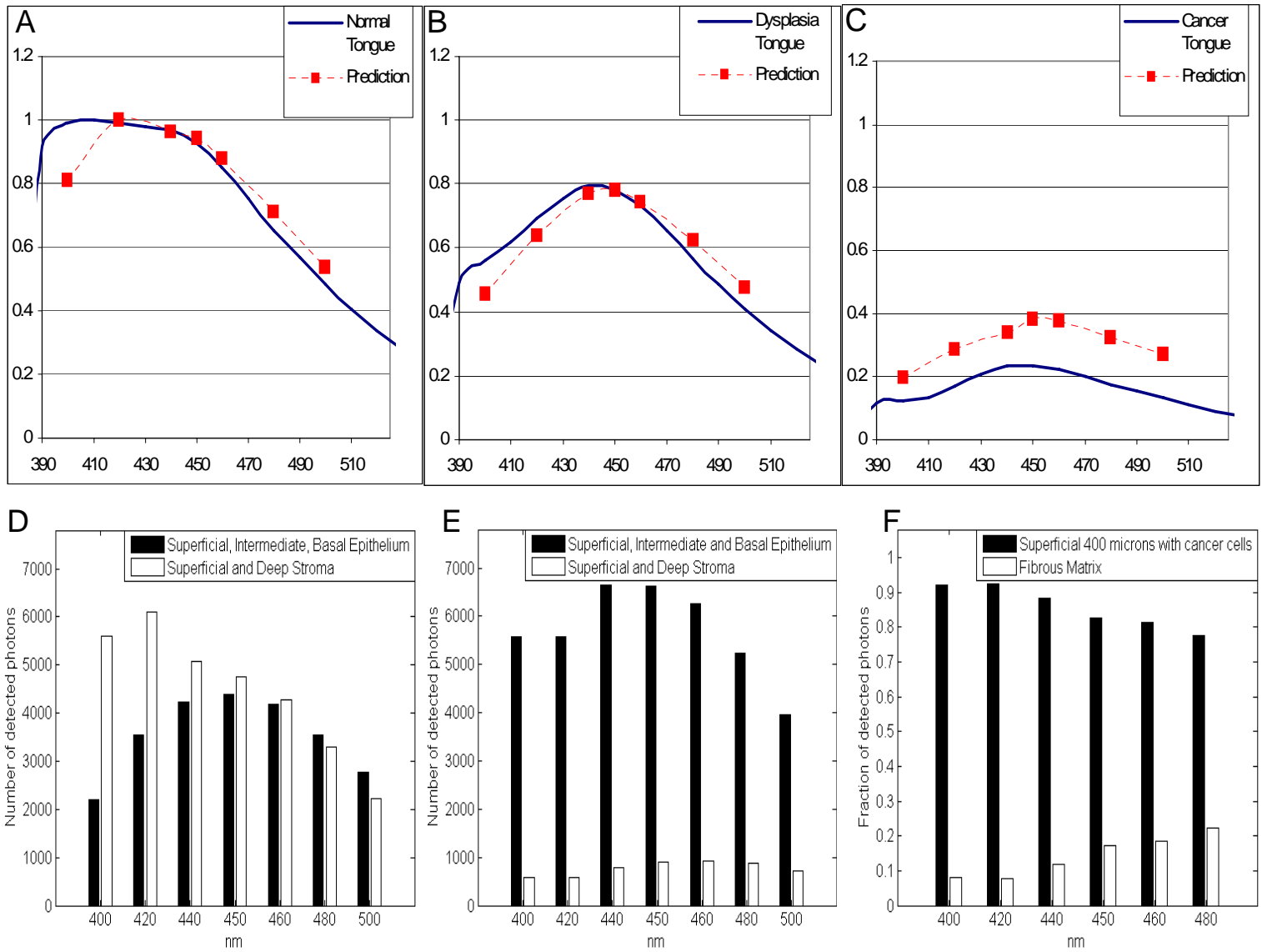


Figure 5.2: Validation of the Monte Carlo model with clinical fluorescence spectra of (A) a normal tongue site, (B) focal mild dysplasia, and (C) moderately differentiated cancer measured from the same patient. The x axis represents emission wavelength in nm, while the y axis represents normalized fluorescence intensity. The bar graphs represent the predicted number of photons originating from the epithelium (black bars) and the stroma (white bars) for (D) normal and (E) dysplastic oral tissue. The depth statistics for the cancerous example are displayed in (F) where the black bars represent detected photons from a superficial region (top 400 microns) with cancer cells and the white bars represent photons detected from the underlying fibrous matrix.

Predictions for each normal tissue site are compared to clinical measurements in Figure 5.4 A and B. The number of fluorescence photons from each epithelial sublayer and the number of photons originating from the stroma are summarized in Figure 5.4 D and C. Both the buccal and the tongue examples display a similar distribution of epithelial and stromal photons, with stromal fluorescence dominating the spectrum. In contrast, the palate example has an increased number of photons detected from the superficial epithelial layer, and an almost negligible number from the stroma. In addition, there is an increase in the photons detected from the basal epithelium, compared to the buccal and palate. Thus, the presence of a thick, highly scattering and fluorescent superficial layer shifts the origin of detected fluorescence towards the epithelial region and increases the overall fluorescence intensity. Since photons from the superficial layer dominate the spectra, the spectral shape of the detected fluorescence is similar to that of keratin (the dominant fluorophore in the superficial layer). Note that the fluorescence intensity of the predicted spectra from the palate is lower by about 15 % compared to the clinical measurements. Previous model sensitivity analysis has shown that even variations of 50 microns in the thickness of the superficial layer can result in a noticeable (a factor of 1.3) effect on the total intensity of the predictions. The estimated thickness of the strongly fluorescent keratin layer from the confocal images has a large standard deviation, which could explain the difference in intensity between the simulated and clinical spectra.

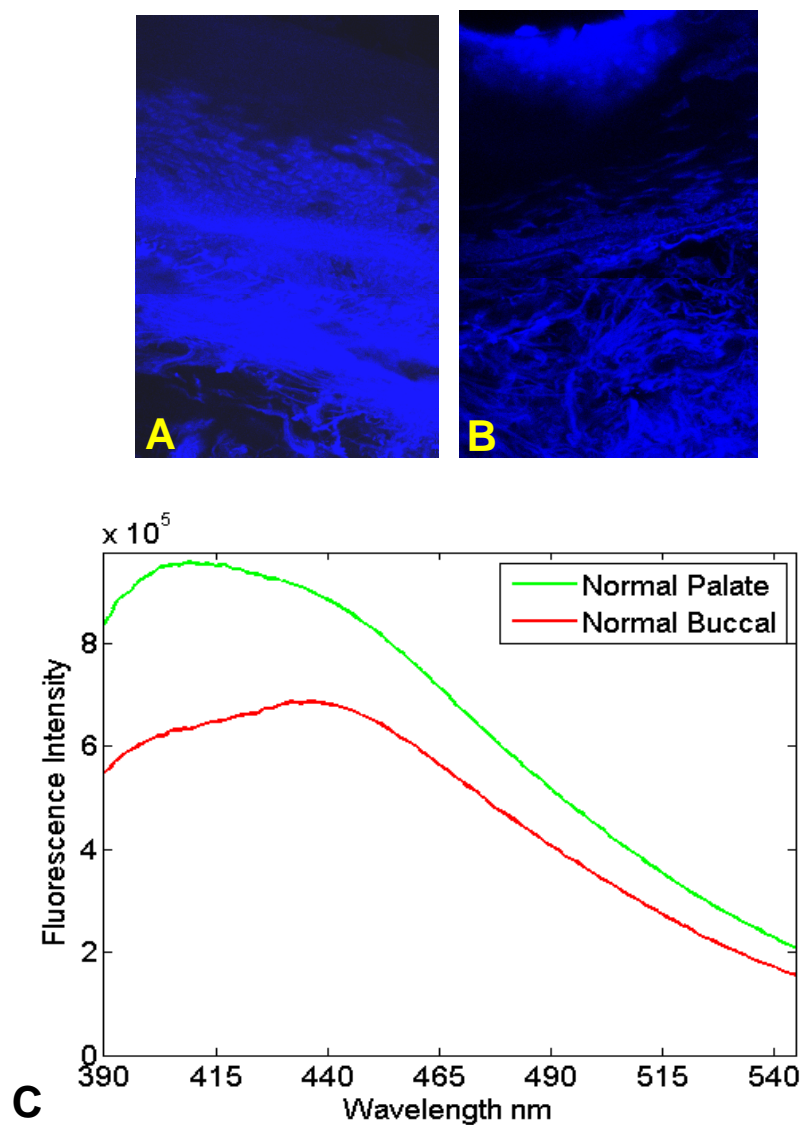


Figure 5.3: Fluorescence confocal images and depth-resolved clinical fluorescence spectra at UV excitation showing changes in autofluorescence patterns due to anatomical site variation. The spectra were measured from the same oral sites shown in the confocal images. Confocal images from (A) normal buccal and (B) normal palate. (C) Emission spectra at 350 nm excitation of normal buccal (red line) and normal palate (green line).

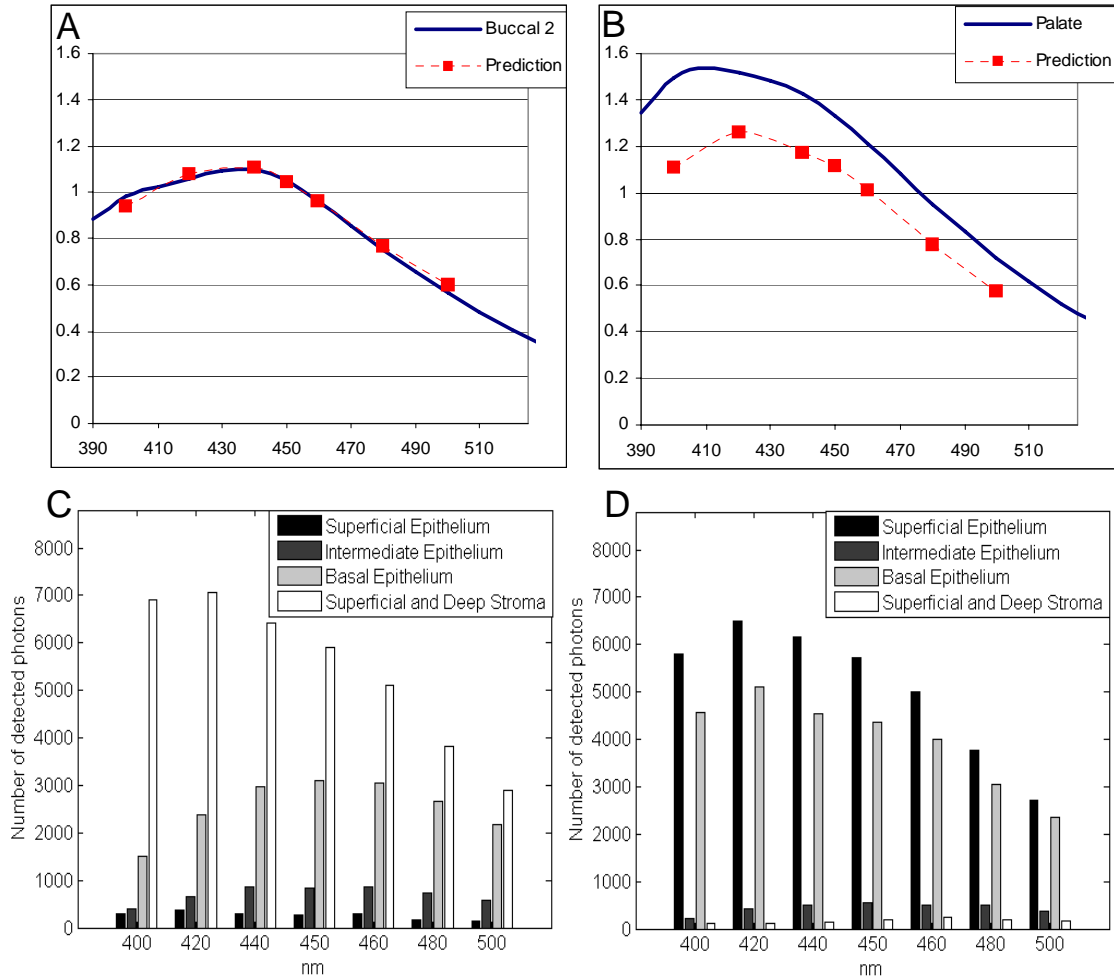


Figure 5.4: Validation of the Monte Carlo model with clinical spectra of oral sites from (A) normal buccal and (B) normal palate. The x axis represents emission wavelength in nm, while the y axis represents normalized fluorescence intensity. The bar graphs represent the predicted number of photons originating from the superficial (first bars); intermediate (second bars) and basal (third bars) epithelium and the stroma (forth bars) for (C) normal buccal and (D) normal palate.

5.4 DISCUSSION

This study tests the ability of the Monte Carlo model to predict depth-resolved spectra from individual spectra of a normal, dysplastic and a cancerous site by using tissue input parameters extracted from confocal images. The decreased fluorescence intensity and spectral shift to longer emission regions, typical for neoplastic progression in oral tissue, can be explained by a drop in the detected fluorescence from the superficial stromal layer and by an increase in fluorescence, originating from basal epithelium. The major optical parameters responsible for these changes are the decreased fluorescence intensity of the subepithelial stroma and the increased thickness of the basal epithelium.

For oral tissue with layered morphology, such as the normal and dysplastic example, the predictions agree very well with clinical data. Using input parameters for the thickness and fluorescence intensity for each sublayer derived from the quantitative analysis of confocal images can improve the accuracy of Monte Carlo simulations. In the cancer example, the intensity of the predicted spectrum was about 15 % higher than clinical data. This error can be attributed to the large variations in tissue morphology that can be observed even within the same field of view captured in the confocal images of the cancerous example. For tumor sites that display a loss of layered morphology, extracting optical properties for a single field of view can lead to noticeable errors in the predictions.

Results in this chapter, suggest that variations in the fluorescence intensity and thickness of the superficial layer in oral tissue can lead to significant differences in both the intensity and spectral shape of clinically measured data. The presence of a thick, highly scattering and fluorescent keratin layer shifts the origin of detected fluorescence towards the superficial and basal epithelium and increases the overall fluorescence

intensity of predicted spectra. In contrast, a previous clinical study reports that in vivo fluorescence spectra from keratinized oral mucosa exhibit a lower intensity compared to nonkeratinized tissue (25). These differences were explained by a reduction of the depth of penetration of excitation light due to scattering from the keratin layer, which results in an increased NADH and decreased collagen contribution to the measured spectra. Moreover, simulation results demonstrated in Chapter 4 also indicate that a thicker superficial epithelium leads to a decreased fluorescence intensity of predicted spectra. However, these simulations were performed by changing the thickness and not the fluorescence intensity of the superficial layer. Current predictions suggest that increasing the fluorescence intensity of the superficial layer leads to an increased fluorescence from the keratinized layer, in addition to a drop in stromal fluorescence. Thus, the total fluorescence is dominated by contributions from keratin, the main fluorophore in the superficial layer, and high fluorescence intensities from this layer would lead to an increase in the overall detected fluorescence. In the high-resolution microscopy study of oral tissue (Chapter 3), the presence of a very brightly fluorescence superficial layer was observed only in a limited number of samples. The fluorescence and morphological properties of the superficial layer in keratinized normal oral sites, such as the hard palate and gingiva, have to be determined in a larger data set.

Chapter 6: Conclusion

6.1 SUMMARY AND CONTRIBUTIONS

Autofluorescence spectroscopy and imaging have the potential to improve the early detections of oral cancer. Biochemical and structural changes associated with dysplastic progression alter the optical properties of oral mucosa and cause diagnostically significant differences in spectra from normal and neoplastic sites. This dissertation describes experimental and modeling studies aimed at elucidating the autofluorescence trends that accompany neoplastic progression in oral tissue and at revealing how changes in biologically relevant optical properties influence fluorescence spectra. Analysis of fluorescence from multilayered tissue, such as the oral mucosa, is further complicated by the depth-dependent distribution of fluorophores, scatterers and absorbers. Fiber optics probes that enhance the detection of fluorescence from the diagnostically significant epithelial and superficial stromal regions are likely to improve the accuracy of in vivo spectroscopy in detecting oral lesions. The ultimate goal of this work is to prove a biological explanation for diagnostically significant differences observed in depth-resolved fluorescence spectra measured from normal and neoplastic oral mucosa.

The first part of the dissertation presents an experimental approach to study the autofluorescence patterns in oral tissue. High-resolution confocal images have revealed the autofluorescence properties of oral mucosa are depth-dependent and that normal tissue can be subdivided into several epithelial and stromal layers. At UV excitation, most of the epithelial autofluorescence originates from the cytoplasm of cells occupying the basal and intermediate layers, while stromal signal originates from collagen and

elastin crosslinks. With dysplasia autofluorescence signal from basal and intermediate cells increases, while a dramatic drop in autofluorescence has been observed in stroma underlying neoplastic epithelium. Benign lesions diagnosed with severe inflammation, also display a dramatic drop in autofluorescence from subepithelial stroma, but have very different fluorescence patterns in the epithelium compared to dysplastic lesions. Imaging such lesions with optical devices or probes that measure mostly stromal fluorescence may result in similar findings of loss of fluorescence intensity and fail to distinguish benign inflammation from dysplasia. Another interesting finding is that UV excitation offers more optical contrast between normal, benign and dysplastic tissue, than excitation at longer wavelengths. Thus, results from this study suggest that the accuracy of fluorescence spectroscopy in differentiating benign inflammation from dysplasia could be improved by using excitation wavelengths in the UV range and fiber-optics probes with depth-sensitive detection of fluorescence signal.

A depth-sensitive probe that offers enhanced detection of epithelial signal has been previously designed in our lab and is currently used to detect fluorescence spectra from normal and neoplastic mucosa in clinical settings. In Chapter 4, I present a Monte Carlo model that predicts fluorescence spectra of the oral mucosa obtained with the depth-selective probe as a function of tissue optical properties. A model sensitivity analysis elucidates how variations in optical parameters associated with neoplastic development influence the intensity and shape of spectra. Predictions indicate that spectra of oral mucosa collected with the depth-selective probe are affected by variations in epithelial optical properties and to a lesser extent by changes in superficial stromal parameters, but not by changes in the optical properties of deeper stroma. Depth analysis of the predicted spectra reveals that 90% of the detected signal originates from the epithelium and superficial stroma. In addition, 43-66% of total detected light with the

depth-selective probe originates from the epithelium as the thickness of the nonkeratinized epithelium was varied from 280 to 420 microns. Thus, model sensitivity results confirm that the depth selective probe offers enhanced detection of epithelial fluorescence and that spectra detected with this probe are more sensitive to changes in epithelial optical parameters than the stromal parameters.

Model sensitivity results also suggest that predictions are influenced even by small changes in the epithelial thickness and the fluorescence intensity of superficial stroma. Therefore, accurate predictions of depth enhanced spectra from the oral cavity depend on the validity of input parameters used to model oral tissue. A major advantage of the Monte Carlo model is the use of biologically realistic tissue geometries and input parameters obtained from confocal images of viable oral tissue. In chapter 4 depth-selective spectra of normal and dysplastic oral tissue were simulated and were shown to be in good agreement with measured average spectra from normal and dysplastic oral sites. In chapter 5, I further validate the ability of the model to predict depth-resolved spectra from oral mucosa, by comparing predictions to measurements from a normal, a dysplastic and a cancerous site obtained from the same patient, using tissue input parameters extracted from confocal images.

Fluorescence spectra from normal and dysplastic oral tissue simulated in Chapter 4 and 5 correctly predict the drop in fluorescence intensity and the shift of spectral shape to longer emission wavelengths characteristic for neoplastic progression in the oral mucosa. The major changes in optical parameters that describe these spectral trends are the decreased fluorescence intensity of the subepithelial stroma and the increased thickness of the basal epithelium. It should be noted that increasing the thickness of the basal layer also increases the fraction of the total epithelium occupied by metabolically active and highly scattering basal cells. Analysis of the origin of simulated fluorescence

indicates that the reduced fluorescence intensity associated with dysplasia is due to a decreased number of photons originating from the stroma, whereas the spectral red shift can be attributed to an increase in the fraction of epithelial photons in the total detected signal. Thus, while fluorescence spectra collected with the depth-sensitive probe have an enhanced epithelial contribution and are very sensitive to changes in epithelial parameters, variations in the fluorescence properties of subepithelial stroma also have an effect on the total detected intensity.

Superficial epithelium in normal oral mucosa can vary significantly in thickness and fluorescence intensity depending on anatomical site. In the high-resolution microscopy study of oral tissue, the presence of a very brightly fluorescence superficial layer was observed in some of the tissue slices originated from keratinized oral mucosa. Chapter 5 suggests possible biological reasons for variations in clinical depth-resolved spectra measured from different anatomical sites. In particular it was found that the presence of a thick, highly scattering and fluorescent keratin layer shifts the origin of detected fluorescence towards the superficial and basal epithelium and increases the overall fluorescence intensity of predicted spectra. Further studies are needed to investigate the fluorescence properties of the superficial layer in keratinized normal oral sites, such as the hard palate and gingiva and to determine if depth-sensitive clinical spectra from these sites display spectral differences compared to nonkeratinized oral mucosa in a larger data set.

The depth-sensitive Monte Carlo model with biologically relevant input provides a simple and accurate method for predicting and analyzing clinical spectra from normal and neoplastic oral tissue. Some of the biological reasons for the decreased fluorescence intensity and spectral shift to the red region that are typical for neoplastic progression in oral tissue have been elucidated. In addition, possible sources for variations in clinical

data due to anatomical site to site differences have been address. Results outlined in this dissertation provide the first step towards building a model-based approach to analyze spectra data. However Monte Carlo simulations are time consuming, and real time diagnosis of oral cancer requires the development of an analytical model that can accurately describe depth-resolved fluorescence spectra from multilayered tissue.

6.2 FUTURE RESEARCH DIRECTIONS

A previous study showed that fluorescence spectra from cervical tissue, which is histologically similar to oral tissue, could be described by a two-layered analytical model. In the weakly scattering epithelial layer, light propagation can be described by the Beer-Lambert Law, assuming that the mean free path, $\delta = 1/(\mu_s + \mu_a)$, is comparable to the average epithelial thickness. In contrast, the stroma is the strongly scattering and light propagation in the stroma layer has been approximated by diffusion theory. The total remitted signal in this model includes four different cases of excitation and fluorescence light propagation through the two layers. In the first case excitation light is exponentially attenuated and converted to fluorescence in the epithelium. Here, the remitted light is further attenuated in the epithelium before it reaches the tissue surface. The second case refers to diffuse fluorescence that has been generated and scattered in the stroma and epithelium before reaching the tissue surface. The third case involves diffuse fluorescence light that has been generated in the epithelium but backscattered from the stromal/epithelium interface. The forth case refers to diffuse excitation light from the stroma that travels back to epithelium and causes epithelial fluorescence. For all four cases the fraction of fluorescence detected at the surface of the epithelium depends on the collection efficiency of the fiber optics probe.

The existing analytical model can be modified to account for light propagation in oral tissue and the depth-dependent response of the clinical probe used to measure fluorescence spectra from oral tissue. As a start, the Monte Carlo model described in Chapter 4 can be used to estimate which of the four major fluorescence cases, would be the dominant component in the depth-resolved signal detected from oral tissue. Preliminary Monte Carlo simulation results have shown that for normal oral mucosa, epithelial fluorescence (case 1) and diffuse stromal fluorescence (case 2) would be the dominant components to the total detected signal. Backscattered epithelial fluorescence from the epithelial/stromal interface (case 3) and epithelial fluorescence caused by diffuse excitation light from the stroma (case 4) would account for less than 10% of the total detected signal and could be ignored for simplicity reasons. This suggests that a simplified version of the analytical model could include mathematical expression only for epithelial and diffuse stromal fluorescence.

The depth-sensitive collection efficiency of the clinical probe could be experimentally determined by measuring the signal from a fluorescence target at different probe to target distances. An example of a previously determined fluorescence measurements at different probe to target distances of a can be found in Chapter 4, Figure 3. It should be noted that these experiments were performed in water. However, the measured collection efficiency of the probe depends on the properties of the media between the fluorescent target and the fiber tip. To estimate more accurately the collection efficiency of the probe, the media between the fluorescent target and the fiber tip should have scattering and absorption properties similar to that of tissue.

In summary, the Monte Carlo simulation approach outlined in this dissertation can be extended to develop an analytical expression of light propagation in multilayered tissue. The new model can be used in the inverse estimation of biologically relevant

optical parameters for clinically measured data. A model-based approach for diagnosing oral lesions has the potential to improve the accuracy of fluorescence spectroscopy as a screening tool for the early detection of oral neoplasia.

References

1. D.M. Parkin, F. Bray, J. Ferlay, P. Pisani. Global cancer statistics, 2002. *CA Cancer J. Clin*, 2005, 55:74-108.
2. American Cancer Society, *Cancer Facts and Figures 2006*. Atlanta, American Cancer Society, 2006.
3. J.J. Sciubba. Oral cancer: The importance of early diagnosis and treatment. *American Journal of Clinical Dermatology*, 2001, 2: 239-251.
4. S.R. Moore, N.W. Johnson, A.M. Pierce, D.F. Wilson. The epidemiology of mouth cancer: a review of global incidence. *Oral Diseases*, 2000, 6: 65-74.
5. A. Barasch, M. Safford, and E. Eisenberg. Oral cancer and oral effects of anticancer therapy. *Mount Sinai journal of medicine*, New York, 1998, 65: 370-7.
6. S. Silverman. *Oral Cancer*. 1998, Hamilton, ON: American Cancer Society.
7. H.S. Goodman, J.A. Yellowitz, A.M. Horowitz. Oral cancer prevention. The role of family practitioners. *Archives of Family Medicine*, 1995, 4: 628-636
8. [http:// www.adam.com](http://www.adam.com).2006
9. F.H. Martini. *Fundamentals of Anatomy & Physiology*. Fifth ed. 2001, Upper Saddle River, N.J.: Prentice Hall.
10. C.A. Squier, M.J. Kremer. Biology of the Oral Mucosa and Esophagus. *Journal of the National Cancer Insitute Monographs*, 2001, 29: 7-15.
11. L.E. Bouquot, P.M. Speight, P.M. Farthing. Epithelial dysplasia of the oral mucosa: Diagnostic problems and prognostic features. *Current Diagnostic Pathology*, 2006, 12: 11-21.
12. S. Silverman, R.D. Rosen, Observation on the clinical characteristics and natural history of oral leukoplakia. *Journal of the American Dental Association*, 1968, 76: 772-777.
13. J.J. Sciubba. Oral Leukoplakia. *Crit Rev Oral Biol Med*, 1995. 6: 147-160.
14. C. Scully, S. Porter. ABC of oral health: Swellings and red, white, and pigmented lesions. *British Medical Journal*, 2000, 321: 225-228.

15. N. Ramanujam, M. Follen Mitchell, A. Mahadevan-Jansen, S. L. Thomsen, G. Staerckel, A. Malpica, T. Wright, N. Atkinson, R. Richards-Kortum. Cervical pre-cancer detection using a multivariate statistical algorithm based on laser induced fluorescence spectra at multiple excitation wavelengths. *Photochem. Photobiol.* 1996, 6: 720-35.
16. R.J. Nordstrum, L. Burke, J.M. Niloff, J.M. Myrtle. Identification of Cervical Intraepithelial Neoplasia (CIN) Using UV-Excited Fluorescence and Diffuse-Reflectance Tissue Spectroscopy. *Lasers Surg. Med.* 2001, 29: 118-127.
17. S.K. Chang, M. Follen, A. Malpica, U. Utzinger, G. Staerckel, D. Cox, E.N. Atkinson, C. MacAulay, and R. Richards-Kortum. Optimal Excitation Wavelengths for Discrimination of Cervical Neoplasia. *IEEE Trans. Biomed. Eng.* 2002, 49: 1102-1111.
18. I. Georgakoudi, E.E. Sheets, M.G. Müller, V. Backman, C.P. Crum, K. Badizadegan, R.R. Dasari, M.S. Feld. Trimodal Spectroscopy for the Detection and Characterization of Cervical Precancers in vivo. *Am. J. Obstet. Gynecol.* 2002, 186: 374-382.
19. G.M. Palmer, C. Zhu, T.M. Breslin, F. Xu, K.W. Gilchrist, N. Ramanujam. Comparison of multi-excitation fluorescence and diffuse reflectance spectroscopy for the diagnosis of breast cancer, *IEEE Trans. Biomed. Eng.* 2003, 50: 1233-1242.
20. I. Georgakoudi, B. Jacobson, J. Van Dam, V. Backman, M. Wallace, M. Müller, Q. Zhang, K. Badizadegan, D. Sun, G. Thomas. Fluorescence, reflectance, and light-scattering spectroscopy for evaluating dysplasia in patients with Barrett's esophagus. *Gastroenterology*, 2001, 120: 1620-9.
21. F. Koenig, R. Larne, H. Enquist, F. J. McGovern, K. T. Schomacker, N. Kollias, T. F. Deutsch. Spectroscopic measurement of diffuse reflectance for enhanced detection of bladder carcinoma. *Urology*, 1998, 51, 342-345.
22. G. Zonios, L. T. Perelman, V. Backman, R. Manoharan, M. Fitzmaurice, J. Van Dam, M. S. Feld. Diffuse reflectance spectroscopy of human adenomatous colon polyps in vivo. *Applied Optics*, 1999, 38: 6628-6637.
23. A. Gillenwater, R. Jacob, R. Ganeshappa, B. Kemp, A. K. El-Naggar, J. L. Palmer, G. Clayman, M. Follen Mitchell, R. Richards-Kortum. Noninvasive diagnosis of oral neoplasia based on fluorescence spectroscopy and native tissue autofluorescence. *Arch Otolaryngol Head Neck Surg.* 1998, 124: 1251-8.

24. D.L. Heintzelman, U. Utzinger, H. Fuchs, A. Zuluaga, K. Gossage, A.M. Gillenwater, R. Jacob, B. Kemp, R. R. Richards-Kortum. Optimal excitation wavelengths for in vivo detection of oral neoplasia using fluorescence spectroscopy. *Photochem. Photobiol.* 2000, 72:103-13.
25. M.G. Muller, T.A. Valdez, I. Georgakoudi, V. Backman, C. Fuentes, S. Kabani, N. Laver, Z. Wang, C. W. Boone, R. R. Dasari, S. M. Shapshay, M. S. Feld. Spectroscopic detection and evaluation of morphologic and biochemical changes in early human oral carcinoma. *Cancer* 2003, 97:1681-92.
26. D.C. De Veld, M. Skurichina, M.J. Witjes, R.P. Duin, H. J. Sterenborg, J. L. Roodenburg. Autofluorescence and diffuse reflectance spectroscopy for oral oncology. *Lasers Surg Med.* 2005; 36:356-4.
27. C. Y. Wang, T. Tsai, H. M. Chen, C.T. Chen, C. P. Chiang. PLS-ANN based classification model for oral submucous fibrosis and oral carcinogenesis, *Lasers Surg Med.* 2003; 32:318-26.
28. D.C. De Veld, M. Skurichina, M.J. Witjes, R.P. Duin, H.J. Sterenborg, J.L.Roodenburg. Clinical study for classification of benign, dysplastic and malignant oral lesions using autofluorescence spectroscopy. *J Biomed Opt.* 2004; 9:940-50.
29. C.S. Betz , M. Mehlmann, K. Rick, H. Stepp, G. Grevers, R. Baumgartner, A. Leunig. Autofluorescence imaging and spectroscopy of normal and malignant mucosa in patients with head and neck cancer. *Lasers Surg Med* 1999; 25:323-34.
30. R. Paczona, S. Temam, F. Janot, P. Marandas, B. Luboinski. Autofluorescence videoendoscopy for photodiagnosis of head and neck squamous cell carcinoma. *Eur Arch Otorhinolaryngol* 2003; 260:544-8.
31. Kulapaditharom B, Boonkitticharoen V. Performance characteristics of fluorescence endoscope in detection of head and neck cancers. *Ann Otol Rhinol Laryngol* 2001; 110:45-52.
32. P. M. Lane, T. Gilhuly, P. D. Whitehead, H. Zeng, C. Poh, S. Ng, M. Williams, L. Zhang, M. Rosin, C.E. MacAulay. Simple device for the direct visualization of oral-cavity tissue fluorescence. *J Biomed Opt* 2006; 11:024006-1-7.
33. L. Nieman, A. Myakov, J. Aaron, K. Sokolov, Optical sectioning using a fiber probe with an angled illumination-collection geometry: evaluation in engineered tissue phantoms. *Appl. Opt.* 2004, 43, 1308-1319.

34. C. Zhu, Q. Liu, N. Ramanujam, Effect of fiber optic probe geometry on depth-resolved fluorescence measurements from epithelial tissues: a Monte Carlo simulation. *J. Biomed Opt.* 2003, 8, 237-247.
35. D. Arifler, R. A. Schwarz, S. K. Chang, and R. Richards-Kortum, "Reflectance spectroscopy for diagnosis of epithelial precancer: model-based analysis of fiber-optic probe designs to resolve spectral information from epithelium and stroma," *Appl. Opt.* 2005, 44, 4291-4305.
36. M.C. Skala, G.M. Palmer, C. Zhu, Q. Liu, K.M. Vrotsos, C.L. Marshak-Stone, A. Gendron-Fitzpatrick, and N. Ramanujam, "Investigation of fiber-optic probe designs for optical spectroscopic diagnosis of epithelial pre-cancers," *Lasers Surg. Med.* 2004, 34, 25-38.
37. R. Schwarz, W. Gao, D. Daye, R. Richards-Kortum, A. Gillenwater. Autofluorescence and diffuse reflectance spectroscopy of oral epithelial tissue using a depth-sensitive fiber-optic probe. *Applied Optics* (submitted)
38. L. Stryer. *Biochemistry*, 34d Edition, 1988, New York: WH Freeman
39. B.R. Masters, B. Chance. In *Fluorescent and Luminescent Probes for Biological Activity*, ed. WT Mason, London: Academic Press, 1993.
40. C. Brookner., M. Follen I. Boiko, J. Galvan, S. Thomsen, A. Malpica, S. Suzuki, R. Lotan, R. Richards-Kortum. Tissue Slices Autofluorescence Patterns in Fresh Cervical Tissue. *Photochem. Photobiol.* 2000, **71**, 730-36.
41. K. Sokolov, J. Galvan, A. Myakov, A. Lacy, R. Lotan, R. Richards-Kortum Realistic Three-Dimensional Epithelial Tissue Phantoms for Biomedical Optics. *J. of Biomed. Opt.* 2002, **7**, 148-156.
42. J.D. Pitts, R.D. Sloboda, K.H. Dragnev, E. Dmitrovsky and M. Mycek Autofluorescence characteristics of immortalized and carcinogen-transformed human bronchial epithelial cells. *J. of Biomed. Opt.* 2001, **6**, 31-40.
43. F. Smedts, F. Ramaekers , R.E. Leube, K. Keijser, M. Link and P. Vooijs Expression of Keratins 1,6,15,16, and 20 in Normal Cervical Epithelium, Squamous Metaplasia, Cervical Intraepithelial Neoplasia, and Cervical Carcinoma. *Am. J. Pathol.* 1993, **142**, 403-412.
44. G.J. Smith, W.H. Melhuish. Fluorescence and Phosphorescence of Wool Keratin Excited by UV-A Radiation. *Text. Res. J.* 1985, **55**, 304-307.
45. K. Millington, L. Kirschenbaum. Crosslinking and Visible Fluorescence in Fibrous Proteins, *Textile and Fiber Technology*, <http://www.tft.csiro.au>

46. A.J. Bailey, R.G. Paul, L. Knott. Mechanisms of Maturation and Ageing of Collagen. *Mech. Ageing and Dev.* 1998, **106**, 1-56.
47. D.P. Thornhill. 1975. *Biochem J*, **147**, 215-19
48. P. Odetti, M.A. Pronzato, G. Noberasck, L. Cosso, N. Traverso, D. Cottalasso, U.M. Marinari, Relationships Between Glycation and Oxidation Related Fluorescences in Rat Collagen During Aging, *Laboratory Investigation*, 1994, **70**, 61-67.
49. J.W. Baynes, Role of Oxidative Stress in Development of Complications in Diabetes, *Diabetes*, 1991, **40**, 405-411.
50. R. Drezek, C. Brookner, I. Pavlova, I. Boiko, A. Malpica, R. Lotan, M. Follen, R. Richards-Kortum. Autofluorescence Microscopy of Fresh Cervical Tissue Sections Reveals Alterations in Tissue Biochemistry with Dysplasia. *Photochem. Photobiol.* 2001, **73**, 636-41.
51. I. Pavlova, K. Sokolov, R. Drezek, A. Malpica, M. Follen, R. Richards-Kortum, Microanatomical and biochemical origins of normal and precancerous cervical autofluorescence using laser scanning fluorescence confocal microscopy. *Photochem. Photobiol.* 2003, **77**, 550-555.
52. J.R. Mourant, A.H. Hielscher, A.A. Eick, T.M. Johnson, J.P. Freyer. Evidence of intrinsic differences in the light scattering properties of tumorigenic and nontumorigenic cells. *Cancer*. 1998, **84**, 366-74.
53. R. Drezek, M. Guillaud, T. Collier, I. Boiko, A. Malpica, C. MacAulay, M. Follen, R. Richards-Kortum. Light scattering from cervical cells throughout neoplastic progression: influence of nuclear morphology, DNA content, and chromatin texture. *J. Biomed. Opt.* 2003, **8**, 7-16.
54. D. Arifler, M. Guillard, A. Carraro, A. Malpica, M. Follen, R. Richards-Kortum, Light scattering from normal and dysplastic cervical cells at different epithelial depths: finite-difference time-domain modeling with a perfectly matched layer boundary condition. *J. Biomed. Opt.* 2003, **8**, 484-494.
55. M. Macluskey, L. M. Chandrachud, S. Pazouki, M. Green, D. M. Chisholm, G.R. Ogden, S. L. Schor, A.M. Schor. Apoptosis, proliferation, and angiogenesis in oral tissue. Possible relevance to tumor ptogression. *J. Pathol.* 2000, **191**, 368-375.
56. B. Chen, K. Stamnes, J.J. Stamnes, Validity of the Diffusion Approximation in Bio-optical Imaging. *Appl Opt*, 2001, **40**, 6356-6366.

57. A. Keinle, M.S. Patterson, N. Utke, R. Bays, G. Wagnieres, H. Van Den Bergh, Determination of the Optical Properties of Two-layer Turbid Media. *J Mod Opt*, 1998, **39**, 1567-1582.
58. G. Alexandrakis, T.J. Farrell, M.S. Patterson. Accuracy of the Diffusion Approximation in Determining the Optical Properties of a Two-Layer Turbid Medium. *Appl Opt*, 1998, **37**, 7401-7409.
59. W. M. Star. "Diffusion theory of light transport" in *Optical-Thermal Response of Laser-Irradiated Tissue*, A. J. Welch and M. J. C. van Gemert, eds., Plenum, New York (1995).
60. P. Thuelier, I. Charvet, F. Bevilacqua, M. St. Ghislain, G. Ory, P. Marquet, P. Meda, B. Vermeulen, C. Depeursinge. In vivo endoscopic tissue diagnostics based on spectroscopic absorption, scattering, and phase function properties. *Journal of Biomedical Optics*, 2003, **8**, 495-503.
61. J. Wu, M. S. Feld, R.P. Rava, Analytical model for extracting intrinsic fluorescence in turbid media. *Appl. Opt.*, 1993, **32**, 3585-3595.
62. M.S. Nair, N. Ghosh, N.S. Raju, A. Pradhan, Determination of optical parameters of human tissue from spatially resolved fluorescence: a diffusion theory model. *Appl. Opt.*, 2002, **41**, 4024-4034.
63. D. E. Hyde, T. J. Farrell, M. Patterson, B.C. Wilson. A diffusion theory model of spatially resolved fluorescence from depth-dependent fluorophore concentrations. *Phys. Med. Biol.*, 2001, **46**, 369-383.
64. S.K. Chang, D. Arifler, R. Drezek, M. Follen, R. Richards-Kortum. Analytical Model to Describe Fluorescence Spectra of Normal and Preneoplastic Epithelial Tissue: Comparison with Monte Carlo Simulations and Clinical Measurements. *J Biomed Opt*, 2004, **9**, 511-522.
65. R. Drezek, K. Sokolov, U. Utzinger, I. Boiko, A. Malpica, M. Follen and R. Richards-Kortum. Understanding the contributions of NADH and collagen to cervical tissue fluorescence spectra: Modeling, measurements, and implications. *J. of Biomed. Opt.* 2001, **6**, 385-396.
66. G. Zonios, L.T. Perelman, V. Backman, R. Manoharan, M. Fitzmaurice, J. Van Dam, M.S. Feld. Diffuse Reflectance Spectroscopy of Human Adenomatous Colon Polyps In Vivo. *Appl. Opt.*, 1999, **38**, 6628-6637.
67. S. L. Jacques, L. Wang, "Monte Carlo modeling of light transport in tissues," in *Optical-Thermal Response of Laser-Irradiated Tissue*, A. J. Welch and M. J. C. van Gemert, eds., Plenum, New York (1995).

68. N. Ramanujam, M.F. Mitchell, A. Mahadevan, et al. Spectroscopic diagnosis of cervical intraepithelial neoplasia CIN in vivo using laser-induced fluorescence spectra at multiple excitation wavelengths. *Lasers Surg Med* 1996, **19**, 63-74.
69. T. Collier, D. Arifler, A. Malpica, M. Follen, R. Richards-Kortum. Determination of epithelial tissue scattering coefficient using confocal microscopy. *IEEE J Sel Top Quant Electron* 2003, **9**, 307-13.
70. A.L. Clark, A. Gillenwater, R. Alizadeh-Naderi, A.K. El-Naggar, R. Richards-Kortum. Detection and diagnosis of oral neoplasia with an optical coherence microscope. *J Biomed Opt* 2004, **9**, 1271-80.
71. N.A. Bhowmick, H.L. Moses. Tumor-stroma interactions. *Curr Opin Genet Dev* 2005, **15**, 97-101.
72. P. Zigrino, S. Löffek, C. Mauch. Tumor-stroma interactions: their role in the control of tumor cell invasion. *Biochimie* 2005, **87**, 321-8.
73. W.K. Hong, M.B. Sporn. Recent advances in chemoprevention of cancer. *Science* 1997, **278**, 1073-7.
74. M.D. Mignogna, S. Fedele, L. Lo Russo, E. Bucci. Immune activation and chronic inflammation as the cause of malignancy in oral lichen planus: is there any evidence? *Oral Oncol* 2004, **40**, 120-30.
75. D.E. Ingber. Cancer as a disease of epithelial-mesenchymal interactions and extracellular matrix regulation. *Differentiation* 2002, **70**, 547-60.
76. D. Arifler, I. Pavlova, A. Gillenwater, R. Richards-Kortum. Light Scattering from Collagen Fiber Networks: Micro-Optical Properties of Normal and Neoplastic Stroma. *Biophys J*. 2007, **92**, 3260-74.
77. P.B. Sugerman, N.W. Savage, L.J. Walsh, et al. The pathogenesis of oral lichen planus. *Crit Rev Oral Biol Med* 2002, **13**, 350-65.
78. L. Montebugnoli, A. Farnedi, C. Marchetti, E. Magrini, A. Pession, M.P. Foschini. High proliferative activity and chromosomal instability in oral lichen planus. *Int J Oral Maxillofac Surg* 2006, **35**, 1140-4.
79. A.S. Narayanan, J.A. Clagett, R.C. Page. Effect on Inflammation on the distribution of collagen types I, III, IV, and V and Type I Trimer and Fibronectin in Human Gingivae. *J Dent Res* 1985, **64**, 1111-6.

80. P. Wilder-Smith, K. Osann, N. Hanna, et al. In vivo multiphoton fluorescence imaging: a novel approach to oral malignancy. *Lasers Surg Med* 2004, **35**, 96-103.
81. G. Gannot, I. Gannot, H. Vered, A. Buchner, Y. Keisari. Increase in immune cell infiltration with progression of oral epithelium from hyperkeratosis to dysplasia and carcinoma. *Br J Cancer* 2002, **86**, 1444-8.
82. M. Syafriadi, J. Cheng, K.Y. Jen, H. Ida-Yonemochi, M. Suzuki, T. Saku. Two-phase appearance of oral epithelial dysplasia resulting from focal proliferation of parabasal cells and apoptosis of prickle cells. *J Oral Pathol Med* 2005, **34**, 140-9.
83. I. Georgakoudi, B. C. Jacobson, M. G. Muller, E. E. Sheets, K. Badizadegan, D. L. Carr-Locke, C. P. Crum, C. W. Boone, R. R. Dasari, J. Van Dam, and M. S. Feld. NAD(P)H and collagen as in vivo quantitative fluorescent biomarkers of epithelial precancerous changes. *Cancer Res.* 2002, **62**, 682–687
84. Y. Wu, J.Y. Qu. Combined depth- and time-resolved autofluorescence spectroscopy of epithelial tissue. *Opt Lett* 2006; **31**, 1833-5.
85. Q. Liu, N. Ramanujam. Sequential estimation of optical properties of a two-layered epithelial tissue model from depth-resolved ultraviolet-visible diffuse reflectance spectra. *Appl. Opt.* 2006, **45**, 4776-4790.
86. J. C. Finlay, T. H. Foster. Recovery of hemoglobin oxygen saturation and intrinsic fluorescence with a forward-adjoint model. *Appl. Opt.* 2005, **44**, 1917–1933.
87. S.K. Chang, N. Marin, M. Follen, R. Richards-Kortum. Model-based analysis of clinical fluorescence spectroscopy for in vivo detection of cervical intraepithelial dysplasia. *J. Biomed Opt.* 2006, **11**, 024008.
88. D. Arifler, C. MacAulay, M. Follen, R. Richards-Kortum. Spatially resolved reflectance spectroscopy for diagnosis of cervical precancer: Monte Carlo modeling and comparison to clinical measurements. *J Biomed Optics*, 2006, **11**, 064027.
89. J.Y. Qu, C.E. MacAulay, S. Lam, B. Palcic. Laser-induced fluorescence spectroscopy at endoscopy: tissue optics, Monte Carlo modeling, and in vivo measurements. *Opt. Eng.* 1995, **34**, 3334.
90. D. Hidovic-Rowe, E. Claridge. Modeling and validation of spectral reflectance for the colon. *Phys. Med. Biol.* 2005, **50**, 1071-1093.
91. I. Pavlova, M. Williams, A. El-Naggar, R. Richards-Kortum, A. Gillenwater. Understanding the biological basis of autofluorescence imaging for oral cancer

- detection: High resolution fluorescence microscopy in viable tissue. *Clinical Cancer Research* (in press)
92. T. Collier, M. Follen, A. Malpica, R. Richards-Kortum, Sources of scattering in cervical tissue: determination of the scattering coefficient by confocal microscopy. *Appl. Opt.* 2005, **43**, 2072-2081
 93. D. Arifler, R. A. Schwarz, S. K. Chang, and R. Richards-Kortum, Reflectance spectroscopy for diagnosis of epithelial precancer: model-based analysis of fiber-optic probe designs to resolve spectral information from epithelium and stroma. *Appl. Opt.* 2005, **44**, 4291-4305.
 94. J. Qu, C. MacAulay, S. Lam, B. Palcic, Optical properties of normal and carcinomatous bronchial tissue. *Appl. Opt.* 1994, **33**, 7397–7405.
 95. J. R. Mourant, J. P. Freyer, A. H. Hielscher, A. A. Eick, D. Shen, and T. M. Johnson. Mechanisms of light scattering from biological cells relevant to noninvasive optical-tissue diagnostics. *Appl. Opt.* 1998, **37**, 3586–3593.
 96. S. L. Jacques 1998 Skin Optics (Portland, OR: Oregon Medical Laser Centre) <http://omlc.org.edu/news/jan98/skinoptics.html>
 97. I. S. Saidi. Transcutaneous optical measurement of hyperbilirubinemia in neonates. PhD Dissertation, Rice University, Houston, TX
 98. A. J. Welch, C. Gardner, R. Richards-Kortum, E. Chan, G. Criswell, J. Pfefer, and S. Warren. Propagation of fluorescent light. *Lasers Surg. Med.* 1997, **21**, 166–178.
 99. W. H. Crawford, Chapter 13: Mucosa: Cancer and premalignant diseases. 2002.
 100. F. Feldchtein, V. Gelikonov, R. Iksanov, G. Gelikonov, R. Kuranov, A. Sergeev, N. Gladkova, M. Ourutina, D. Reitze, J. Warren. In vivo OCT imaging of hard and soft tissue of the oral cavity. *Opt. Express*, 1998, **3**, 239-250.

Vita

Ina Pavlova was born in Sofia, Bulgaria on December 12, 1973, the daughter of Pavel Pavlov and Stefka Georgieva. After graduating from high school, she came to the United States and entered The University of Texas at Austin. She graduated in May 1999 with a Bachelor of Art degree in chemistry. In January 2002, she entered the Graduate School of the University of Texas Austin to pursue a Doctorate of Biomedical Engineering. She obtained a Master of Science in Biomedical Engineering in 2003 under the supervision of Rebecca Richards-Kortum. After receiving her M.A., she continued work on her Doctorate under the supervision of Rebecca Richards-Kortum.

Permanent address: 27 A Buntovnik St., Sofia Bulgaria

This dissertation was typed by the author.